DEVELOPMENT OF A MECHANISTIC MODEL FOR CAPILLARY PRESSURES AND RELATIVE PERMEABILITIES TO ESTIMATE OIL AND GAS RECOVERIES FOR UNCONVENTIONAL RESERVOIRS UNDER DEPLETION AND GAS INJECTION

A Thesis

by

BARTOSZ TADEUSZ CZERNIA

Submitted to the Office of Graduate and Professional Studies of
Texas A&M University
in partial fulfillment of the requirements for the degree of

MASTER OF SCIENCE

Chair of Committee,	Maria A. Barrufet
Committee Members,	Thomas A. Blasingame
	William John Lee
Head of Department,	Jeffrey Spath

August 2018

Major Subject: Petroleum Engineering

ABSTRACT

A mechanistic model was created to calculate recovery factors and capillary pressure curves for unconventional reservoirs. A key aspect of the model is that it accounts for the effect of fluid confinement that occurs inside small diameter pores in unconventional reservoirs. Confinement effects are incorporated through the calculation of capillarity via the Young-Laplace equation. The model is intended to provide an estimate of recovery factors that is faster and simpler to use than a full reservoir simulation. The model simulates initial depletion of the reservoir and then simulates one or more gas injection steps as an enhanced oil recovery technique. The results from the model are unique to the specific reservoir fluid composition, pore size distribution, degree of depletion, injection gas composition, injection gas amount and number of injection steps specified for the run. The results from the model are compared against small-scale reservoir simulation runs under equivalent conditions. The simulator used for the comparison is a Matlab based, compositional research simulator that is capable of modeling pore confinement effects.

For an idealized reservoir model, the mechanistic model and the reservoir simulation results match for both the initial depletion and gas injection portions of the run. For larger reservoir models containing a greater number of cells, the mechanistic model matches the simulation results closely for the initial depletion. However, the two methods do not match for the gas injection portion of the run. This mismatch occurs

because the mechanistic model is not capable of modeling the complex mixing of the injection gas with the reservoir fluids as the gas moves through the reservoir volume.

To isolate the impact of confinement on production, each reservoir simulation is run once with confinement effects considered and again using bulk fluid behavior (no confinement effects). All other run parameters are held constant between the runs. For a black oil reservoir fluid, the confinement effects increase the ratio of oil to gas production. For a volatile oil, confinement has a minimal impact on the ratio of oil to gas production.

ACKNOWLEDGEMENTS

I would like to thank my advisor Dr. Maria Barrufet for her guidance, expertise, patience and assistance throughout the course of my graduate studies. She was always available to provide encouragement and feedback throughout the course of my research project.

I would like to thank my committee members, Dr. Blasingame and Dr. Lee for their excellent classroom instruction. Their technical knowledge combined with their ability to explain often confusing topics in a clear and concise manner made both courses valuable and memorable.

I would like to thank my parents and my younger brother for supporting me throughout the course of my degree.

I would also like to thank my friends and colleagues and the department faculty and staff for helping me throughout my time at Texas A&M University.

Portions of this research were conducted with the advanced computing resources provided by Texas A&M High Performance Research Computing. I would like to thank the staff for their consultation and assistance.

CONTRIBUTORS AND FUNDING SOURCES

Contributors

This work was supervised by a thesis committee consisting of Dr. Maria A. Barrufet of the Department of Petroleum Engineering and the Department of Chemical Engineering, Dr. Thomas A. Blasingame of the Department of Petroleum Engineering and the Department of Geology of Geophysics and Dr. John Lee of the Department of Petroleum Engineering.

Funding Sources

Graduate study was generously supported through a research assistantship from the Department of Petroleum Engineering and the Crisman Institute for Petroleum Engineering.

NOMENCLATURE

Symbol	Definition	Units
A^ℓ	Polynomial EOS constant for phase ℓ	Unitless
a_i	Attraction parameter for component i	$(psia-ft^6)/(lbmol^2)$
a^ℓ	EOS attraction parameter for phase ℓ	$(psia-ft^6)/(lbmol^2)$
B^ℓ	Polynomial EOS constant for phase ℓ	Unitless
b_i	Covolume parameter for component i	$ft^3/lbmol$
b^ℓ	Covolume parameter for phase ℓ	$ft^3/lbmol$
c^ℓ	Volume shift parameter for phase ℓ	$ft^3/lbmol$
f_i^ℓ	Fugacity of component i in phase ℓ	psia
f_v	Molar vapor fraction	Unitless
f(x)	Lognormal probability density function	Unitless
F(x)	Lognormal cumulative probability density function	Unitless
K_i	Vapor liquid equilibrium ratio	Unitless
k_{ij}	Binary interaction parameter, components i and j	Unitless
k	Permeability	mD
$k_{r\ell}$	Relative permeability of phase ℓ	Unitless
P_i	Parachor of component i	$(dyne^{1/4}-cm^{11/4})/mol$
p^ℓ	Pressure of phase ℓ	psia
$p_{c,i}$	Critical pressure of component i	Psia

Symbol	**Definition**	**Units**
M_i	Molar weight of component i	lb/lbmol
Nc	Number of components	Unitless
N_D	Number of depletion steps	Unitless
N_I	Number of injection steps	Unitless
R (10.731)	Universal gas constant	(ft^3-psi)/(lbmol-°R)
R_1	Spherical radius 1	nm
r	Pore radius	nm
s_i	Shift parameter of component i	Unitless
T	Temperature	°R
$T_{c,i}$	Critical temperature of component i	°R
$T_{r,i}$	Reduced temperature	Unitless
V_m^{ℓ}	Molar volume for phase ℓ	ft^3/lbmol
$V_m^{\ell\text{-EOS}}$	Molar volume for phase ℓ (from EOS with no volume shift applied)	ft^3/lbmol
x_i^{ℓ}	Molar fraction of component i in phase ℓ	Unitless
y_i^V	Molar vapor fraction of component i	Unitless
Z^{ℓ}	Compressibility factor of phase ℓ	Unitless
z_i	Molar fraction of component i	Unitless

Greek Symbol	Definition	Units
α_i	Temperature dependent scaling factor for a of component i	Unitless
ω_i	Accentric factor of component i	Unitless
σ	Interfacial tension	dyne/cm
σ_{ln}	Lognormal standard deviation	nm
Θ	Contact angle	Degree
φ_i^ℓ	Fugacity coefficient of component i in phase ℓ	Unitless
ρ^ℓ	Density of phase ℓ	lb/ ft^3
λ_ℓ	Mobility of phase ℓ	mD/cP
μ_ℓ	Viscosity phase ℓ	cP
μ_{ln}	Lognormal mean	nm

Superscripts	Definition
ℓ	Phase
c	Critical
v	Vapor
l	Liquid
k	Current iteration step
k+1	Next iteration step

Subscripts	**Definition**
i	Component
k	Component
cap	Capillary
init	Initial
fin	Final

TABLE OF CONTENTS

LIST OF FIGURES

LIST OF TABLES

1. INTRODUCTION AND LITERATURE REVIEW

1.1 Equations of State and Vapor Liquid Equilibrium

The first example of an Equation Of State (EOS) was the ideal gas law (Clapeyron 1834) which was accurate for gases at low pressures. However, the equation was insufficient for pressures above a few atmospheres due to what is known as non-ideal behavior. Van der Waals (1873) improved on this equation with the addition of terms that account for the attraction and repulsion of molecules. This equation also allowed modeling of both vapor and liquid phases. Redlich and Kwong (1949) proposed an EOS based on the van der Waals equation that allowed calculation of Vapor Liquid Equilibrium (VLE) for multicomponent mixtures. The equation improved accuracy through the use of a more accurate intermolecular attraction term. A number of modifications to the Redlich-Kwong (RK) equation were subsequently proposed. One of the most important was a modification proposed by Soave (1972) which introduced temperature dependence into the molecular attraction term and also accounted for the eccentricity (non-spherical shape) of molecules. This became known as the Soave-Redlich-Kwong (SRK) equation.

A new EOS was proposed by Peng and Robinson (1976) which produced more accurate liquid density values compared to the SRK equation. However, like the SRK equation before it, the Peng-Robinson (PR) had problems accurately modeling polar compounds. Peneloux (1982) introduced an equation that allows for correction of phase density without affecting the calculated phase equilibrium. The volume correction was originally formulated for the SRK equation but can also be applied to volumes calculated using the PR equation. Throughout the years, new equations of state have been developed but the Peng-Robinson remains one of the most widely used in the oil and gas industry and is used in this research.

1.2 Effects of Capillary Pressure

Some of the earliest observations of the effects of capillary pressure were documented by Hauksbee (1711) who measured the rise of water between two parallel glass plates as a function of distance separating the plates. This behavior occurs due to the attraction of the water molecules to the glass surface which causes the water to rise up the glass surface. The attraction of the water molecules is counteracted by the gravitational force on the water. When the forces are in equilibrium the height of the water level between the plates multiplied by the density of the water is equal to the capillary pressure. The magnitude of capillary pressure varies with the separation of the plates.

Young (1805) reviewed a number of experiments on capillary pressure and offered a more thorough qualitative description of capillary pressure. Laplace (1805) developed a mathematical description of capillary pressure which was expanded on by Gauss (1830) into what is known today as the Young-Laplace equation.

Leverett (1941) discussed the effect of capillary pressure on static equilibrium in porous media as well as the impact on dynamic flow processes. In porous media, the capillary pressure is a function of pore throat diameter, therefore, when the media has a distribution of pore sizes, which is the case when dealing with any natural material, each pore will experience a different capillary pressure. The most common method of measuring capillary pressure of rock samples in the oil and gas industry is the mercury injection experiment that was introduced by Purcell (1949). This method can be utilized to produce a single capillary pressure curve for the reservoir rock that accounts for all the different sized pores. In commercial reservoir simulators, capillary pressure data is input by the user and is completely separate from the vapor liquid equilibrium calculations. This is in contrast to the vapor liquid equilibrium calculations utilized for the work in this thesis. The inclusion of capillary pressure is explained in detail in Section 2. In this work, the focus is on the oil-gas capillary pressure. This is important because there can be a significant amount of mass transfer between these phases. Oil-water and gas-water capillary pressures are not considered in this work because hydrocarbon solubility water is low.

1.3 Influences of Confinement on Petrophysical Properties

Since the late 2000's, the United States has experienced a surge in production of oil and gas from shales and other tight reservoir rocks. These reservoirs fall under the umbrella term "unconventional resources". It is projected that these unconventional resources will constitute an increasingly larger portion of us oil production as demonstrated in Figure 1.1.

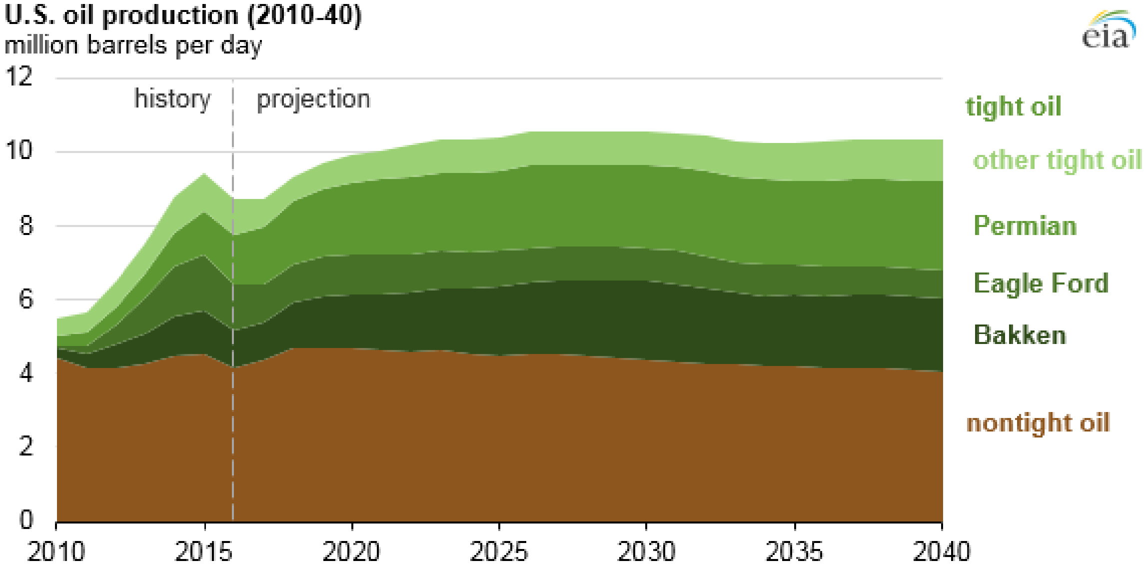

Figure 1.1: Historical and projected US oil production by source (reprinted from Energy Information Administration 2017).

One of the defining characteristics of these reservoirs is that they contain smaller pore sizes than are typically found in conventional reservoir rocks (Loucks et. al. 2009). While a conventional sandstone reservoir may have typical pore sizes in the micrometer range, an unconventional shale may have a significant fraction of its total pore volume represented by pore sizes in the nanometer range (Nelson 2009) as seen in Figure 1.2.

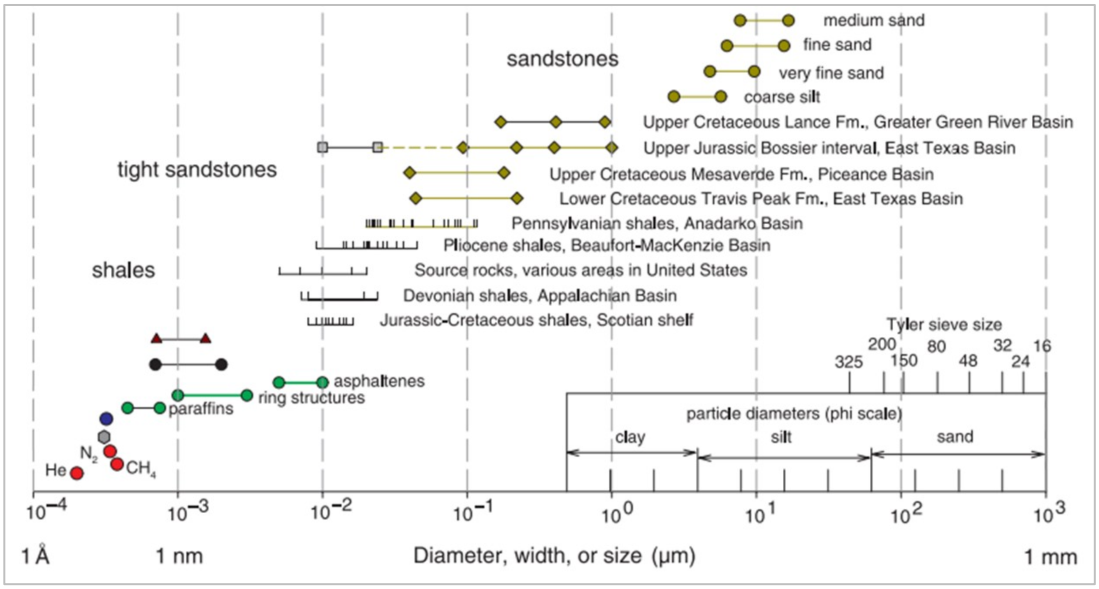

Figure 1.2: Comparison of pore diameter ranges for different reservoirs (reprinted from Nelson 2009).

As the size of the pore decreases, the ratio of internal pore surface area to pore volume increases. For example, for a spherical pore the ratio of pore surface area to volume is equal to three divided by the pore radius. Because of this ratio, the effect of hydrocarbon molecules interacting with the pore walls becomes more significant as the pore size decreases. This increasing amount of interaction can cause the fluid to behave differently from how the same fluid behaves under bulk conditions at the same temperature and pressure. In large pores, there is still interaction between hydrocarbon molecules and the pore wall, however, the amount of interaction is insignificant and does not affect phase behavior.

This difference at small pore sizes is called “fluid confinement”. As a result, the equations of state used to describe bulk fluid behavior may not be appropriate for describing the confined fluid behavior. Industry standard laboratory PVT (Pressure-Volume-Temperature) tests used to characterize reservoir fluids can measure bulk fluid properties but cannot replicate the effects of confinement (Honarpour et al. 2012).

The change in behavior of reservoir fluids resulting from confinement in nanometer scale pores has only been experimentally investigated to a limited extent. This is largely due to the technical difficulty of measuring the properties of fluids while confined inside core samples. Most experimental work instead relies on nanometer sized channels etched into manmade materials such as glass to simulate small pores. Luo et al. (2016) performed experimental work in which the effect of confinement on the bubble point of octane and decane was studied. The experiments were all conducted at atmospheric pressure. The fluids were confined in a powdered glass material that contained pores of known sizes and shapes. At the smaller pore size studied, 4.3 nm, the bubble point of the hydrocarbon decreased below that of the bulk fluid. The larger pore size, 38.1 nm, resulted in a negligible impact on the bubble point compared to the bulk hydrocarbon.

Most of the research on confinement of hydrocarbons has utilized molecular simulation studies. Zhang et al. (2016) performed molecular simulations on mixtures of methane and ethane confined within cylindrical carbon nanotubes and found that the interaction between hydrocarbon molecules and the pore wall creates a heterogeneous distribution of hydrocarbon components. The net effect of this distribution is a decrease in the bubble point of the mixture. The confinement effect was first noticed at a pore radius of

50 nm. At the smallest pore radius evaluated, 5 nm, the bubble point pressure decreased by approximately 500 psi for a 50-50% molar mixture at a temperature of approximately 350°F.

Didar and Akkutlu (2015) performed molecular simulations on methane, ethane, n-butane, n-octane, and binary mixtures of these hydrocarbons. In this study, the fluids were confined in a slit shaped pore made of graphite (carbon) walls. The results showed that at two phase conditions, confinement effects causing an increase in gas phase density and a decrease in liquid phase density compared to bulk condition results. These effects became more pronounced as the size of the slit decreased. This was true for both single components and mixtures. It was also concluded that these effects are more pronounced for lighter hydrocarbons.

A number of additional molecular simulation studies have been performed using different combinations of pore size, pore shape and hydrocarbons. The consensus among these studies is that at pore sizes less than approximately 50 nm, confinement effects result in a suppression of the bubble point pressures for hydrocarbons with the degree of suppression corresponding to pore size.

1.4 Incorporation of Confinement Effects into an Equation of State

The use of molecular simulation to model hydrocarbon behavior under confinement has the advantage of being physically rigorous but is too computationally intensive to be used outside of a research application. Additionally, most studies model behavior in an individual pore containing simple one or two component mixtures. Therefore, there is great interest in finding a way to accurately capture the effect of confinement on fluid behavior in a less computationally intensive manner. A number of approaches have been examined to incorporate the effects of confinement into existing equations of state.

One of the simplest approaches to capturing confinement effects is to alter the critical properties of the individual components in the mixture. These altered critical properties can then be used directly in the phase simulator or reservoir simulator of choice. Using data obtained from a molecular simulation study, Jin et al. (2013) developed a set of correlations that can be used to calculate shifts in critical temperature and pressure for hydrocarbon components based on bulk critical properties, pore size, and the Lennard-Jones parameter for the molecule. Using these correlations, Sanaei et al. (2014) showed the effect of confinement on a number of different fluid types, including condensates. Additionally, the critical property shifts were incorporated into a reservoir simulator in order to examine the effects of confinement on production rates of oil and gas. The advantage of using the critical property shifts is the simplicity of the approach. However, this approach is not thermodynamically consistent and does not account for changes to fluid compositions that occur over the course of a reservoir simulation.

A more physically rigorous and thermodynamically consistent approach to account for confinement effects is the inclusion of capillary pressure in the calculation of Vapor

Liquid Equilibrium (VLE) as described by Stimpson and Barrufet (2016). When calculating VLE using a cubic equation of state, most commercial phase and reservoir simulators make the assumption that the vapor and liquid phase pressures are equal. For conventional reservoirs containing mostly micron scale pores, this assumption is valid. However, as pore size decreases, the magnitude of capillary pressure can become large enough that the equal pressure assumption is no longer valid. To account for the effect of capillary pressure, the liquid and vapor phase pressures are allowed to vary from one another. The difference in pressures is equal to the capillary pressure which can be calculated from the Young-Laplace equation.

The approach of including capillary pressure has been around for a number of years and many research groups have used some derivation of the capillary pressure approach to quantify confinement effects in unconventional reservoirs. The capillary pressure approach is an attractive approach for including confinement effects because although it is not as physically rigorous as molecular simulation it is orders of magnitude less computationally intensive. Incorporation of capillary pressure as described only requires a modest increase in computational resources over the calculation of bulk fluid behavior using a cubic EOS. Firincioglu et al. (2012) investigated a modeling approach that included capillary pressure effects along with several other effects including interaction of fluid molecules with pore walls due to Van der Waals forces. In the paper, it was concluded that the capillary pressure effects were the dominant force and it was acceptable to ignore the other forces considered.

There are a number of ways to include capillary pressure into the calculation of VLE. A simple method is to have a table lookup that determines capillary pressure as a function of cell oil or gas saturation. This approach is easy to implement but does not account for specific compositions within each cell. A more thermodynamically consistent approach is to calculate the capillary pressure in each cell based on the specific conditions and compositions in that cell. This can be done either explicitly (Haider 2015) where the capillary pressure is calculated once per time step for each cell or implicitly which is the method used in this work. In this work, the capillary pressure is integral to the VLE and is updated with each iteration of the flash calculation.

1.5 Enhanced Oil Recovery

Enhanced Oil Recovery (EOR) is a broad term that refers to any number of methods that are applied to an existing reservoir following primary depletion in an attempt to increase the ultimate recovery from the reservoir. These methods include water flooding, gas reinjection, chemical flooding, miscible flooding, and thermal recovery. These methods have been applied commercially to conventional reservoirs for a number of years (Mosbacher et al. 1984).

Enhanced oil recovery methods are not currently commercially employed in unconventional reservoirs. However, due to the relatively low recovery resulting from primary depletion and the sharp decline in production rates there is great interest in developing EOR methods and techniques for shale and tight oil reservoirs. Some companies have begun testing pilot programs to evaluate the feasibility of EOR in unconventional reservoirs (Addison 2016).

Fragoso et al. (2015) examined the feasibility of using gas reinjection in the Eagle Ford shale to increase liquids recovery. They concluded that a huff and puff approach could increase the recovery by approximately 20% depending on the injected gas. They concluded that continuous gas injection through a separate injection well could potentially increase the recovery by a larger amount, however, this would be highly dependent on the combination of reservoir permeability, availability of injection wells and the presence of natural fractures.

Tovar et al. (2014) performed experimental studies on shale cores to investigate CO_2 injection as a possible enhanced recovery method for shale reservoirs. They found that similar to what is observed in conventional reservoirs, CO_2 causes oil to swell, decreases viscosity and therefore increases oil mobility. They also propose that the presence of CO_2 results in a reduction in capillary forces within the confined pores which would also aid in recovery.

2. METHODOLOGY

2.1 Phase Simulation

This work relies on numerical phase simulation to determine the hydrocarbon phase properties at the conditions being analyzed. The following summarizes the equations and methodology employed in this work to model phase behavior.

2.1.1 Peng Robinson Equation of State

The phase behavior in this work is modeled using equations based on the Peng-Robinson (PR) Equation of State (EOS) shown in Eq. 2.1 solving for the pressure of phase ℓ, which can be either liquid or vapor.

$$p^{\ell} = \frac{RT}{V_m^{\ell} - b^{\ell}} - \frac{a^{\ell}}{V_m^{\ell}\left(V_m^{\ell} + b^{\ell}\right) + b^{\ell}\left(V_m^{\ell} - b^{\ell}\right)} \tag{2.1}$$

When dealing with a mixture of components the attraction parameter (*a*) and van der Waals covolume (*b*) for the mixture are calculated using the mixing rules in Eq. 2.2 and 2.3 respectively.

$$a^{\ell} = \sum_{i=1}^{Nc}\sum_{j=1}^{Nc} x_i^{\ell} x_j^{\ell}(1 - k_{ij})\sqrt{a_i a_j} \tag{2.2}$$

$$b^{\ell} = \sum_{i=1}^{Nc} x_i^{\ell} b_i \tag{2.3}$$

The attraction parameter and covolume for each individual component are calculated using Eq. 2.4 and 2.5 respectively.

$$a_i = 0.45724\frac{R^2T_{c,i}^2}{p_{c,i}}\alpha_i \tag{2.4}$$

$$b_i = 0.0778\frac{RT_{c,i}}{p_{c,i}} \tag{2.5}$$

The value of α for component i is calculated using either Eq. 2.6 or 2.7 depending on accentric factor which is based on molecule size. Eq. 2.6 is used for components with an accentric factor less than or equal to 0.491. For longer molecules with an accentric factor exceeding 0.491 Eq. 2.7 is used.

$$\alpha_i = \left(1 + (0.037464 + 1.54226\omega_i - 0.26992\omega_i^2)\left(1 - \sqrt{\frac{T}{T_{c,i}}}\right)\right)^2 ; if\ \omega_i \leq 0.491 \tag{2.6}$$

$$\alpha_i = \left(1 + \left(0.037464 + 1.485\omega_i - 0.1644\omega_i^2 + 0.01667\omega_i^3\right)\left(1 - \sqrt{\frac{T}{T_{c,i}}}\right)\right)^2 ; if\ \omega_i > 0.491 \tag{2.7}$$

The PR EOS is often combined with the real gas law (Eq. 2.8) and reorganized as shown in Eq. 2.9 to yield a cubic equation that can be solved for the compressibility factor *Z*.

$$Z^\ell = \frac{p^\ell V_m^\ell}{RT} \tag{2.8}$$

$$\left(Z^\ell\right)^3 - \left(1 - B^\ell\right)\left(Z^\ell\right)^2 + \left(A^\ell - 3\left(B^\ell\right)^2 - 2B^\ell\right)Z^\ell - \left(A^\ell B^\ell - \left(B^\ell\right)^2 - \left(B^\ell\right)^3\right) = 0 \tag{2.9}$$

Where:

$$A^\ell = \frac{a^\ell p^\ell}{(RT)^2} \tag{2.10}$$

$$B^{\ell} = \frac{b^{\ell} p^{\ell}}{RT} \tag{2.11}$$

If multiple real roots exist for the cubic equation, the largest root corresponds to the gas phase compressibility factor and the lowest to the liquid phase compressibility factor. If only one real root exists this indicates a single phase mixture.

2.1.2 Calculation of Fugacity

When multiple phases exist the distribution of moles between the two phases is determined by calculating the Vapor-Liquid Equilibrium (VLE) for the system. Equilibrium is defined as the condition where the fugacity of each component in the vapor and liquid phases is equal. The fugacity coefficient of component i in phase ℓ is calculated from Eq. 2.12.

$$\ln \phi_i^{\ell} = \frac{A^{\ell}}{2\sqrt{2}B^{\ell}} \left[\frac{2\sum_{j=1}^{Nc} x_j \sqrt{a_i a_j}(1-k_{ij})}{a^{\ell}} - \frac{b_i}{b^{\ell}} \right] \ln\left(\frac{Z^{\ell} + 2.414B^{\ell}}{Z^{\ell} - 0.414B^{\ell}} \right) + \frac{b_i}{b^{\ell}}\left(Z^{\ell} - 1\right) - \ln(Z^{\ell} - B^{\ell}) \tag{2.12}$$

The fugacity of component i in phase ℓ (f_i^{ℓ}) is related to the fugacity coefficient (φ_i^{ℓ}) by Eq. 2.13.

$$f_i^{\ell} = \phi_i^{\ell} p^{\ell} x_i^{\ell} \tag{2.13}$$

Vapor liquid equilibrium exists when the fugacity of every component (i) is equal in the vapor and liquid phases (Eq. 2.14).

$$\phi_i^{v} p^{v} y_i^{v} = \phi_i^{l} p^{l} x_i^{l}; \quad for\ i = 1\ to\ Nc \tag{2.14}$$

This equation can be reorganized to calculate the vapor liquid equilibrium constant of component i in Eq. 2.15.

$$K_i = \frac{y_i}{x_i} = \frac{\phi_i^l}{\phi_i^v}\frac{p^l}{p^v}; \quad for\ i = 1\ to\ Nc \tag{2.15}$$

For bulk fluids where capillary pressure is negligible, the vapor pressure (p^v) is equal to the liquid pressure (p^l) and therefore the pressures cancel out. When considering the effect of capillarity in which the vapor and liquid pressures are different, the pressure values are retained in the VLE calculation and the vapor pressure is equal to the sum of liquid and capillary pressures.

In addition to satisfying the iso-fugacity constraint, VLE must also satisfy a material balance. The sum of component *i* in the liquid and vapor phases must equal the total number of molecules of component *i* in the mixture as shown in Eq. 2.16.

$$z_i = f_v(x_i) + (1 - f_v)y_i \tag{2.16}$$

This equation can be reorganized to solve for liquid (Eq. 2.17) or vapor molar compositions (Eq. 2.18) as a function of vapor molar fraction and equilibrium constant.

$$x_i = \frac{z_i}{1 - f_v + f_v K_i} \tag{2.17}$$

$$y_i = \frac{z_i K_i}{1 - f_v + f_v K_i} \tag{2.18}$$

Summing for all components in the mixture yields Eq. 2.19 from Rachford and Rice (1952).

$$\sum_{i=1}^{Nc}(x_i - y_i) = \sum_{i=1}^{Nc}\frac{z_i(K_i - 1)}{1 - f_v + f_v K_i} = 0 \tag{2.19}$$

2.1.3 Calculation of Capillary Pressure

Capillary pressure is defined as the difference between the pressures of the non-wetting and wetting phases. It is noted that in this work it is assumed that the reservoir is oil wet. Therefore, the liquid hydrocarbon phase will be wetting and the vapor phase will be non-wetting resulting in Eq. 2.20.

$$p_{cap} = p^v - p^l \tag{2.20}$$

This pressure difference arises when one phase has a stronger affinity for the container surface than the other phase. This affinity is quantified through the use of a wetting angle (Θ) also often referred to as the contact angle. The capillary pressure is calculated using the Young-Laplace equation shown in Eq. 2.21. This form of the equation applies to a fluid confined between two spherical surfaces of radius R_1 and R_2 measured as shown in Figure 2.1.

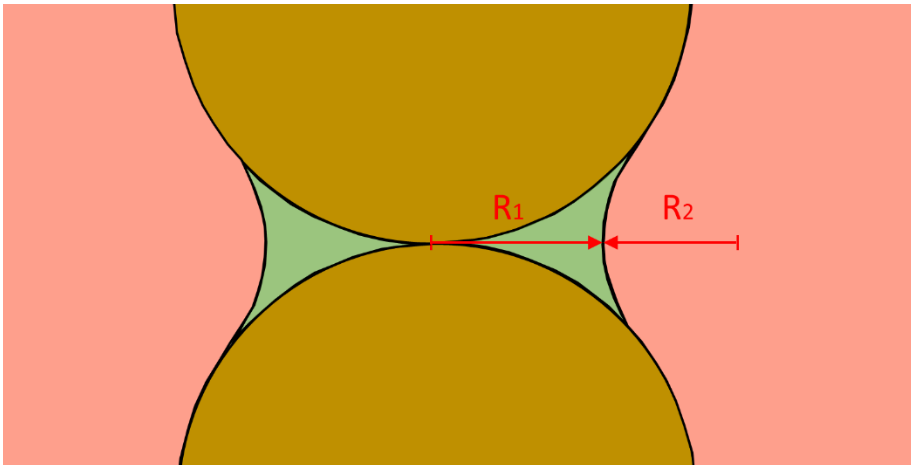

Figure 2.1: Measurement of radii of curvature.

The form of the equation for fluids contained within a cylindrical pore of radius r is shown in Eq. 2.22.

$$p_{cap} = \sigma\left(\frac{1}{R_1} - \frac{1}{R_2}\right) \tag{2.21}$$

$$p_{cap} = \frac{2\sigma\cos(\theta)}{r} \tag{2.22}$$

The capillary pressure calculation is based on the Interfacial Tension (IFT) σ of the vapor/liquid phase interface.

2.1.4 Calculation of Interfacial Tension

The interfacial tension between the vapor and liquid phases is a function of phase density and a component specific value known as a parachor. This relationship was first identified by Sugden (1930) for individual components. The additive nature of parachors for individual chemical groups in organic compounds was discussed by Quayle (1953). Weinaug and Katz (1943) devised an equation for calculating interfacial tension for multicomponent mixtures based on this additive nature shown in Eq. 2.23.

$$\sigma = \left(\sum_{i=1}^{Nc} P_i \left(\frac{x_i \rho^l}{V_m^l} - \frac{y_i \rho^v}{V_m^v}\right)\right)^4 \tag{2.23}$$

2.1.5 Incorporation of Volume Shifts

The PR EOS has well documented limitations when calculating molar volumes. As a result, a number of methods have been proposed to increase the accuracy of the molar volume results. In this work, the method proposed by Peneloux (1982) is utilized as shown in Eq. 2.24 for phase ℓ. This method uses dimensionless shift parameters (s_i), which are unique to each component, and the covolume parameter (b_i) which is calculated as part of the EOS solution. This method does not impact the vapor-liquid equilibrium calculation. Rather, the volume shifts are applied after the equilibrium calculation has converged to a solution.

$$V_m^\ell = V_m^{\ell-EOS} - c^\ell = V_m^{\ell-EOS} - \sum_{i=1}^{Nc} (x_i^\ell s_i b_i) \tag{2.24}$$

2.1.6 Methodology for Determination of Vapor Liquid Equilibrium

As stated above, VLE is defined as the condition where the fugacity of each component in each phase is equal. The phase distribution that satisfies this condition cannot be solved for directly and instead relies on an iterative process. The solution for the VLE of a known composition at a specific temperature and pressure is commonly known as a "flash calculation." An industry standard successive substitution iterative process is used to solve the flash calculation as described in Michelsen (1982). A concise summary of this method is provided by Firoozabadi (1999) and it is shown schematically in Figure 2.2 as follows:

1) The initial equilibrium constants for each component are calculated using the correlation in Eq. 2.25 from Wilson (1969).

$$K_i = \frac{p_{c,i}}{p} e^{\left[5.37(1+\omega_i)\left(1-\frac{1}{T_{r,i}}\right)\right]} \tag{2.25}$$

   This initial step is only performed once per flash calculation. Subsequent steps are inside the iteration loop and may therefore be performed multiple times before convergence is achieved.

2) Calculate the vapor fraction (f_v) using the Rachford-Rice equation. If only a single phase exists, the molar composition of that phase will be equal to the total molar composition.
3) If multiple phases exist ($0<f_v<1$), determine the compositions of each phase from the vapor fraction and the equilibrium constants using Eq. 2.17 and 2.18.
4) Using the vapor and liquid compositions, solve for the compressibility factors for each phase using Eq. 2.9.
5) Calculate fugacity coefficients for each component using Eq. 2.12 and the fugacity of each component using Eq. 2.13.
6) Calculate new equilibrium constants for each component based on the ratio of fugacity coefficients and pressures for each phase. Note that if confinement effects are not being considered (i.e. bulk fluid conditions) the liquid and vapor pressure will be equal and will therefore cancel out.

7) Compare the values of the equilibrium constant from step 6 with those from the previous iteration. If the difference is less than the specified convergence criteria, the phases are in equilibrium and the iterative loop ends. If convergence has not been achieved the new equilibrium constants are used and steps 2-7 are repeated.
8) When confinement effects are included, (i.e. capillary pressure is considered), an additional iterative loop is required to determine the capillary pressure. Steps 1-7 above are repeated, once equilibrium conditions are achieved, capillary pressure is calculated using Eq. 2.22 and 2.23.

This new capillary pressure is compared to the capillary pressure from the previous iteration step (a capillary pressure of zero is always assumed for the first iteration). If the difference in the capillary pressures is less than a specified convergence value, the capillary pressure has converged. If the difference in capillary pressure exceeds the convergence criteria, the new and old values are averaged and the entire process (steps 1-8) is repeated. Step 8, which only applies when confinement effects are being considered, is shown inside the dashed box in Figure 2.2.

When both loops of the calculation have converged to within their respective criteria the flash calculation is complete. At this point, the equilibrium compositions of the phase(s) are known along with the molar volume(s) and vapor fraction.

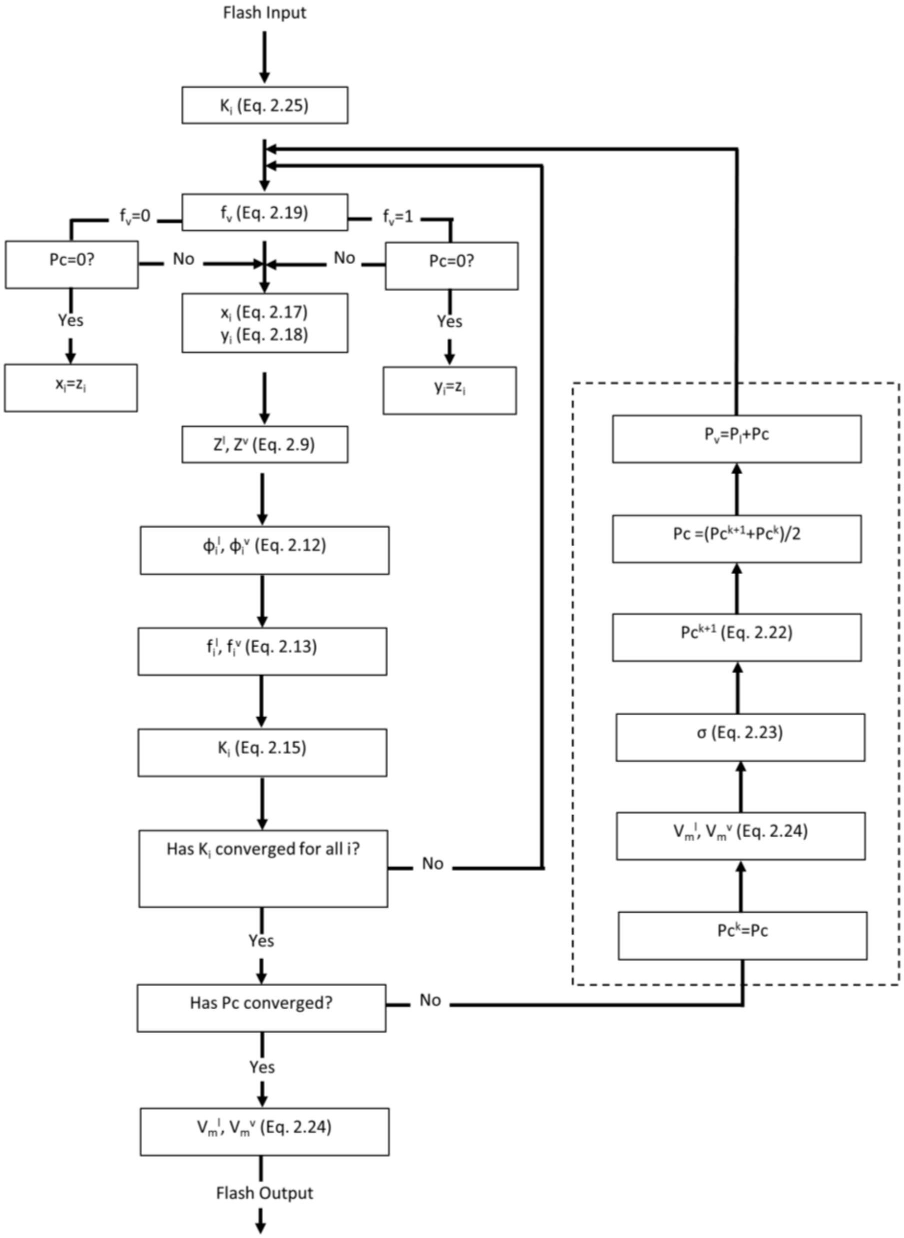

Figure 2.2: Workflow for "flash" calculation. The portion of the workflow inside the dashed box only applies when capillary pressure is included to account for confinement effects.

2.2 Impact of Confinement on Phase Behavior

As described in Section 1, confinement of hydrocarbons within nanoscale pores can cause VLE to deviate from the results for the same fluid under bulk conditions. This behavior is important because it can hinder the ability to accurately model fluid flow which in turn affects any production predictions based on this behavior.

2.2.1 General Theory

Confinement effects are not related to any changes in the fluid itself but rather occur due to the interaction of the fluid with the pore walls. The interaction of the fluid molecules with pore walls becomes more significant as the pore size decreases. At larger pores sizes, the interaction is negligible and the interface between the oil and gas phases is flat (Figure 2.3.A). The interface between the phases is flat and the oil and gas phase pressures are equal. At pore diameters under approximately 100 nm the interaction of the liquid phase with the pore wall causes a curvature of the interface (Figure 2.3.B). This causes a difference in the oil and gas phase pressure equal to the capillary pressure (Eq. 2.22).

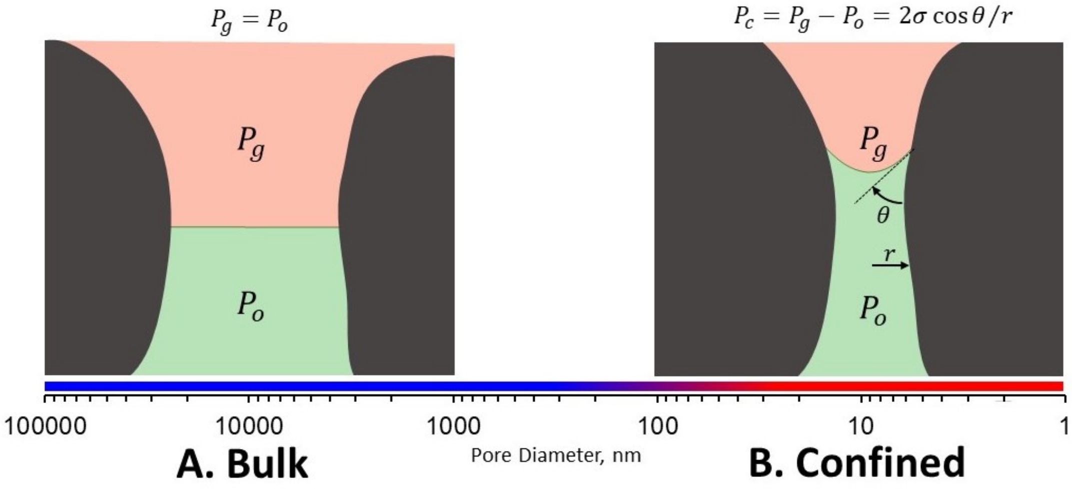

Figure 2.3: Schematic of reservoir fluid contained inside a pore. In large pores (A) the oil and gas phases have a flat interface. At small pore sizes (B) capillary action causes a curvature of the oil/gas interface (adapted from Stimpson 2016).

The curvature of the interface is based on the affinity of the liquid phase for the pore wall material often referred to as “wettability”. The measure of surface wetness is expressed in terms of a contact angle. For an oil-gas mixture the contact angle is measured through the oil phase while for an oil-water mixture the contact angle is measure through the water phase as shown in Figure 2.4.

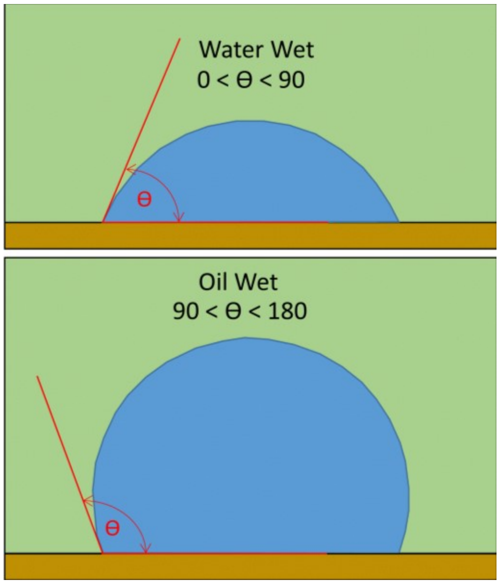

Figure 2.4: Measurement of contact angle through an oil-water mixture.

A smaller angle indicates a greater attraction of the liquid phase to the pore wall with larger angles indicating less attraction. At a contact angle of 90° the interface between the phases is flat. Using the Eagle Ford Oil composition listed in Appendix A, Figure 2.5 shows the impact of pore size and contact angle on the value of capillary pressure.

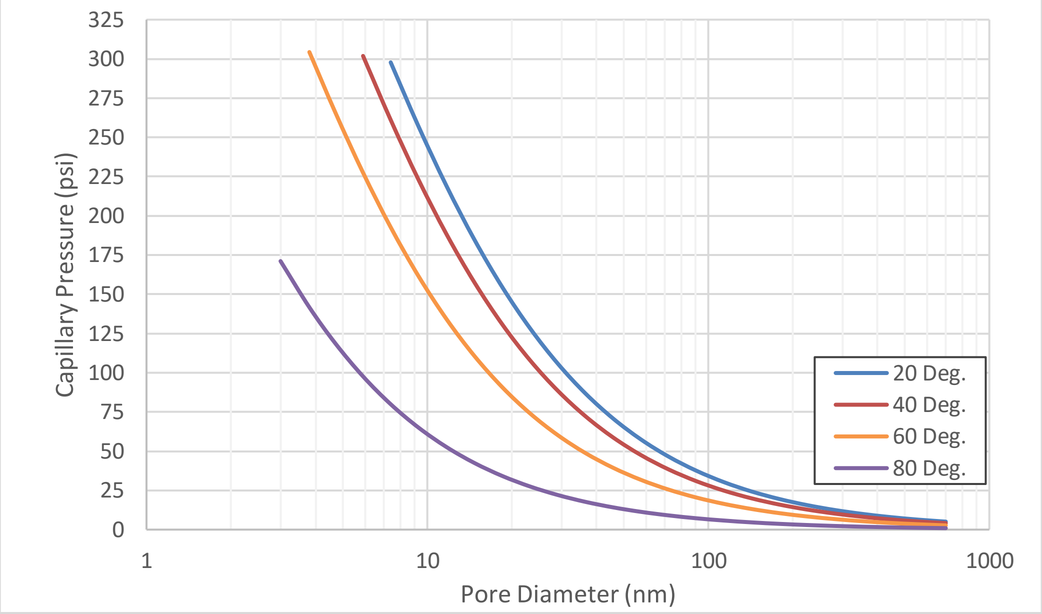

Figure 2.5: Impact of pore diameter and contact angle on capillary pressure for an Eagle Ford black oil at 225°F.

For each contact angle evaluated the capillary pressure increases with decreasing pore diameter. For a given pore size, the capillary pressure increases as contact angle decreases (increasing affinity of the oil phase for the pore wall).

The contact angles values evaluated are kept at less than 90°. At a contact angle of 90° the capillary pressure will be zero at any pore size as per Eq. 2.22. The capillary pressure can be calculated for contact angles exceeding 90°, however, this would yield a negative capillary pressure. A negative capillary pressure means that the liquid phase pressure exceeds the vapor phase pressure, as defined in Eq. 2.20. Physically, a contact angle exceeding 90° specifies that the vapor phase has a higher affinity for the pore wall than the liquid phase, also known as a "gas wet" reservoir. When dealing with reservoir fluids this is almost never the case, the pore surface will be oil wet and therefore contact angles will be less than 90°. The results presented in this work will assume an oil wet reservoir in all cases.

2.2.2 Confinement Impact on Phase Composition

As stated earlier, confinement in small pores shifts the VLE from that calculated at bulk conditions. The impact on the calculation of VLE is most clearly seen by examining the calculation of the equilibrium (K) constants. Equation 2.26 below combines Eq. 2.15 with Eq. 2.20 to incorporate the capillary pressure.

$$K_i = \frac{y_i}{x_i} = \frac{\phi_i^l}{\phi_i^v}\frac{p^l}{p^v} = \left(\frac{\phi_i^l}{\phi_i^v}\right)\left(\frac{p^l}{p^l + p_{cap}}\right); \quad for\ i = 1\ to\ Nc \tag{2.26}$$

As the magnitude of the capillary pressure increases the equilibrium constant decreases; this results in a decrease in the fraction of moles in the gas phase at equilibrium. Figure 2.6 below shows oil saturation as a function of pore size. The curve shows the Eagle Ford oil from Figure 2.5 at a contact angle of 40°.

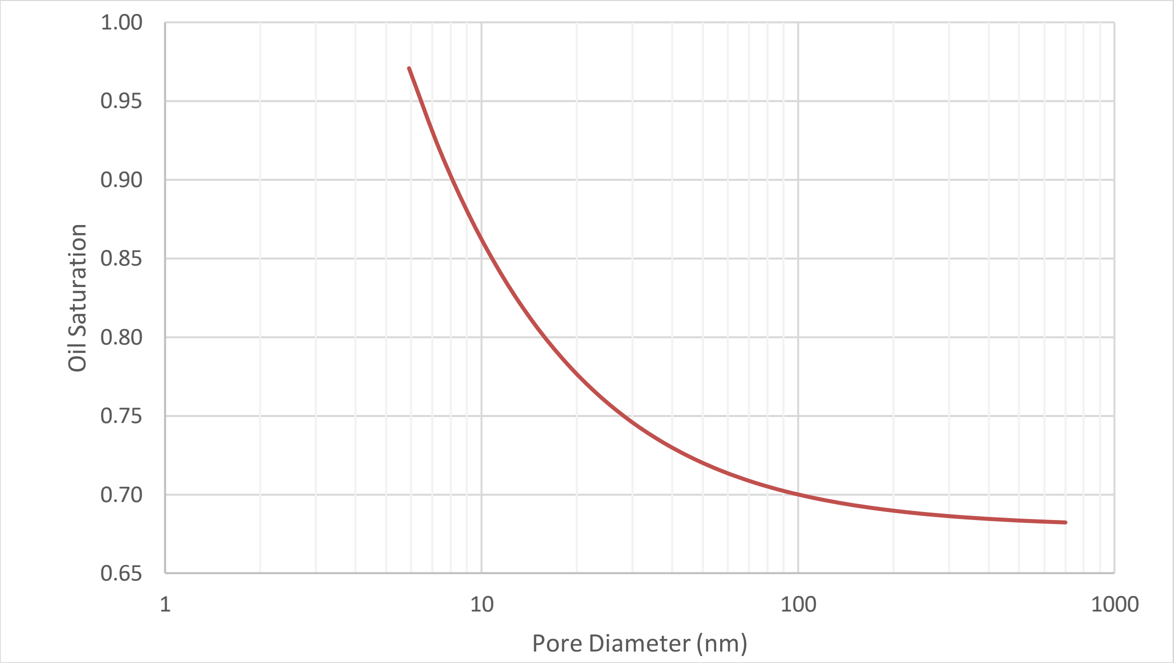

Figure 2.6: Oil saturation as a function of pore size for the Eagle Ford oil sample at a contact angle of 40 degrees.

The oil saturation increases as the pore size decreases. A consequence of this reduction in the equilibrium constants is that the compositions of the oil and gas phases becomes more similar (i.e. oil becomes lighter and gas phase becomes heavier).

For select component in the Eagle Ford oil, Figure 2.7.A shows the molar fraction of that component in the liquid and vapor phases. For these components, vapor and liquid compositions become more similar as the pore size decreases. For methane, there is an increase in methane composition in the vapor phase but a larger increase in the liquid phase. In Figure 2.7.B the corresponding interfacial tension is shown as a function of pore size.

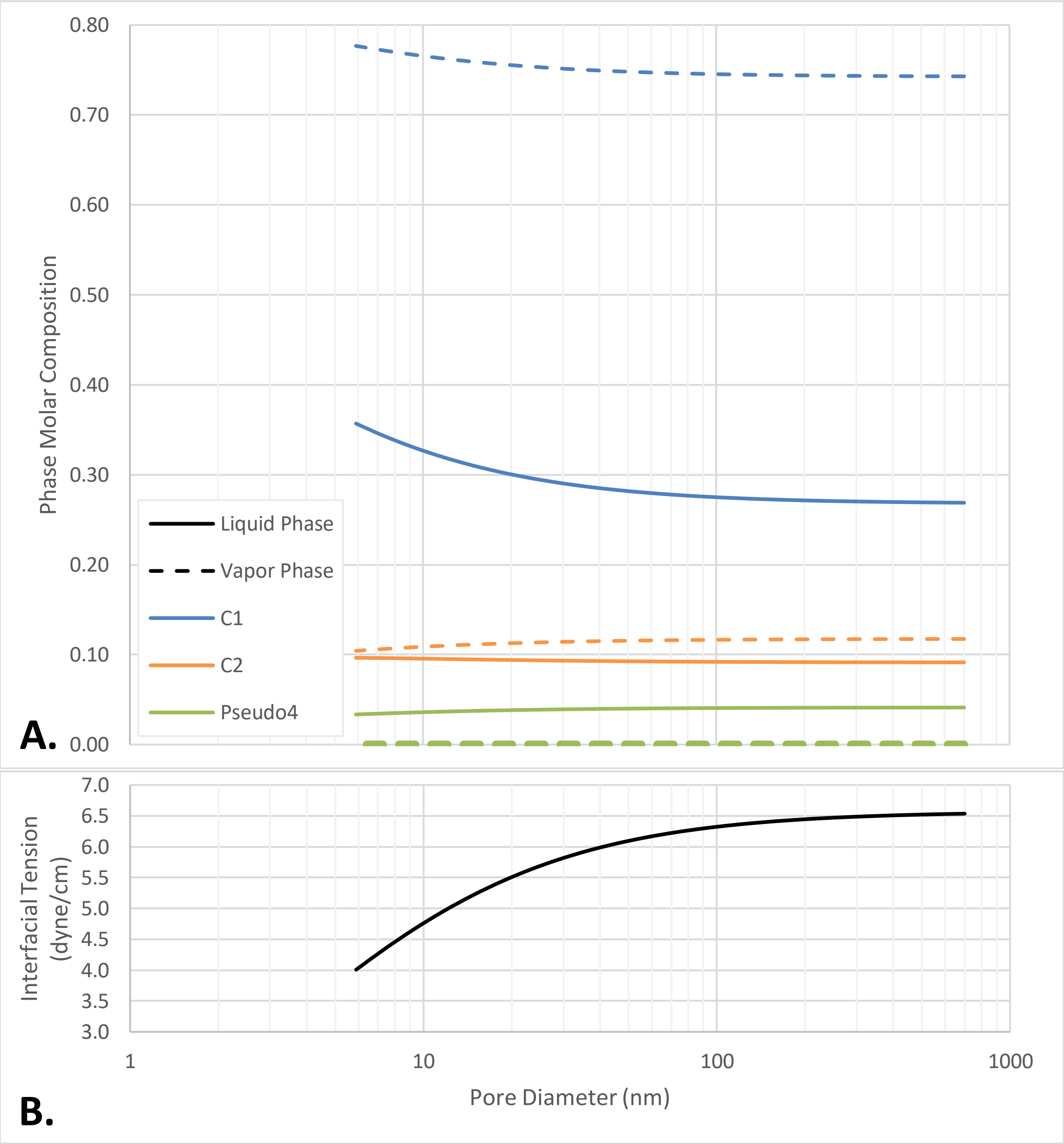

Figure 2.7: A) Liquid and vapor composition of select components as a function of pore size. B) Interfacial tension as a function of pore size. The results for both are generated using the Eagle Ford oil sample at a contact angle of 40 degrees and 225°F.

As the pore size decreases the interfacial tension decreases because the liquid and vapor phases are more compositionally similar.

2.2.3 Confinement Impact on Density and Viscosity

The differences in liquid and vapor phase compositions resulting from confinement cause changes to liquid and vapor density and viscosity values. This is important because this directly affects the mobility of the phases and consequently production. Figures 2.8.A and 2.8.B show the density and viscosity, respectively, of the oil and gas phases for the Eagle Ford oil as a function of pore size.

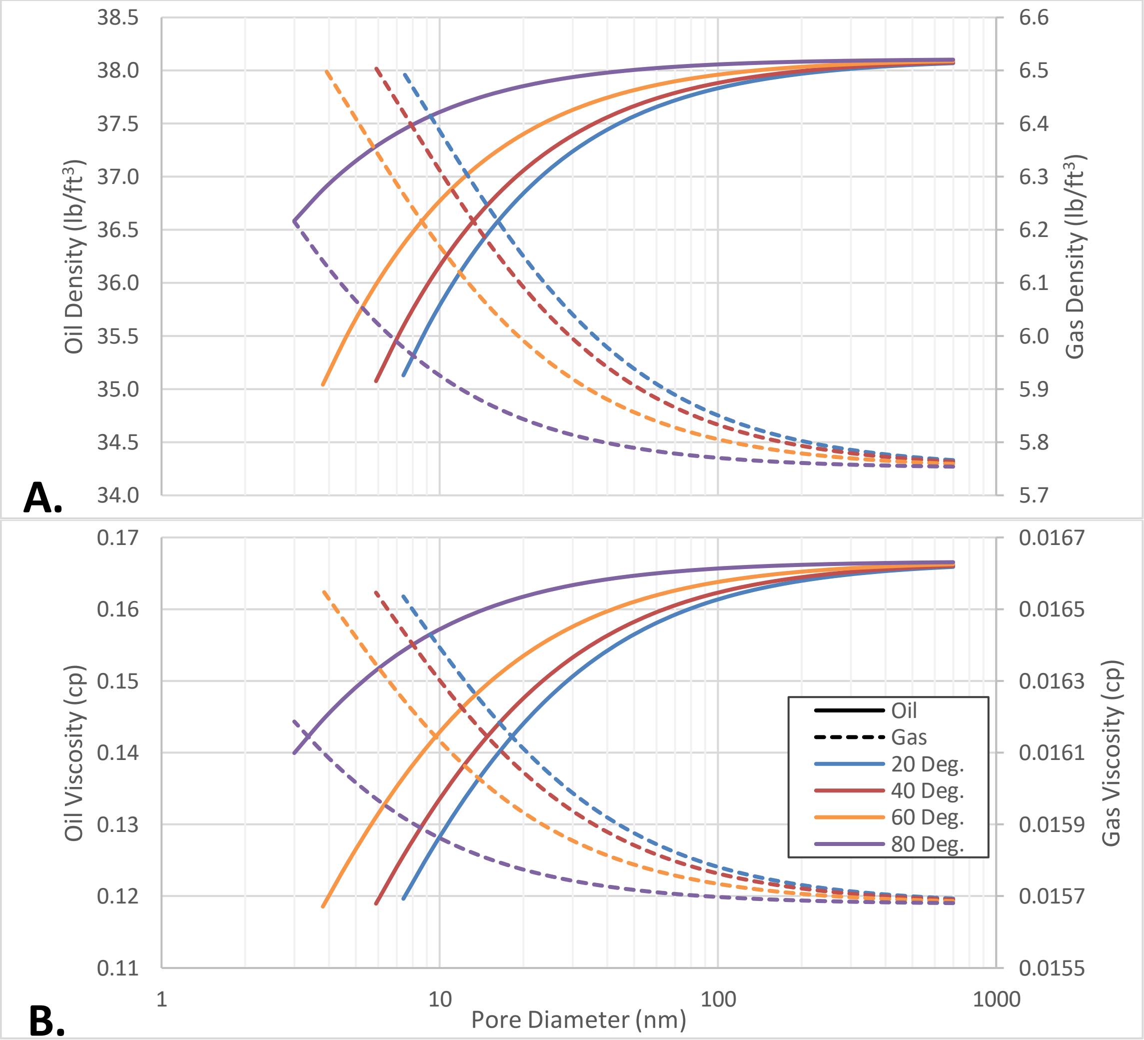

Figure 2.8: Oil and gas phase density (A) and viscosity (B) as a function of pore size for an Eagle Ford oil sample at different contact angles. At smaller pore sizes the oil and gas phase results become more similar.

At smaller pore sizes the oil and gas compositions becomes more similar. This causes a decrease in the liquid phase density and an increase the vapor phase density. This causes a similar trend in the oil and gas viscosities. The changes become more pronounced at smaller contact angles (more oil wet reservoirs). Figure 2.9 further illustrates this effect by showing the ratio of oil to gas density (2.9.A) and oil to gas viscosity (2.9.B).

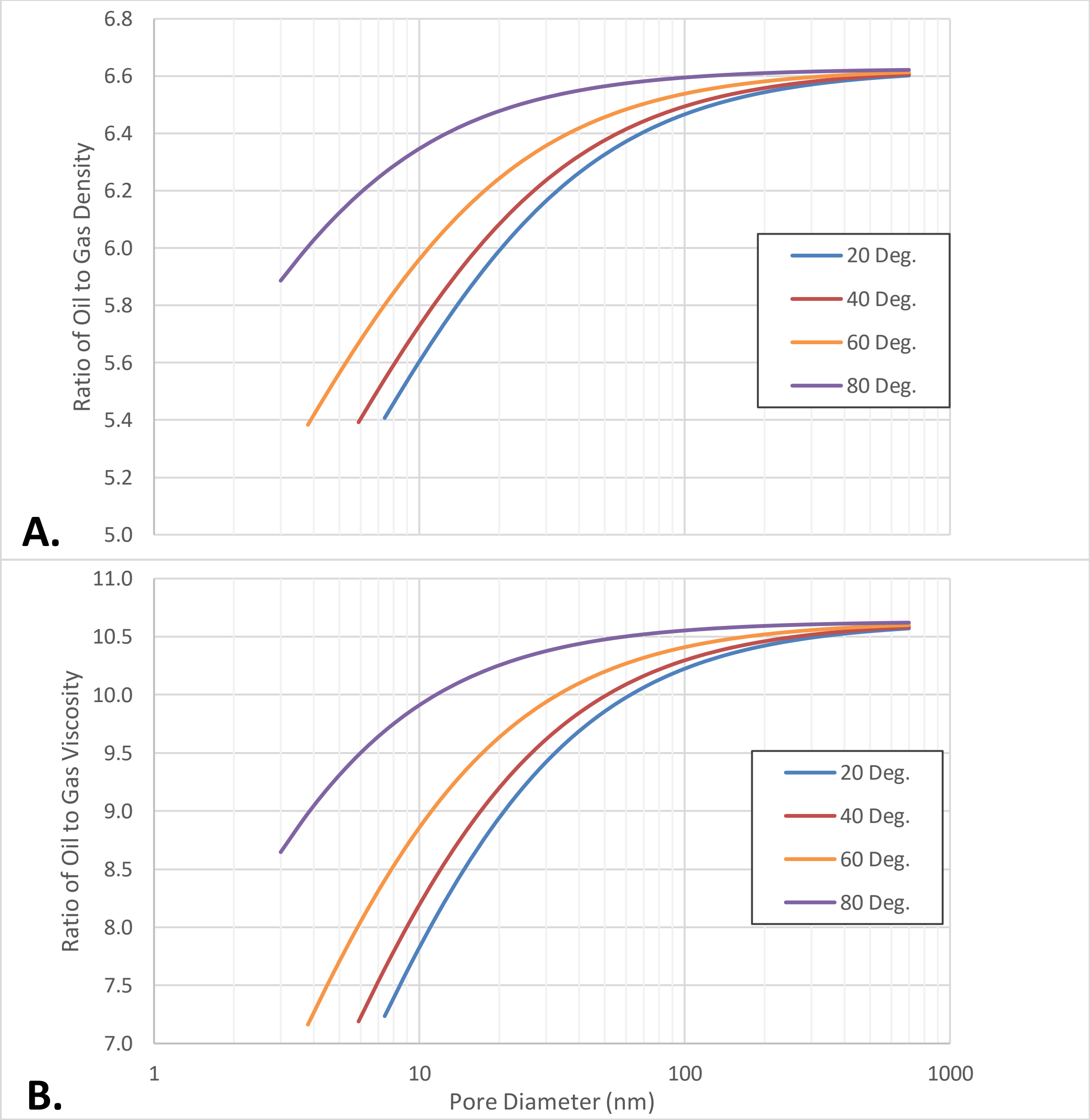

Figure 2.9: Ratio of oil to gas phase density (A) and viscosity (B) as a function of pore size for an Eagle Ford oil sample at different contact angles. At smaller pore sizes the oil and gas phase results become more similar.

The ratio of oil to gas density and viscosity decrease with decreasing pore sizes because the phase compositions become more similar. This effect is exaggerated at smaller contact angles.

3. MECHANISTIC GENERATION OF CAPILLARY CURVES AND RELATIVE PERMEABILITY CURVES

This section describes all aspects of the mechanistic model and provides example results. The mechanistic model functions by approximating a reservoir that undergoes an initial depletion followed by a gas injection and then a secondary depletion, analogous to a "huff and puff" injection process.

3.1 Generation of Capillary Pressure Curves

The mechanistic model described in this work generates a depletion capillary pressure curve and then generates a separate capillary curve for gas injection following the initial depletion. This process can be applied to a single pore or to a collection of pores that represent the pore size distribution within an unconventional reservoir.

3.1.1 Capillary Curve Generation for Single Pore Depletion

To generate a capillary curve for depletion of a single pore size, a process similar to a Constant Volume Depletion (CVD) is utilized. The hydrocarbon composition being analyzed undergoes a number of equally spaced pressure reduction steps. Each pressure decrease results in an expansion of the hydrocarbons, this increase in volume will be referred to as "excess volume" in this work. A volume of hydrocarbons equal to the excess volume is then removed which causes the pore volume to return to the volume at the start of the pressure step, hence the comparison to a constant volume depletion. The ratio of oil and gas removed is controlled by the specified production setting for the run known as a “production mode”. The production modes are described in detail in Section 3.1.2 below. The steps in the depletion process are summarized as follows:

1) Record the volume of hydrocarbons in the pore at the starting pressure.
2) Decrease the pressure in the pore. The pressure steps are equally spaced between the starting and ending pressure (Eq. 3.1). The number of depletion steps (N_D) is specified.

$$\Delta P\ (psi) = \frac{P_{init}\ (psia) - P_{fin}\ (psia)}{N_D} \tag{3.1}$$

3) Perform a flash calculation on the fluid in the pore.
4) Calculate the expanded pore volume.
5) Record the oil saturation in the pore and the capillary pressure.
6) Remove hydrocarbons from the pore until the volume returns to the initial volume calculated in step 1 above. The amount of volume removed is the excess volume. The exact composition removed from the pore depends on the composition of the fluid and the production mode selected. The volumes of oil and gas depleted and the molar compositions of the oil and gas phases are recorded for each step.
7) Return to step 2 above and repeat the process until the pressure reaches the specified end pressure.

One iteration of this process is shown schematically in Figure 3.1 below. In this case, the excess volume is removed entirely through gas production but this will not always be the case and depends on the specified production mode.

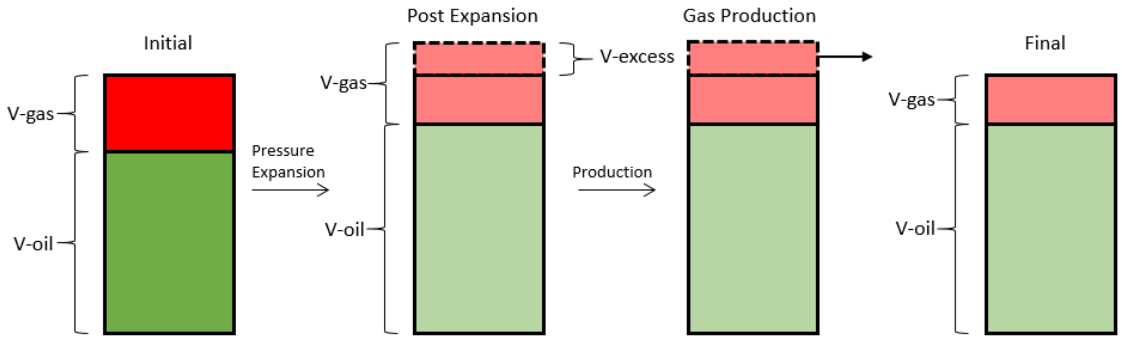

Figure 3.1: Schematic representation of the pore depletion process. One iteration of the process is shown progressing from left to right.

Once the iteration process is complete, the capillary pressure for each pressure step is plotted as a function of the corresponding oil saturation. This yields a capillary pressure curve that is unique to the pressure range, fluid composition, pore size and production mode specified. Figure 3.2 below shows two sample capillary curves generated from an Eagle Ford oil composition (see Appendix A) for two different pore sizes. Each data set was obtained through a separate calculation and only combined to illustrate the impact of pore size on the generated curves. The constant composition production mode, which is explained in the following section, is used to generate this curve. Each point in the figure corresponds to a pressure step. The number of depletion pressure steps (N_D) can impact the shape of the curve especially when only a small number of steps is specified. Therefore, it is important that a sufficiently large number of steps is specified for the run.

A sufficient number of steps is specified when the addition of more steps has little impact on the recovery and capillary results.

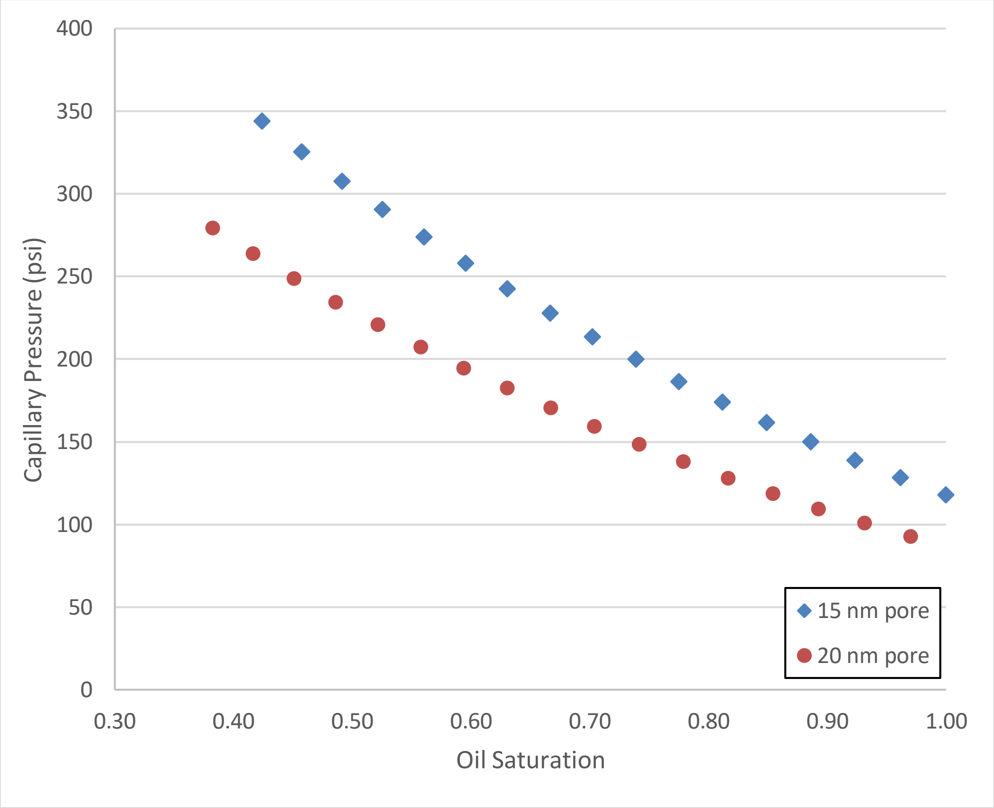

Figure 3.2: Capillary pressure curve for depletion of a single pore filled with Eagle Ford oil at a temperature of 220°F and a contact angle of 30°. The depletion covers a pressure range of 2200-600 psi using 17 pressure steps. Each point represents data from a separate depletion pressure step.

3.1.2 Description of Production Modes

The depletion process described in Section 3.1.1 above requires the removal of excess hydrocarbon volume following each pressure decrease. The ratio of oil and gas volume removed is determined by the production mode specified for the particular run. Different production modes are utilized to simulate the effects of differing production schemes in a real world reservoir.

The different production modes can yield different capillary curves for the same starting hydrocarbon composition at the same starting pressure and temperature. The mechanistic model was created with five different production mode options. Each mode is described below along with a schematic representation for depletion. It is noted that the same production modes are used for the injection portion of the run and operate analogously.

Gas Production or Oil Production

These are two separate production settings but function similarly. If the gas production mode is specified, only gas is removed from the pore. The amount of gas removed from the pore during each step is equal to the excess volume for that step. Gas production is shown schematically in Figure 3.3.A below. Conversely, if oil production is specified, only oil is removed from the pore as shown in Figure 3.3.B below. If the oil or gas volume is less than the excess volume for that step, then no hydrocarbons are removed during that step. It is noted that in a real life setting, for production to remain exclusively single phase oil or single phase gas the pressure range for the run must be above the saturation pressure of the fluid.

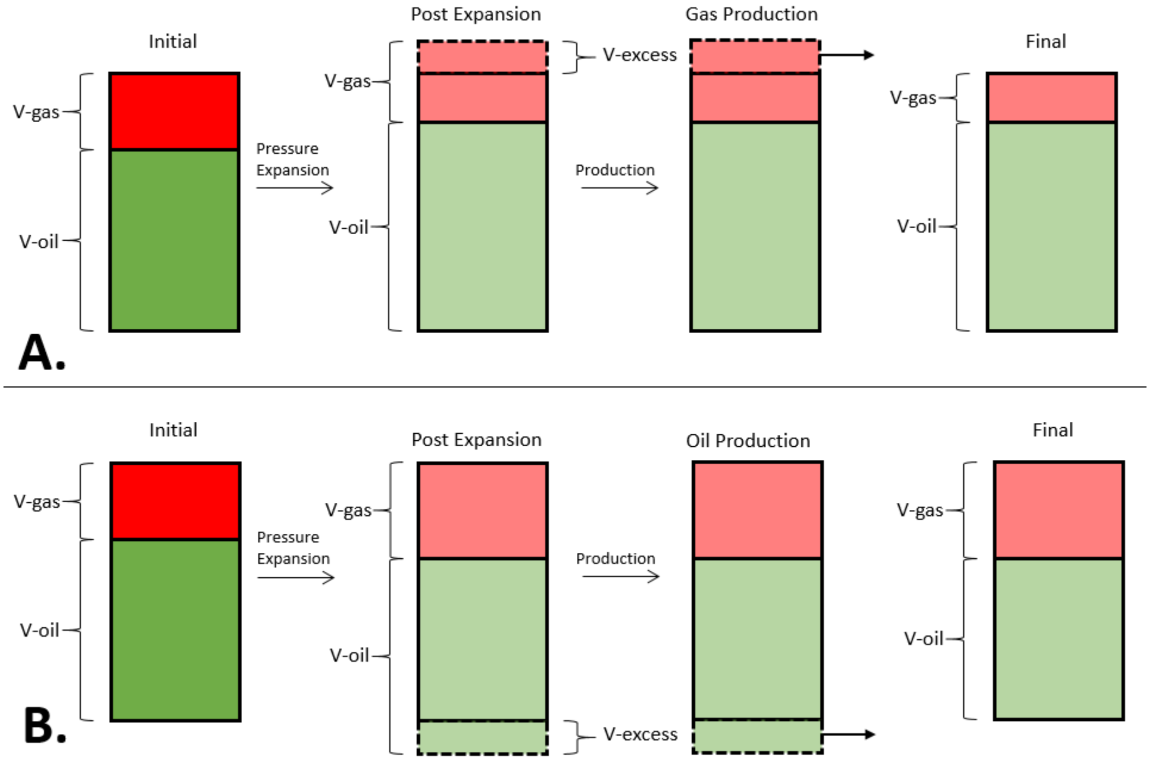

Figure 3.3: Schematic for depletion of a single pore using the gas production mode (A) and oil production mode (B). The two modes are separate and only one mode is used at a time.

<u>Preferential Gas Production</u>

This production mode is similar to the gas production mode described above with a key difference. If the gas volume in the pore is greater than the excess volume, only gas will be produced as shown in Figure 3.4.A below. If the gas volume is less than the excess volume, all the available gas will be removed and oil will be removed to make up the remainder of the excess volume, shown in Figure 3.4.B.

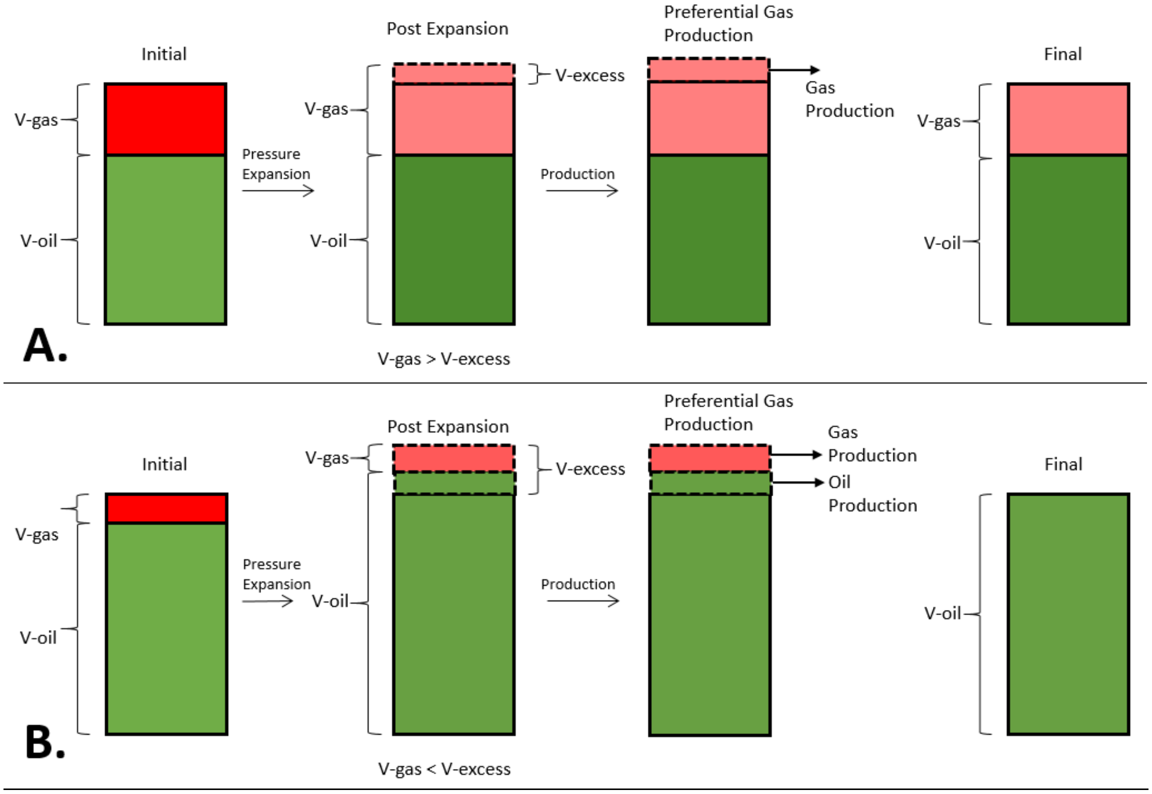

Figure 3.4: Schematic for preferential gas production. If gas volume in the pore is greater than excess volume, only gas will be produced (A). If gas volume is less than excess volume, all available gas will be produced and the remainder of the excess volume will be produced as oil (B).

Constant Composition

This production mode produces oil and gas volumes such that the total molar composition within the pore remains constant. Volumes of oil and gas produced (Eq 3.2 and Eq. 3.3 respectively) are a function of excess volume and the oil saturation in the pore during that particular step. These volumes are evaluated at reservoir temperature and the pressure inside the pore in that particular step.

$$Oil\ Production\ (T_{res}, P_{pore}) = (Vexcess)\left(\frac{V_{oil}}{V_{oil} + V_{gas}}\right) \tag{3.2}$$

$$Gas\ Production(T_{res}, P_{pore}) = (Vexcess)\left(\frac{V_{gas}}{V_{oil} + V_{gas}}\right) \tag{3.3}$$

Additionally, the lbmols of oil and gas produced are recorded in order to conserve material balance. Constant composition production is shown schematically in Figure 3.5 below.

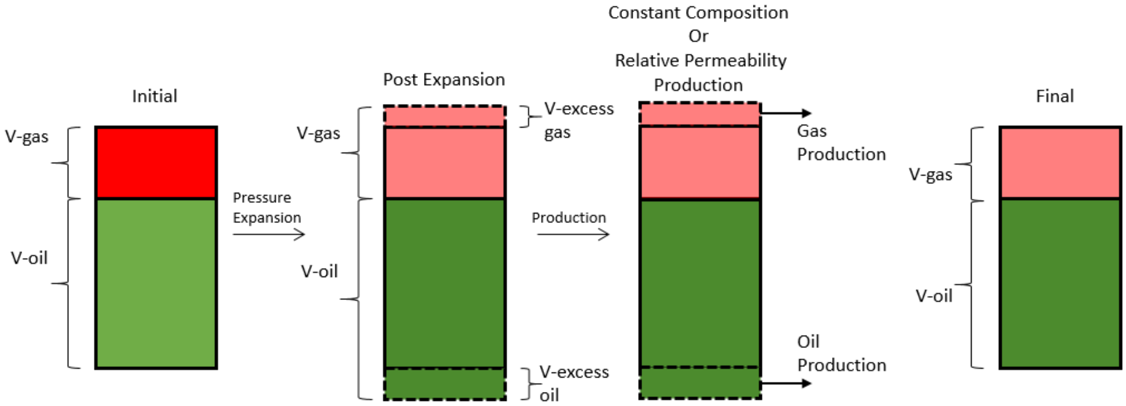

Figure 3.5: Schematic for Constant Composition or Relative Permeability production. The amounts of gas and oil removed (V-excess gas and V-excess oil, respectively) are calculated differently for Constant Composition and Relative Permeability modes.

Relative Permeability

This production mode uses relative permeability curves and oil saturation to determine the amounts of oil and gas produced in each step. This production mode is used to simulate actual production from a reservoir. The relative permeability curves can either be directly specified or they can be calculated from capillary pressure data as described in Section 3.2 below. This option is more rigorous than specifying relative permeability values independently.

The volumes of oil and gas produced are based on the ratio of the mobility of each phase as defined in Eq. 3.4 to 3.6 where the relative permeability is obtained from the supplied curves and the viscosities of each phase are obtained from the flash calculation using the Lorentz-Bray-Clark (1964) correlation.

$$\lambda_{o/g} = \frac{(k_{r,o/g})(k)}{\mu_{o/g}} \tag{3.4}$$

$$Oil\ Production = (Vexcess)\left(\frac{\lambda_o}{\lambda_o + \lambda_g}\right) \tag{3.5}$$

$$Gas\ Production = (Vexcess)\left(\frac{\lambda_g}{\lambda_o + \lambda_g}\right) \tag{3.6}$$

The relative permeability production is shown schematically in Figure 3.5 above. Since the saturation in the pore changes with each pressure step the amounts of oil and gas removed are recalculated in each depletion pressure step.

3.1.3 Capillary Curve Generation for Single Pore Injection

Gas injection begins after the final depletion step has been completed. Therefore, the total molar composition and pressure inside the pore at the start of injection is equal to the composition and pressure at the end of the final depletion step.

Gas is injected into the rigid, constant volume pore, resulting in an increase in pressure inside the pore. Hydrocarbons are then produced from the pore until the pressure returns to the pressure at the end of the depletion run. It is possible to simulate multiple injection steps per run. The injection gas composition and molar injection amount per step is specified before the run starts and remains constant throughout the run. One iteration of the injection process, which is shown in Figure 3.6 below is summarized. The frames listed in each step below refer to Figure 3.6.

1) Record the volume of hydrocarbons in the pore at the end of the depletion (frame a).
2) Add the injection gas to the pore (frame b). The injection gas amount (expressed in lbmols) and composition is specified at the start of the mechanistic model run.
3) Estimate the new pressure inside the pore due to the addition of the injected gas (frame c).
4) Calculate multiple equally spaced pressure steps. The steps are equally spaced in between the pressure estimated in step 3 above and the pressure in step 1 before the injection gas was added.
5) Reduce the pressure in the pore from the pressure in step 3 to the next lower pressure step. This results in an expansion of the hydrocarbons inside the pore (frame d).
6) Perform a flash calculation at the pressure in step 5.
7) Record the oil saturation in the pore and the capillary pressure.
8) Calculate the expanded pore volume.
9) Remove hydrocarbons from the pore until the volume returns to the initial volume calculated in step 1 above (frame e). The selected production mode specifies the relative volumes of oil and gas removed from the pore. The

volumes of oil and gas depleted and the molar compositions of the oil and gas phases are recorded for each step.

10) Return to step 5 above and repeat the process for the next four decreasing pressure steps.

11) If multiple injection steps are specified for the run, the process from step 2 to 10 is repeated for each injection step.

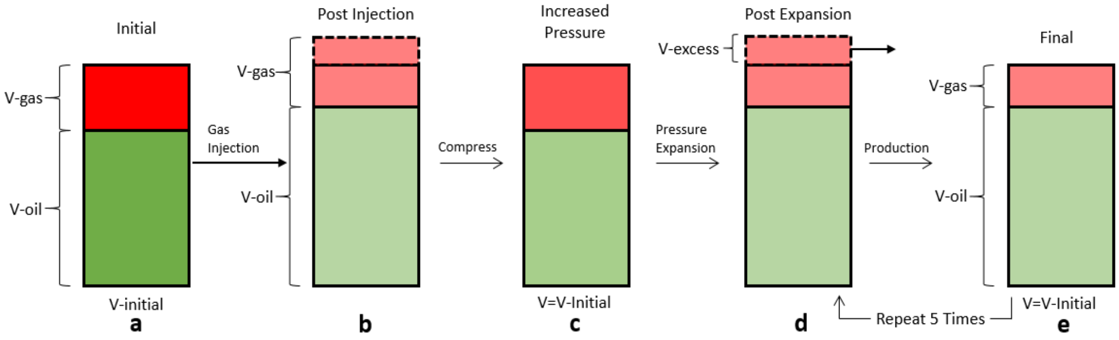

Figure 3.6: Schematic representation of pore injection process. One iteration of the process is shown progressing from left to right. Frames d and e are repeated 5 times for each injection step. If multiple injection steps are specified for the run, the entire process (frames a-e) is repeated for each injection step.

Once the iteration process is complete, the capillary pressure data is plotted as a function of the corresponding oil saturation. This yields a capillary pressure curve for the injection conditions and pore size evaluated. Figure 3.7 below shows two sample capillary curves generated from an Eagle Ford oil composition (defined in Appendix A) that has undergone a depletion followed by CO_2 injection. The curves show the data from the injection portion of two separate runs for two different pore sizes to illustrate the impact of pore size on the capillary results.

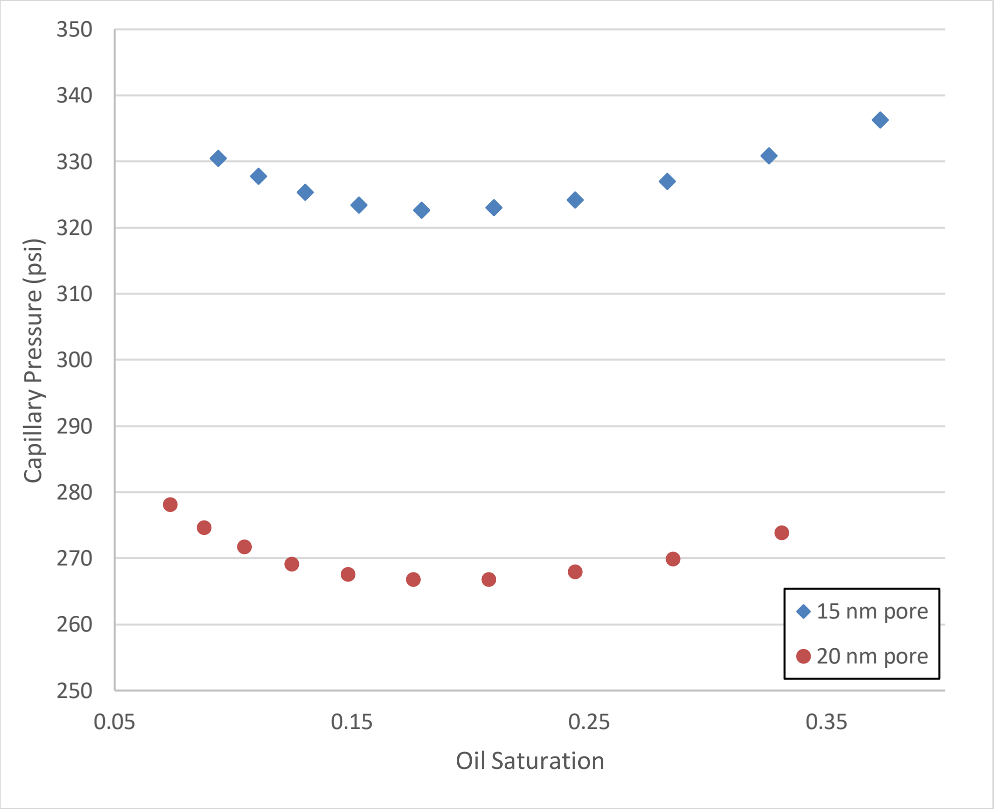

Figure 3.7: Capillary pressure curve for CO_2 injection of single pore following depletion of Eagle Ford oil at 225°F with a contact angle of 30°. Each point represents data from a separate injection step. As more CO_2 is injected the saturation decreases.

As stated earlier, each time the mechanistic model is run, a depletion and injection are run in series. Figure 3.8 shows the data from Figures 3.2 and 3.7 combined to show the results of an entire run.

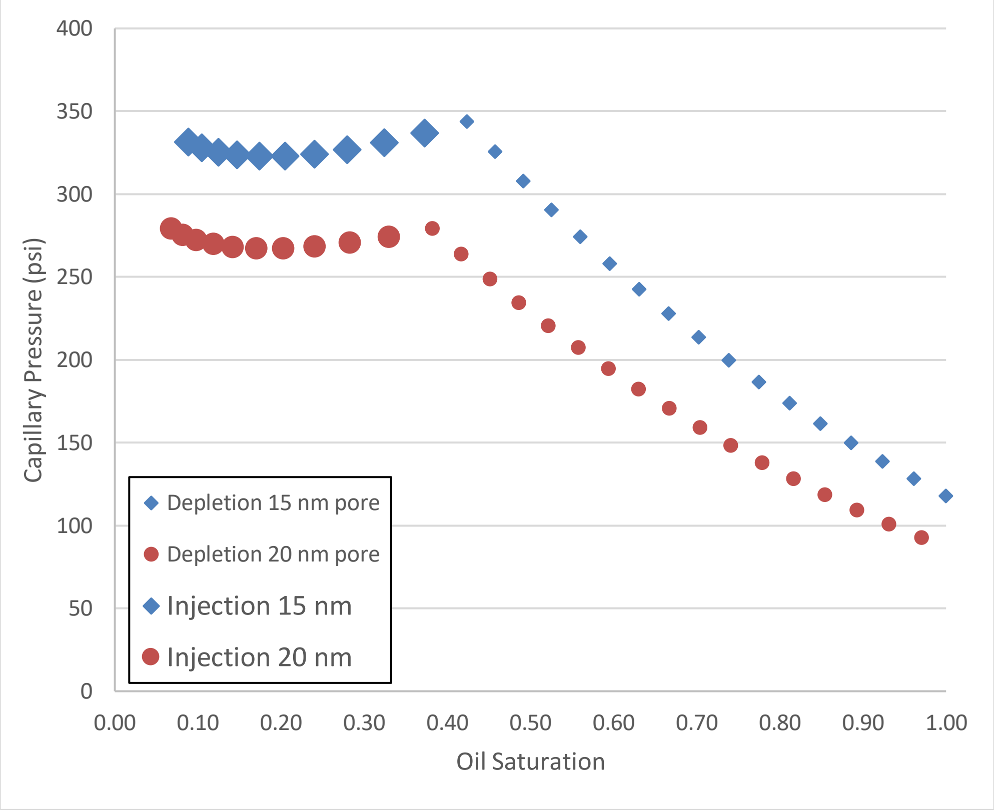

Figure 3.8: Combined capillary pressure curve for depletion of an Eagle Ford Oil (Fig. 3.2) followed by injection of CO_2 (Fig. 3.7). The 15 nm line represents a single mechanistic model run with the depletion portion of the run (smaller diamonds) starting at an oil saturation of 1.0 and ending at an oil saturation of 0.42. The injection portion of the run (larger diamonds) starts at a saturation of 0.42 and ends at a saturation of 0.09.

3.1.4 Selection of Pore Sizes for Multiple Pore Capillary Curves

Capillary pressure curves can also be generated for a collection of pore sizes representing a reservoir. The pore sizes are selected such that they represent the pore size distribution found within a reservoir. This allows for the creation of a capillary pressure curve that represents the depletion of an entire reservoir instead of a single pore size as described in Section 3.1.1 above.

Lognormal Distribution

The procedure for generating capillary curves will work with any pore size distribution but this work assumes a lognormal pore size distribution. This is based on the work of Pommer (2014) which evaluated pore size distributions from multiple Eagle Ford core samples and found that in most cases the pore sizes resulted in a lognormal distribution. A lognormal distribution is defined as a data set that has a normal distribution of the natural logarithms of the points in the data set. Consequently, the probability density function (*f(x)*) for a lognormal distribution, which is defined in Eq. 3.7, has a mean value (μ_{ln}) and a standard deviation for the data set (σ_{ln}).

$$f(x) = \left(\frac{1}{x}\right)\left(\frac{1}{\sigma_{ln}\sqrt{2\pi}}\right)e^{\left(-\frac{(\ln(x)-\mu_{ln})^2}{2\sigma_{ln}^2}\right)} \tag{3.7}$$

A sample lognormal distribution is shown in Figure 3.9 below.

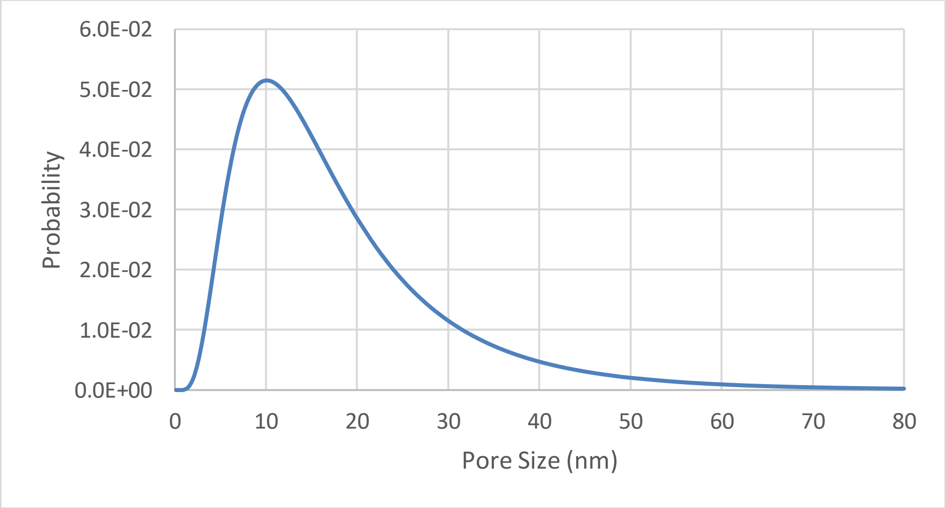

Figure 3.9: Probability density function for a lognormal distribution with log mean of 2.708 nm (mean of 15 nm) and a standard deviation of 0.63 nm.

The cumulative probability function (*F(x)*) for a lognormal distribution is calculated from Eq. 3.8, where erf is the Gauss error function.

$$F(x) = 0.5 + 0.5\,\mathrm{erf}\left(\frac{\ln x - \mu_{ln}}{\sigma\sqrt{2}}\right) \tag{3.8}$$

The cumulative probability function corresponding to the probability function in Figure 3.9 is shown in Figure 3.10 below.

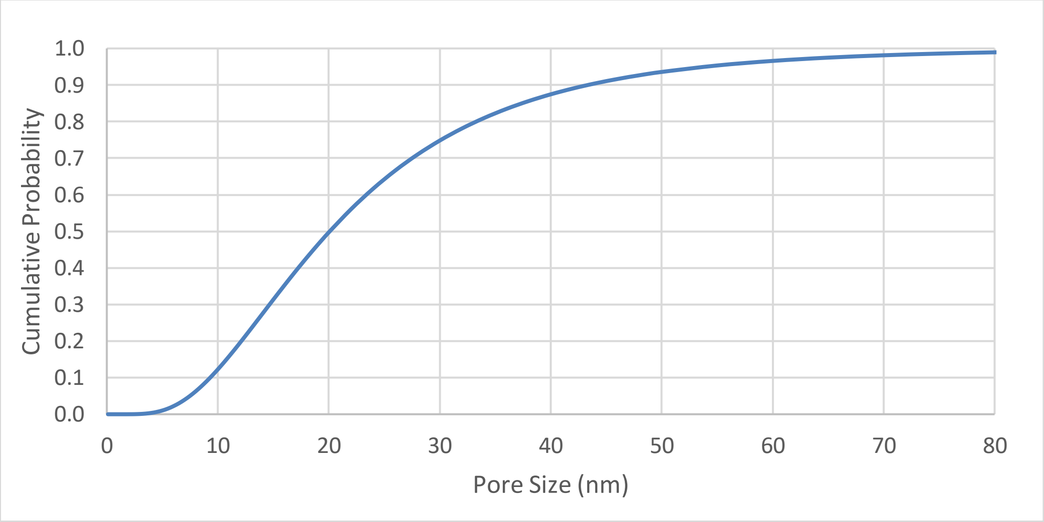

Figure 3.10: Cumulative probability density function for a lognormal distribution with log mean 2.708 nm and standard deviation of 0.63 nm.

Selection of Pore Sizes

To represent the cumulative pore size distribution shown in Figure 3.10 above using a finite number of pores, pore sizes must be assigned such that they match the specified cumulative distribution. The number of pores used (N) is specified before the mechanistic model run starts. To represent the distribution using N pores, each pore must represent 1/Nth fraction of the cumulative probability. A probability located in the midpoint of the fraction is selected and then the corresponding pore size can be read from the cumulative distribution. Figure 3.11 below shows an example of how to divide the cumulative probability distribution from Figure 3.10 into five pore sizes. Each pore size represents 20% (1/5th) of the total number of pores.

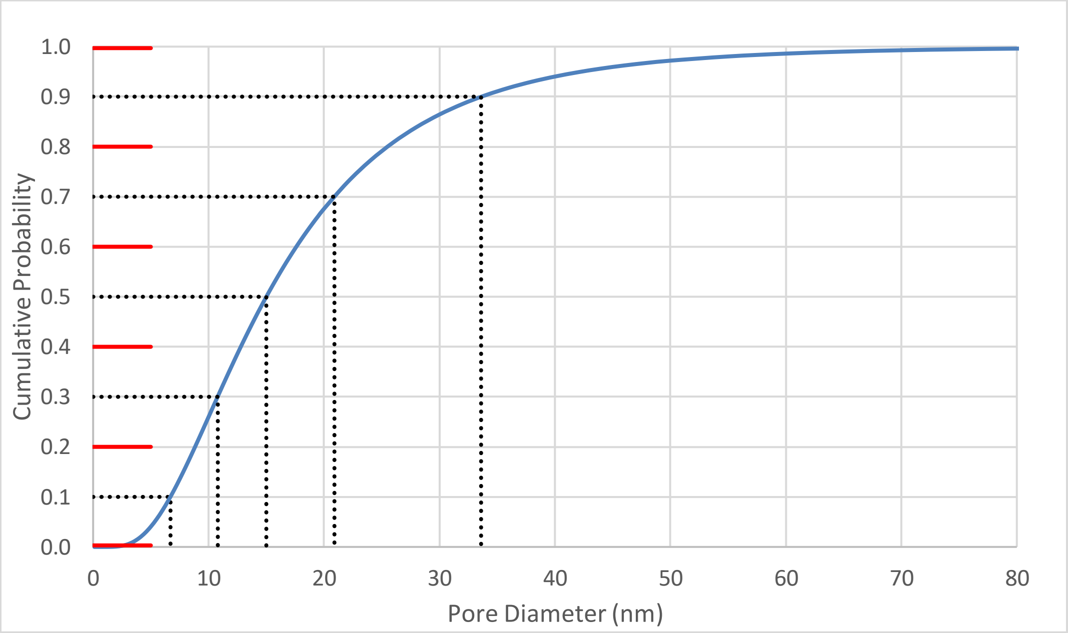

Figure 3.11: Determination of pore sizes that represent a cumulative probability density function for a lognormal distribution with log mean 2.708 nm and standard deviation of 0.63 nm using 5 pores. The short red lines show how the cumulative probability is split into 5 equally spaced segments. The dashed vertical lines indicate the pore size assigned to each of the 5 pores.

3.1.5 Capillary Curve Generation for Depletion of a Pore Size Distribution

To generate a capillary curve for the depletion of an entire pore size distribution, the distribution is treated as a collection of individual pores and calculated as follows:

1) The pore sizes representing the distribution are assigned as described in Section 3.1.4 above.

2) For each pore size, a depletion is run as described in Section 3.1.1 above which creates a separate capillary curve for each pore.
3) Individual capillary curves are combined into a single curve. Two averaging methods are used in this work (step 3a or 3b). Both methods use the same capillary pressure values from the individual curves but use a slightly different approach in averaging the data to produce a single curve. The method in step 3a averages data based on oil saturation while the method in step 3b averages based on oil pressure.
    3a. The first averaging method iterates through oil saturation values and then uses linear interpolation to determine the corresponding capillary pressure for each pore at the specified oil saturation. The capillary pressures are then weighted by the pore volume represented by each pore size and then added together to determine the capillary pressure for the distribution. This yields a capillary pressure curve that represents the average capillary pressure for each of the pores as a function of oil saturation. The oil saturation range evaluated ranges between the highest and lowest oil saturations experienced by the individual pores. This combination method is used for the generation of relative permeability curves described in Section 3.2 below.
    3b. The second averaging method iterates oil pressure values and then uses linear interpolation to determine the corresponding capillary pressure for each pore at the specified oil pressure. The oil saturations as a function of

oil pressure are also determined. Similar to method 3a) above, the capillary pressures and oil saturations are then weighted by the pore volume. The averaged capillary pressure is plotted against the averaged oil saturation values. The resultant capillary pressure curve represents the average capillary pressure for a depleting reservoir.

Figure 3.12 below shows the individual capillary pressures for each pore size and the combined capillary pressure curves resulting from the two averaging methods described. The individual curves are generated from depletion of the pore sizes determined in Figure 3.11 above.

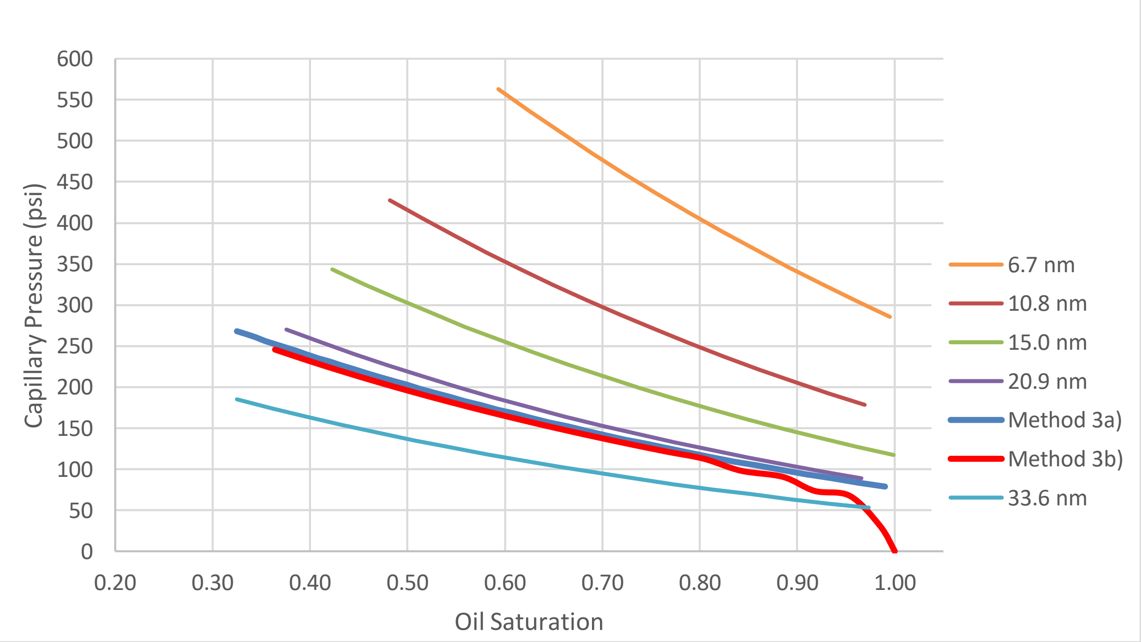

Figure 3.12: Capillary pressure curves for individual pores and the two combined capillary curves for a depletion run using an Eagle Ford oil across a pressure range of 2200-600 psia. The pore size distribution is lognormal with a log mean of 2.708 nm and standard deviation of 0.63 nm.

The two averaging methods yield different curves. The difference is most apparent at high oil saturation. When averaging based on oil saturation (method 3a), an oil saturation is selected and the capillary pressure for each pore at the specified saturation is used in the averaging. This explains why the curve for this method begins at a non-zero value.

This is in contrast to the averaging method based on oil pressure (method 3b). At high oil pressure, all pores are single phase resulting in a capillary pressure of zero. As the oil pressure is reduced due to depletion, the largest diameter pores pass the saturation pressure first followed by progressively smaller pores. As each pore enters a two-phase condition, a non-zero capillary pressure is included in the averaging calculation which causes the sharp increase in the method 3b capillary curve between a saturation of 1-0.9. When all pores have entered a two phase state, the method 3a and method 3b curves match more closely. To illustrate this progression, the oil saturation for each pore size in Figure 3.12 is shown as a function of oil pressure in Figure 3.13 below.

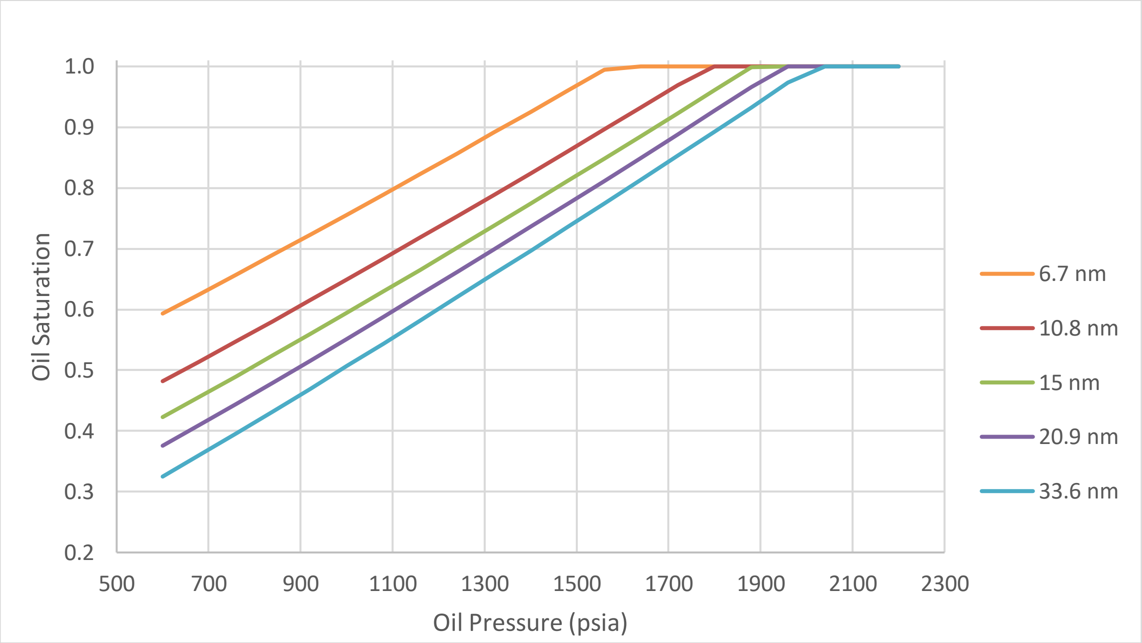

Figure 3.13: Oil saturation as a function of oil phase pressure for individual pores resulting from a depletion run. The pore size distribution is lognormal with a log mean of 2.708 nm and standard deviation of 0.63 nm. The Eagle Ford oil composition from Appendix A is used with a temperature of 225°F and a contact angle of 30°.

3.1.6 Capillary Curve Generation for Injection of a Pore Size Distribution

The capillary curve for injection is calculated using the following steps:

1) The pore sizes representing the distribution are assigned as described in Section 3.1.4 above.
2) A depletion is run for each pore size. The pressure range and number of depletion steps are specified as inputs to the model run.
3) Following the end of the depletion, a pore injection is run for each pore as described in Section 3.1.3. The injection gas composition, lbmols injected per step and number of injection steps are specified inputs to the model run. The capillary data for each individual pore is recorded.

4) Individual capillary curves are combined into a single curve. The curves can be averaged using based on oil saturation or oil phase pressure, similar to depletion averaging methods 3a and 3b, respectively, described in Section 3.1.5.

An important difference between running a pore injection for a pore distribution compared to a single pore is the allocation of the injection gas between the multiple pores. For a single pore run, the total injection gas amount goes to a single pore. For multiple pores, the total injection gas amount is distributed amongst the pores. The way the gas is distributed can impact the capillary curve that is generated. The following distribution options were considered over the course of this research:

<ins>Volume Distributed</ins> – The injection gas is split amongst the pores based on the fraction of total pore volume represented by each pore size. This ratio is calculated at the start of the mechanistic model run and does not change throughout the injection run.

<ins>Molar Distributed</ins> – The injection gas amount is split proportional to the fraction of total hydrocarbon molecules contained in each pore size at the end of the depletion run. For example, if the largest pore size contains 30% of the hydrocarbon molecules at the end of the depletion run, it will receive 30% of the total injected gas. This ratio is calculated once at the end of the depletion portion of the run. The amount (fraction of lbmols) of gas assigned to each pore is constant and does not change throughout the injection run even if there are multiple injection steps.

Gas Saturation Distributed – The injection gas amount is split proportional to the fraction of total gas volume contained within each pore. This fraction is recalculated at the end of each injection step. Therefore, the amount of gas injected into each pore can differ between injection steps based on how the oil saturation in each pore changed during the previous injection step.

Figure 3.14 below shows the individual capillary pressures and the combined capillary pressure curves for injection of the pore sizes determined in Figure 3.11 above. For this injection run, the volume distributed method was used to split the injection gas.

For the combined curve, the two averaging methods yield a similar capillary pressure curve. The combined curve generated using the oil saturation method (method 3a) covers a larger oil saturation range because the range is selected to span from the highest to the lowest oil saturations of the individual curves.

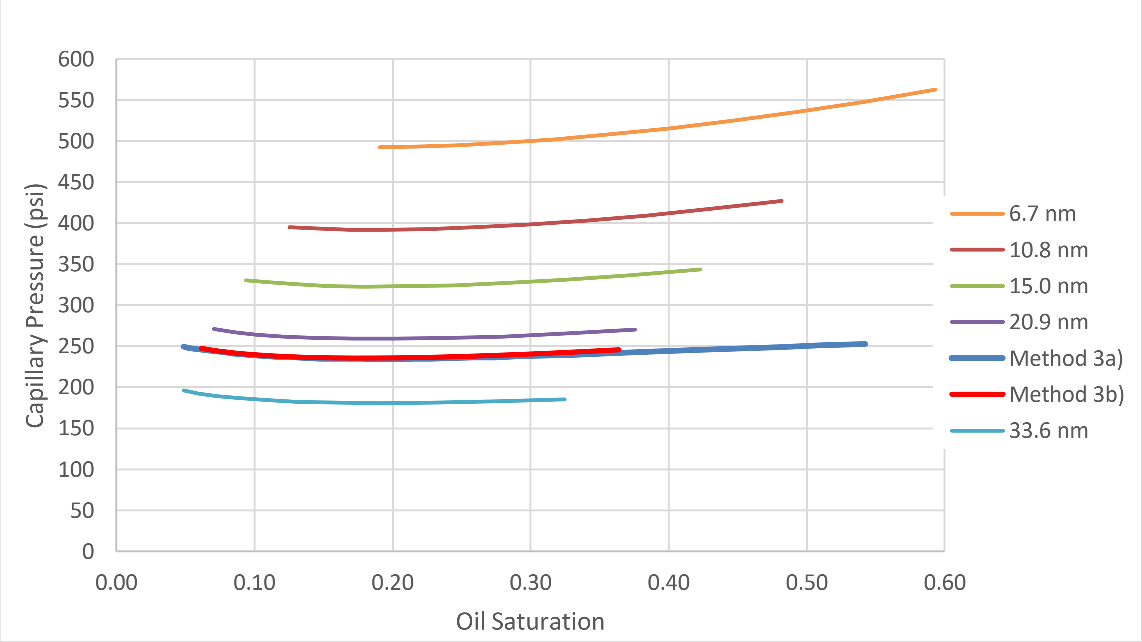

Figure 3.14: Capillary pressure curves for individual pores and the combined capillary curves for a CO_2 injection run. The pore size distribution is lognormal with a mean of 2.708 nm and standard deviation of 0.63 nm. The injection gas is distributed based on the volume distributed method with 10 injection steps used with 5 moles of CO_2 injected per step for every 100 moles of hydrocarbons initially in place.

When the depletion capillary data from Figure 3.12 is combined with the injection capillary data in Figure 3.14, the capillary pressure of the entire depletion and injection run can be seen (Figure 3.15). The depletion run starts with an oil saturation of 1.0. As the depletion oil pressure decreases, the oil saturation decreases. The discontinuity in the curves indicates the start of the injection portion of the run. The combined curve is generated using the oil pressure averaging method (method 3b).

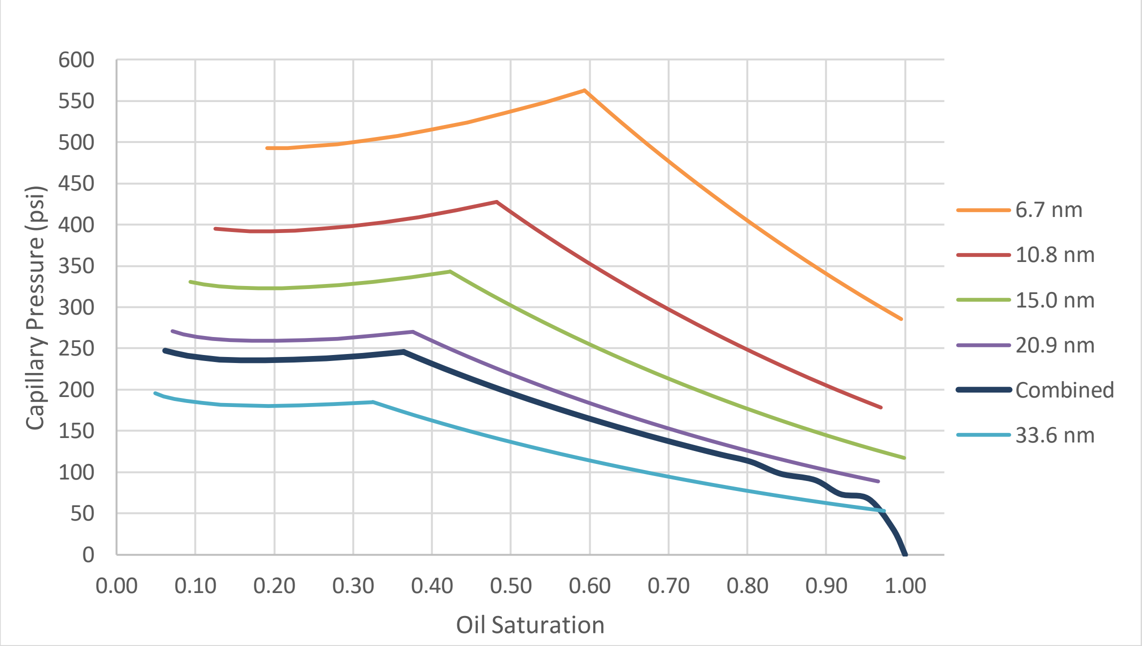

Figure 3.15: Combined capillary pressure curves for individual pores and the combined capillary curve for full mechanistic model run (depletion (Fig. 3.12) and injection (Fig. 3.14) combined). The pore size distribution is lognormal with a mean of 2.708 nm and standard deviation of 0.63 nm.

Figure 3.16 below provides a flowchart showing how the mechanistic model functions. The various portions of the model run sequentially from top to bottom.

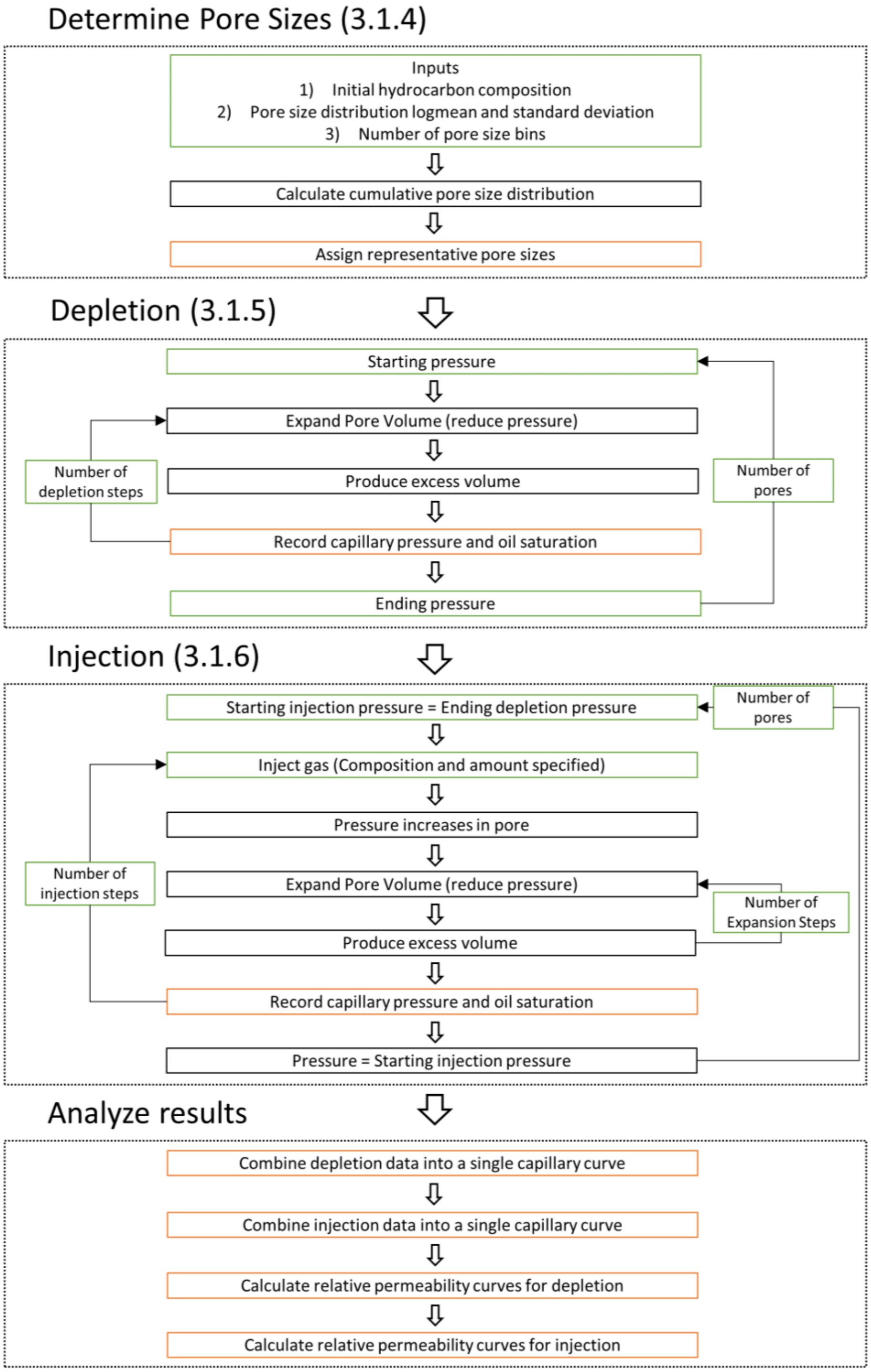

Figure 3.16: Flowchart summarizing the mechanistic model. The steps shown run sequentially from top to bottom. Inputs to the model provided by the user are shown in green. Outputs calculated during the model run are shown in orange.

3.2 Generation of Relative Permeability Curves

The experimental determination of relative permeability curves is often a time consuming and difficult process. With unconventional reservoirs the process is even more difficult due to the extremely low permeabilities often seen in shale or tight formations. As a result, there is interest in ways to compute rather than measure relative permeability curves. The process used in this work is based on the approach utilized by Stimpson and Barrufet (2017). This approach relies on integration of capillary pressure results as described by Nakornthap and Evans (1986).

3.2.1 Fitting an Equation to the Capillary Results

After a capillary curve has been generated using one of the methods described in Sections 3.1.1, 3.1.3, 3.1.5 or 3.1.6 above, an equation is fit to the capillary results. If using a pore distribution the oil saturation averaging method (method 3a in Section 3.1.5) is used to determine the combined capillary pressure curve. Stimpson (2017) evaluated a number of common capillary pressure models but found that a rational polynomial equation nearly always resulted in the best fit of the capillary results. Therefore, the rational polynomial equation of the form in Eq. 3.9 will be used in this thesis.

$$P_c(S_o^*) = \frac{a_1 + a_2 S_o^* + a_3 S_o^{*2} + a_4 S_o^{*3}}{b_1 + b_2 S_o^* + b_3 S_o^{*2}} \tag{3.9}$$

Where:

$$S_o^* = \frac{S_o - S_{o,min}}{1 - S_{o,min}} \tag{3.10}$$

S_o^* is known as the normalized oil saturation and is defined so that it has a range of zero to one as the oil saturation ranges between the minimum oil saturation and an oil saturation of one, respectively. Figure 3.17 below shows a rational polynomial fit to the capillary pressure results from the combined depletion curve in Figure 3.12.

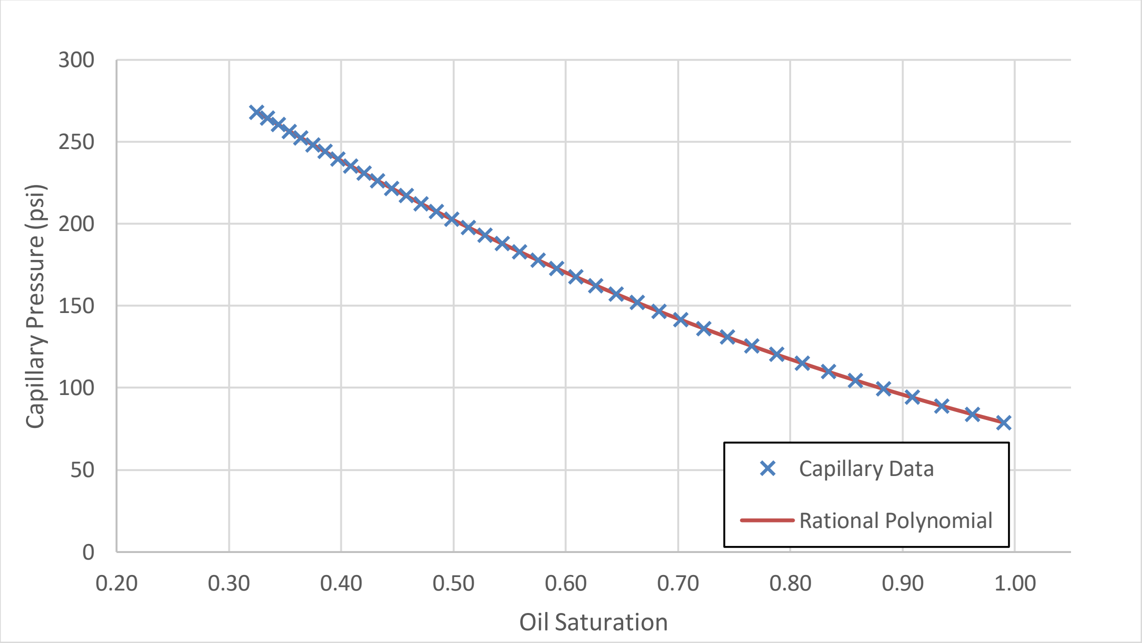

Figure 3.17: Rational polynomial equation fit to capillary results for a combined pore depletion.

The coefficients for the best fit polynomial equation (Eq. 3.9) are shown below and are fit using a sum of least squares regression technique.

Table 3.1: Coefficients for Rational Polynomial Equation Fit to Depletion Capillary Pressure Data

Coefficient	a1	a2	a3	a4	b1	b2	b3
Value	**268.0**	**2664.3**	**-2218.1**	**439.6**	**1**	**10.9**	**3.0**

3.2.2 Integration of Capillary Data to Determine Relative Permeability

Once an equation has been fit to the capillary results, the equation can be integrated to determine the relative permeability curves for oil (Eq. 3.11) and gas (Eq. 3.12) phases using equations based on a derivation from Nakornthap and Evans (1986).

$$k_{ro}(S_o^*) = (S_o^{*2})\frac{\int_0^{S_o^*}\frac{1}{P_c^2}dS_o^*}{\int_0^1\frac{1}{P_c^2}dS_o^*} \tag{3.11}$$

$$k_{rg}(S_o^*) = (1 - S_o^*)^2\frac{\int_{S_o^*}^1\frac{1}{P_c^2}dS_o^*}{\int_0^1\frac{1}{P_c^2}dS_o^*} \tag{3.12}$$

Capillary pressure from Figure 3.17 yields the following relative permeability curves.

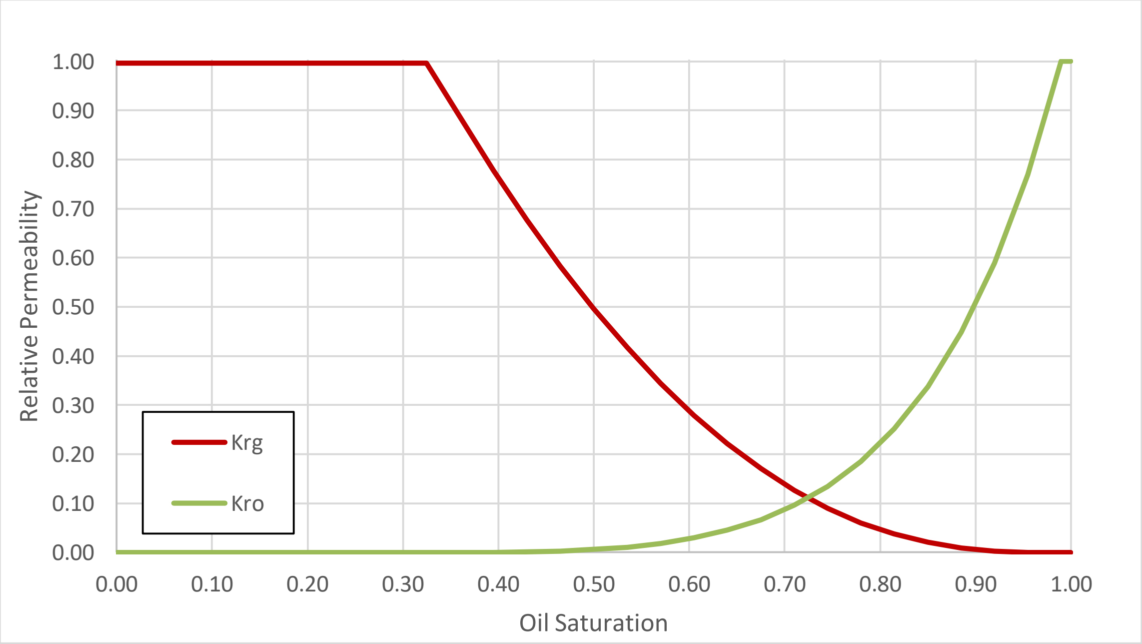

Figure 3.18: Relative permeability curves calculated from a rational polynomial equation fit to depletion capillary results.

3.2.3 Iterative Approach to Calculation of Relative Permeability Curve

When running a pore depletion (Section 3.1.1 or 3.1.5) or pore injection (Section 3.1.3 or 3.1.6) calculation, one of the production modes available is relative permeability. The shape of the relative permeability curves affects the shape of the generated capillary curve, which in turn affects the calculated relative permeability curves. This results in a circular relationship between the capillary curves and relative permeability curves. However, a convergence of results occurs when the following iterative approach is applied:

1) An initial capillary curve is generated using the constant composition production mode.
2) This capillary curve is used to generate a set of relative permeability curves.
3) A new run is performed, using the relative permeability production mode and the calculated relative permeability curves from step 2, to generate a new capillary curve. The new run uses the same pore size distribution as in the initial run in step 1.
4) This new capillary curve is then used to calculate an updated set of relative permeability curves.
5) Steps 3 and 4 are repeated until the change in capillary pressures between successive iterations fall within a specified tolerance.

Figure 3.19 below shows the capillary pressure curves from three iterations of this process performed on an Eagle Ford oil. Figure 3.20 below shows the relative permeability curves generated from the corresponding capillary pressure curves. By the third iteration of this process, the capillary curves, and therefore the generated relative permeability curves, converge to a final set of curves.

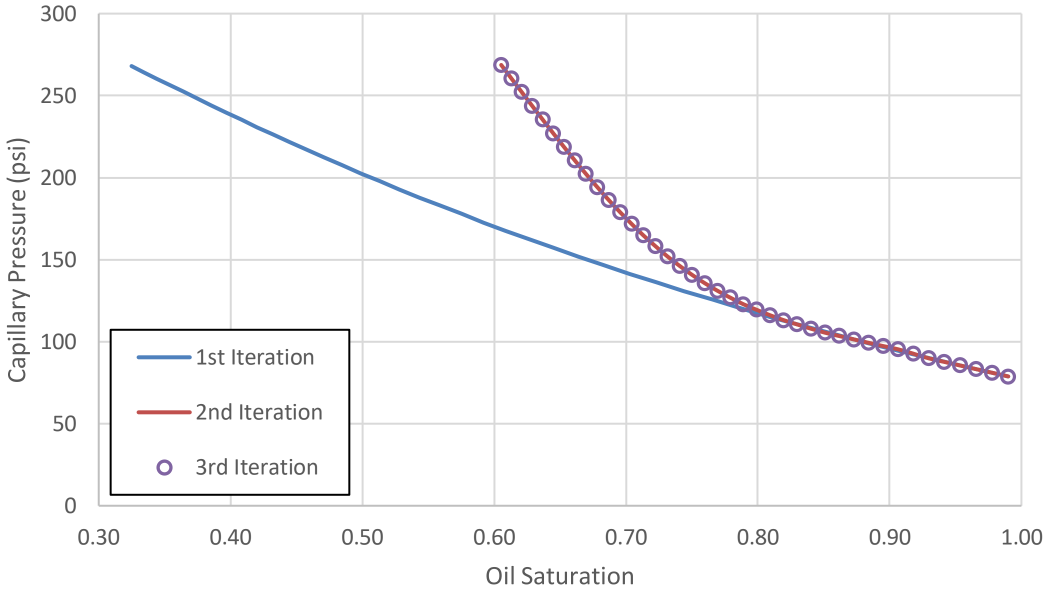

Figure 3.19: Depletion capillary pressure curves from three iterations. The first curve was generated using a constant composition production mode. The second and third curves were generated using the relative permeability production mode. The relative permeability curves were generated from the capillary results from the previous iteration.

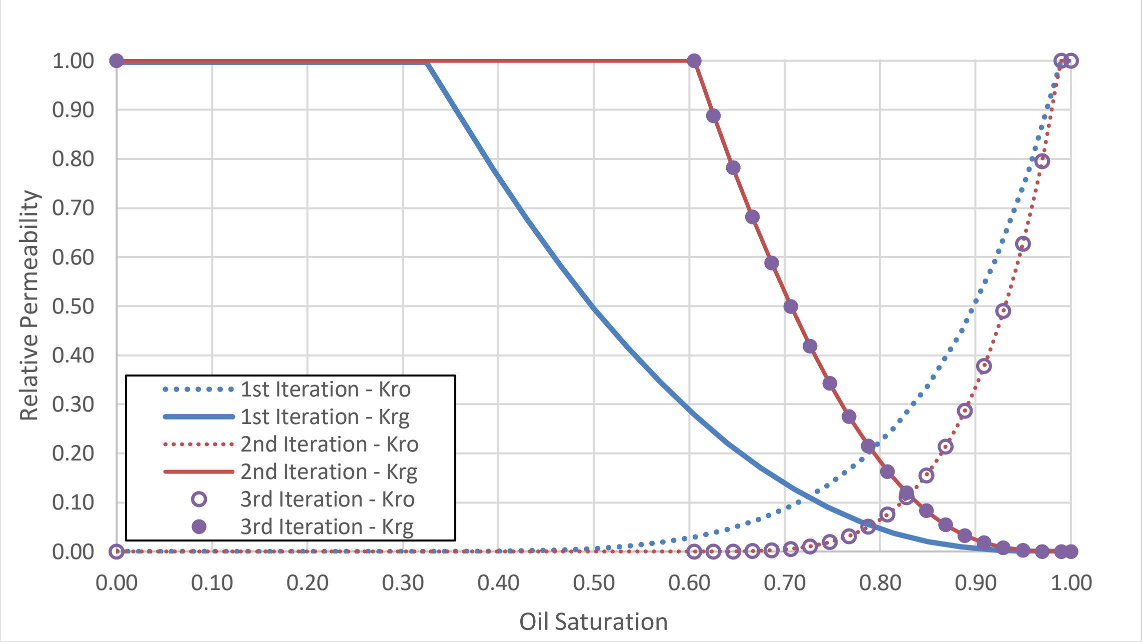

Figure 3.20: Relative permeability curves for three iterations of capillary curve calculation. The curves converge very quickly as seen by the overlap of the curves from the second and third iterations.

It is important to note that this converging behavior occurs regardless of the production mode used for the first iteration. For example, if the preferential gas mode is used for the initial iteration of the process, the relative permeability curves converge to the same final curves in Figure 3.20 above after a sufficient number of iterations.

3.3 Comparison of Calculated Relative Permeability Curves to Experimental Data

In this section, the capillary integration method described in Section 3.2 above is compared against published experimental data from Kalla et. al. (2015).

3.3.1 Description of Experimental Setup

The experimental setup used by Kalla et. al. (2015) relied on a composite core made up several core pieces held together inside a cylindrical core holder and wrapped in a sleeve to prevent fluid flow around the outside of the core. The core holder was connected to two pumps, one which pumped a gas phase and the other which pumped a liquid phase. At the start of the experiment only the gas phase was pumped through the core. Progressively more of the liquid oil phase was pumped through the core to simulate two phase flow with an increasing liquid flow rate. A digital camera was used to measure the production of the two phases at the downstream end of the core. The production rates along with the two pump pressures were used to calculate relative permeability curves. The paper describes a run performed using a fluid composed of methane and butane. The relative permeability method will be compared against the results for this fluid and experimental conditions.

3.3.2 Description of Calculation Parameters

A depletion run for a single pore size was simulated in an attempt to model the experimental setup as closely as possible in order to allow comparison of the calculated relative permeability curves with the relative permeability data presented in the paper. Where possible values and parameters from the paper were used directly. For values that were not provided a reasonable value was estimated and used for the calculation. The following parameters were used for the mechanistic model depletion run:

Pore Size – The paper does not specify any pore size data for the composite cores analyzed. As a result, a pore size was estimated using the Kozeny-Carman equation (Eq.3.13 below) based on the supplied porosity ($\Phi=0.25$) and permeability ($k=500$ md) of the core tested.

$$r = \sqrt{\frac{(8)(k)987}{\phi}} \tag{3.13}$$

The 987 is included to account for a unit conversion of permeability value.

$$1\,md = 987\,nm^2$$

The resultant pore radius used is 3974 nm.

Fluid Composition - The paper states that the fluid analyzed is a mixture of methane and n-butane but does not provide the molar fraction of each components. As a result, three molar compositions were analyzed.

Table 3.2: Total Methane / N-Butane Molar Compositions Analyzed

Fluid Number	Molar % C_1	Molar % n-C_4
1	50	50
2	40	60
3	60	40

Binary Interaction Coefficient - The paper states that for the methane/butane mixture the interfacial tension at 160°F and 1100 psig is 2 dyne/cm. A methane / n-butane binary interaction coefficient value of 0.21 was selected so that the interfacial tension is approximately 2 dyne/cm when the mixture is flashed at 160°F and 1100 psig. This coefficient was used for all three fluids analyzed. Contact angle for this mixture was not specified therefore a contact angle of 30° was assumed to indicate an oil water reservoir.

Production Mode – The capillary pressure data used to calculate the relative permeability curves was obtained by running a depletion simulation for a single pore size. The constant composition production mode was used for the depletion. This production mode was selected because the paper states that each time the liquid/gas injection ratio was modified the ratio was maintained long enough to allow the flow to reach steady state. By definition this would guarantee that the oil/gas ratio produced from the downstream end of the core would be equal to the saturation of oil and gas within the core. This type of production is equivalent to the constant composition production mode where the amounts of oil and gas produced during each depletion step is equal the saturation of oil and gas in the pore.

Depletion Pressure Range – For each fluid analyzed, a pressure range was selected such that the capillary pressure data ranges from an initial oil saturation of approximately 0.6 to a final oil saturation of approximately 0.03. This was done to match the saturation range of the data presented for the methane / n-butane mixture by Kalla et. al. (2015).

3.3.3 Results

The capillary pressure data obtained from the depletion run for each fluid was integrated using the technique in Section 3.2 and all three sets of relative permeability curves were plotted in Figure 3.21 below along with the experimental data.

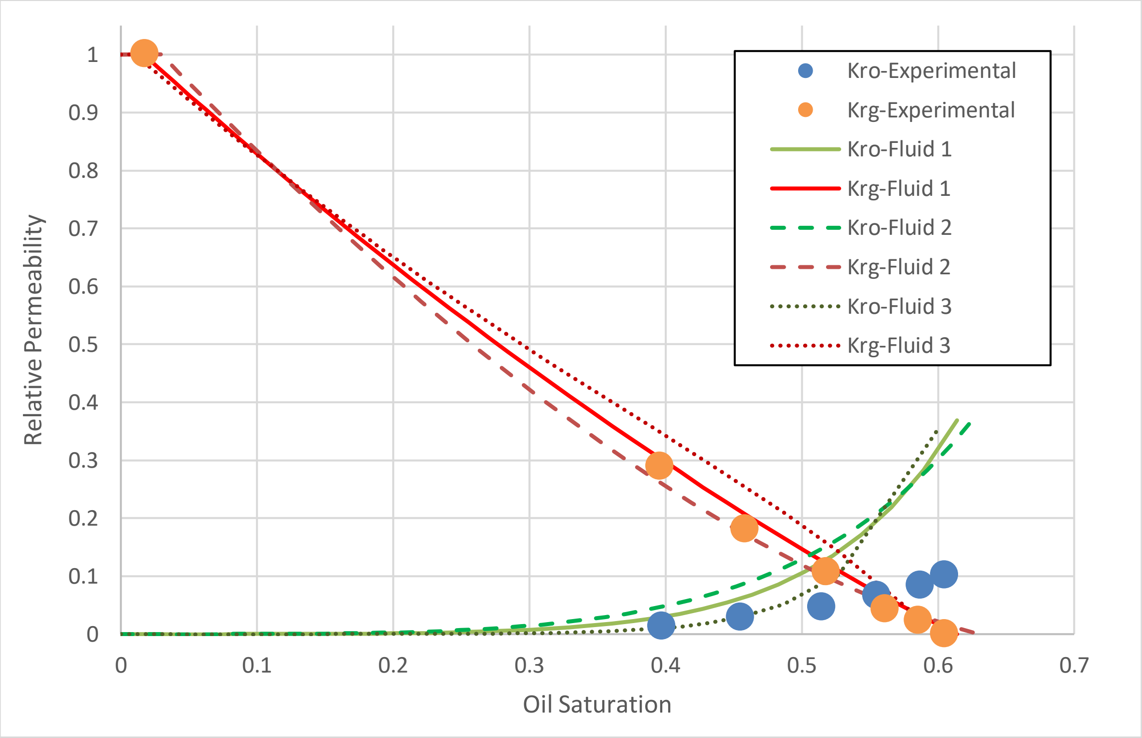

Figure 3.21: Relative permeability curves calculated for three fluids composed of varying molar amounts of methane and n-butane. The capillary data was obtained from a single pore depletion run. The plot includes experimental data for the "Model Fluid" from Figure 14 of Kalla et. al. (2015) for comparison.

The depletion calculation required a number of assumptions and estimated parameters, which precludes a direct comparison, but the calculated and experimental data show a reasonable match. The calculated results for the gas relative permeability show a closer match than those for the liquid phase.

4. DESCRIPTION OF RESERVOIR SIMULATOR

The results obtained from the mechanistic model are compared against reservoir simulation results for the equivalent run conditions. This section describes the reservoir simulator used, the simulation input parameters, the assumptions inherent in the simulator and limitations of the simulator. The compositional simulator is written in Matlab software and has capabilities to model both depletion and gas injection processes. The simulator is based on a version originally developed by Gonzalez (2016) and modified to account for confinement in the vapor liquid equilibrium calculation by Stimpson (2017). The simulator is implicit in pressure and explicit in saturation and composition (IMPESC). A complete description of the creation and validation of the simulator on which this version is based is provided by Gonzalez (2016). The following subsections will describe aspects of the simulator most pertinent to the research discussed in this thesis as well as modifications made to the simulator throughout the course of this research.

4.1 General Simulator Capabilities and Limitations

The reservoir simulator is used to model production from and injection into a hydraulically fractured reservoir with fractures on both ends of a rectangular reservoir model. The compositional simulator has the following major assumptions and limitations:

Isothermal System – The reservoir system is assumed to remain at a single temperature throughout the entirety of each run. For injection runs, the injection gas is assumed to be at the same temperature as the reservoir.

Two Phase Flow – The simulator is limited to oil and gas flow only. Water is not included in any simulations.

Instant Equilibration – Oil and gas reach thermodynamic equilibrium instantaneously in each time step.

Slight Rock Compressibility – The reservoir rock is slightly compressible and results in a reduction or increase of pore volume during depletion or injection respectively. The reduced pore volume is recalculated with each time step and an exponential pressure-volume relationship is assumed.

No Chemical Reactions or Wall Sorption – There is no accounting for adsorption/desorption effects on production.

Capillary Pressure is Optional – Simulations can be run with or without considering capillary pressure effects. Runs without capillary pressure effects use the normal Peng-Robinson equation of state with Peneloux volume translation to model phase behavior. Runs including capillary pressure effects model phase behavior as described in Section 2.1.

Two Vertical Fractures – The simulator models production from a rectangular shaped reservoir with vertical fractures on opposite ends of the model. The two vertical fractures fully penetrate the entire reservoir width and height. Either fracture can be used for either production or gas injection. All production and gas injection occurs through one or both of these fractures. The fractures are assumed to have infinite conductivity.

Small Fractures Not Explicitly Modeled – Other fractures including microfractures are not explicitly modeled. Instead, the enhanced permeability associated with the presence of these fractures is accounted for by increasing the matrix permeability above typical unstimulated values.

Permeability – The user has the capability to assign different permeability values to individual cells in the model but in this work, homogenous permeability is used. Vertical permeability is set lower than horizontal permeability for the simulations in this work.

Porosity – In this work, a uniform porosity is used for all cells in the model.

Darcy Flow – Due to the relatively low flow rates associated with production from vertical fractures it is assumed only Darcy flow occurs. Non-Darcy flow effects are not included in the analysis.

Well Model Not Incorporated – Flow through the horizontal well connected to the fractures is not included in the model. Once hydrocarbons pass through the fracture face into the fracture they are included in the production totals.

4.1.1 Description of Reservoir Model

The simulator is set up to model production from either one or two vertical fractures in an unconventional reservoir. The model assumes fully penetrating fractures and models the production from the stimulated reservoir volume as shown in Figure 4.1 below. It is assumed the two fractures are connected to separate adjacent well bores allowing simultaneous production from one well and gas injection into the other. This arrangement where the fractures of adjacent wells are offset from one another is commonly known as a “zipper fracture” configuration. Many operators attempt to create this fracture spacing in the hopes of increasing recovery by increasing contact with the reservoir (Jacobs 2014).

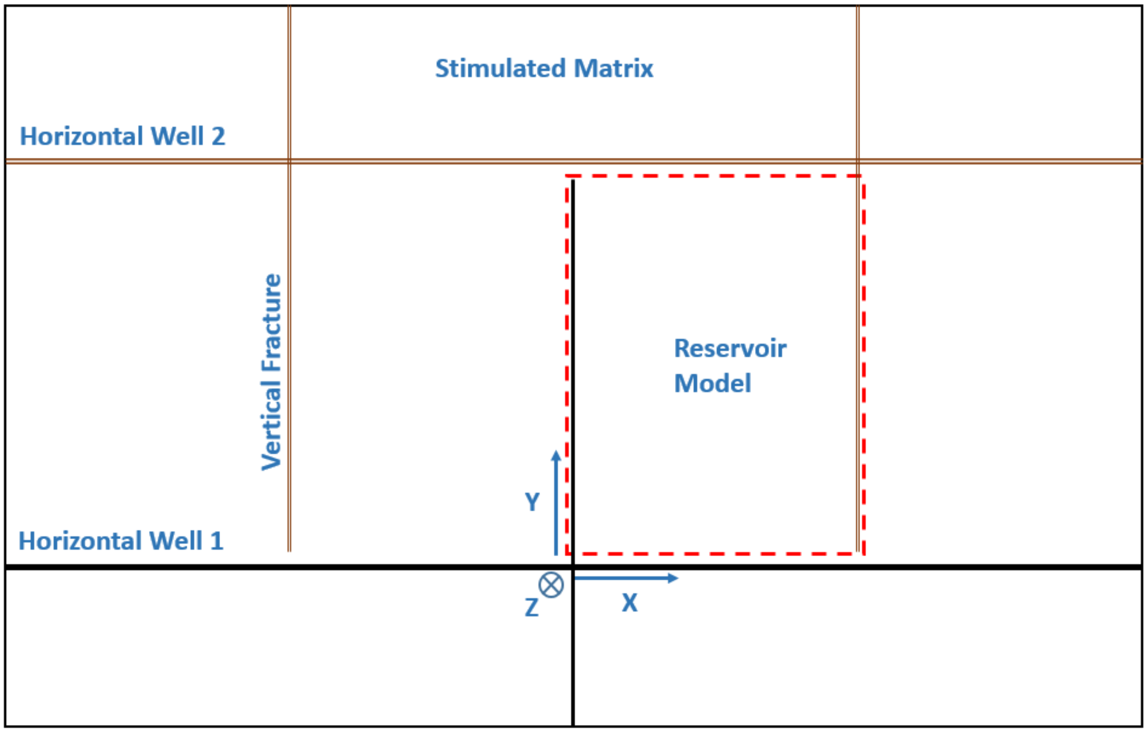

Figure 4.1: A top down view of a stimulated reservoir with three vertical fractures connected to two separate horizontal wells is shown. The reservoir simulation model includes two fractures and stimulated reservoir matrix between the two fractures (shown as a dashed red box).

The reservoir model assumes a highly idealized configuration and models only a single portion of a pattern that repeats along the length of the wellbore. Figure 4.2 below shows a sample reservoir model during depletion.

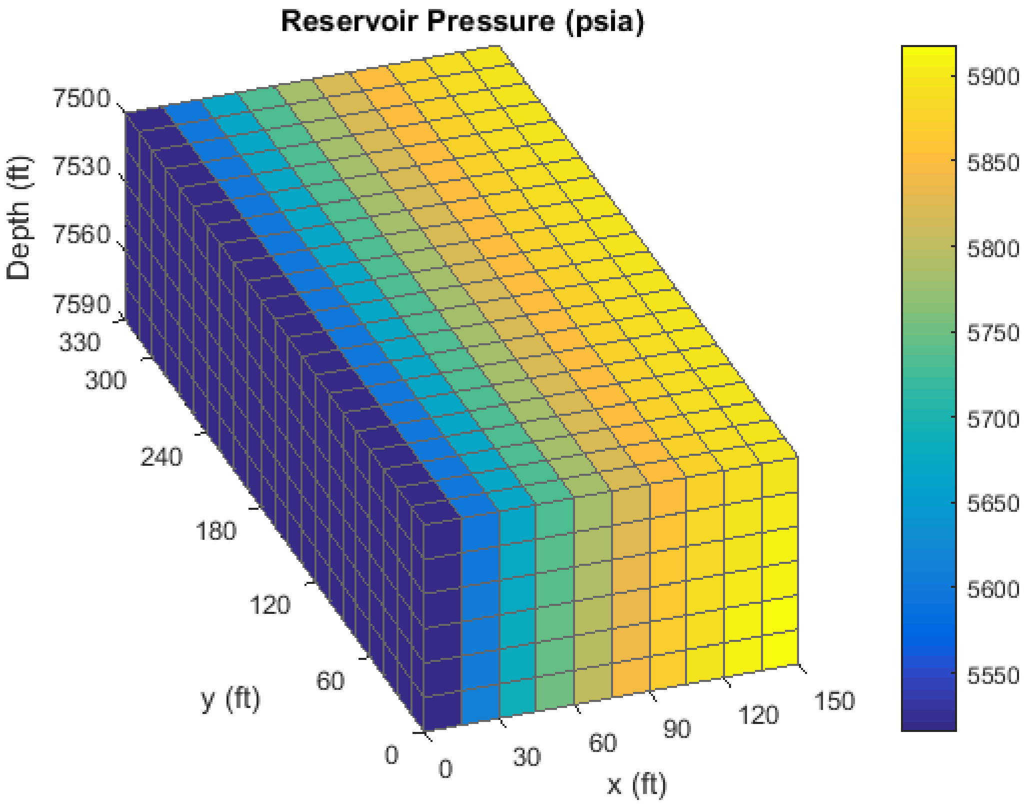

Figure 4.2: Sample reservoir model during a depletion run with the pressures of each cell shown. Hydrocarbons are produced from the fracture face (not shown) located at the left side of the model (x=0 ft) resulting in the lower pressures observed. The other fracture located at x=150 ft is not used in this simulation run. This model contains a total of 1320 cells.

It is assumed that the fractures have infinite conductivity throughout the length of the simulation run.

4.2 Assignment of Pore Size

To account for the effects of confinement during reservoir simulations each cell within the reservoir model is assigned a pore size at the start of each simulation run. The pore size is used to determine the capillary pressure which is used as part of the vapor liquid equilibrium calculation as described in Section 2.1. The simulator has three options for pore size assignment:

Single Size - The entire reservoir model can be assigned a single pore size.

Lognormal Distribution - Pore sizes can be assigned based on a log-normal distribution in which the log mean and standard deviation of the distribution are specified as inputs.

Custom Distribution - Pore size vs. cumulative pore volume data can be input in the simulator and used to determine the corresponding distribution. This type of data could typically be obtained from a Mercury Injection Capillary Pressure (MICP) laboratory analysis on a rock sample (Australian 2014). This option can also be used to analyze a hypothetical pore size distribution.

4.2.1 Lognormal Distribution Pore Size Assignment

In this research, the lognormal option is used almost exclusively. For the lognormal distribution option, values for the log mean and standard deviation for the distribution are supplied as inputs for the simulation run. Based on these inputs, pore sizes are assigned. The process of selection pore sizes is similar to the process described for the mechanistic model in Section 3.1.4. The process is summarized as follows with an emphasis on any differences from the mechanistic model:

1) The simulator calculates the cumulative probability density function for a lognormal distribution with the specified inputs up to the maximum pore size. The distribution is normalized with respect to the maximum pore size.
2) The fraction of total pore volume represented by each cell is calculated. This is determined by dividing each cell's pore volume by the total pore volume of the

reservoir model. The cells in the model may have different pore volumes depending on the cell dimensions and porosities assigned. This step differs slightly from the mechanistic model because pore volumes must account for cell dimensions and porosity which may not necessarily be uniform in the reservoir model.

In the specific case where uniform cell dimensions and porosities are specified, each cell in the model will represent the same fraction of pore volume. This is the case for the simulation runs detailed in Section 5 below and also for the sample reservoir model in Figure 4.2 above.

3) Cells are selected at random and based on the fraction of pore volume represented by the cell, a pore size is chosen based on the cumulative density profile calculated in Step 1. Based on the range of pore sizes corresponding to the cell, a midpoint value is chosen and used to determine a pore diameter for the cell.

Once all the cells have been assigned, the pore sizes in the reservoir volume will be representative of the log-normal distribution specified.

4.2.2 Illustrative Example for Log Normal Distribution

A simple example of the assignment procedure for the simulator is shown below. This example is for a reservoir with 9 equally sized cells. The parameters for the distribution are a log mean value of 3 nm, standard deviation of 0.6, and maximum pore size of 100 nm. Figure 4.3 shows the probability density function corresponding to this distribution.

Figure 4.4 shows the cumulative distribution function before and after it has been normalized to the maximum pore size. As long as the maximum pore size is sufficiently large the normalized distribution will match the lognormal distribution closely. This normalization step is required to ensure that the total cumulative probability is accounted for.

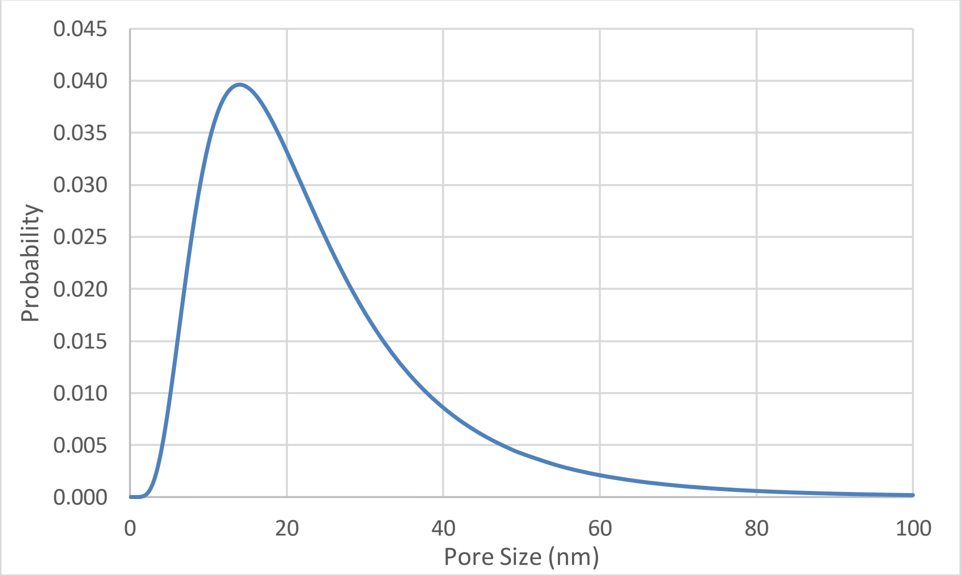

Figure 4.3: The probability density function for a lognormal distribution with log mean 3.0 nm, which corresponds to a mean pore size of 20.1 nm, and a standard deviation of 0.6 nm.

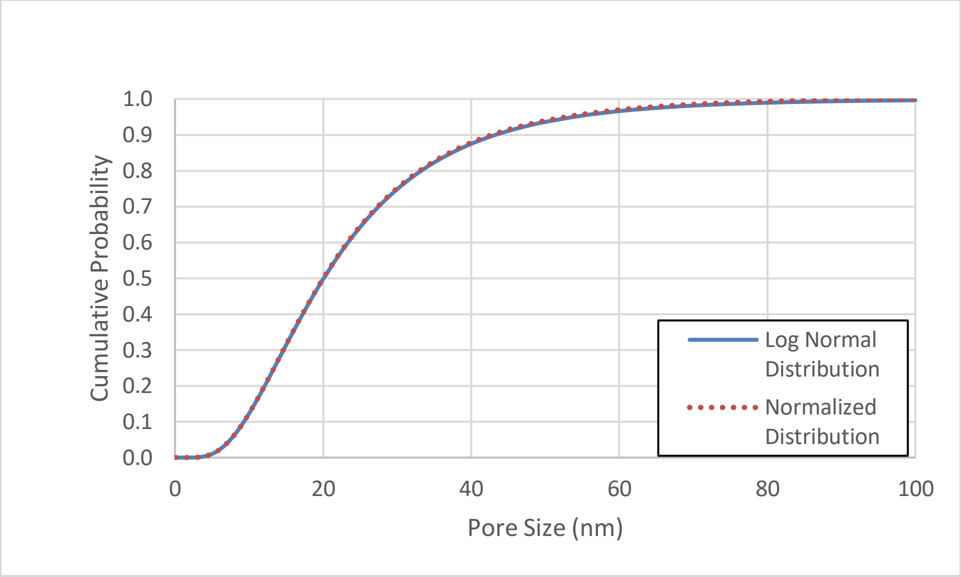

Figure 4.4: The cumulative density function is normalized based on the specified maximum pore size. In this instance, the normalization process has little effect on the resultant curve. The effect of the normalization process becomes more pronounced as the maximum pore size is reduced.

Figure 4.5 shows the process of dividing the cumulative distribution up into segments, selecting a midpoint value and selecting the corresponding pore size for each segment. In this simple example, the cell dimensions are uniform and the porosity of each cell is equal. As a result, the pore volume of each cell is equal and therefore the segments are equally spaced.

If the pore volumes are not uniform, the size of the segment will correspond to the fraction of total pore volume represented by the cell. An example of this case is presented in Section 4.2.3.

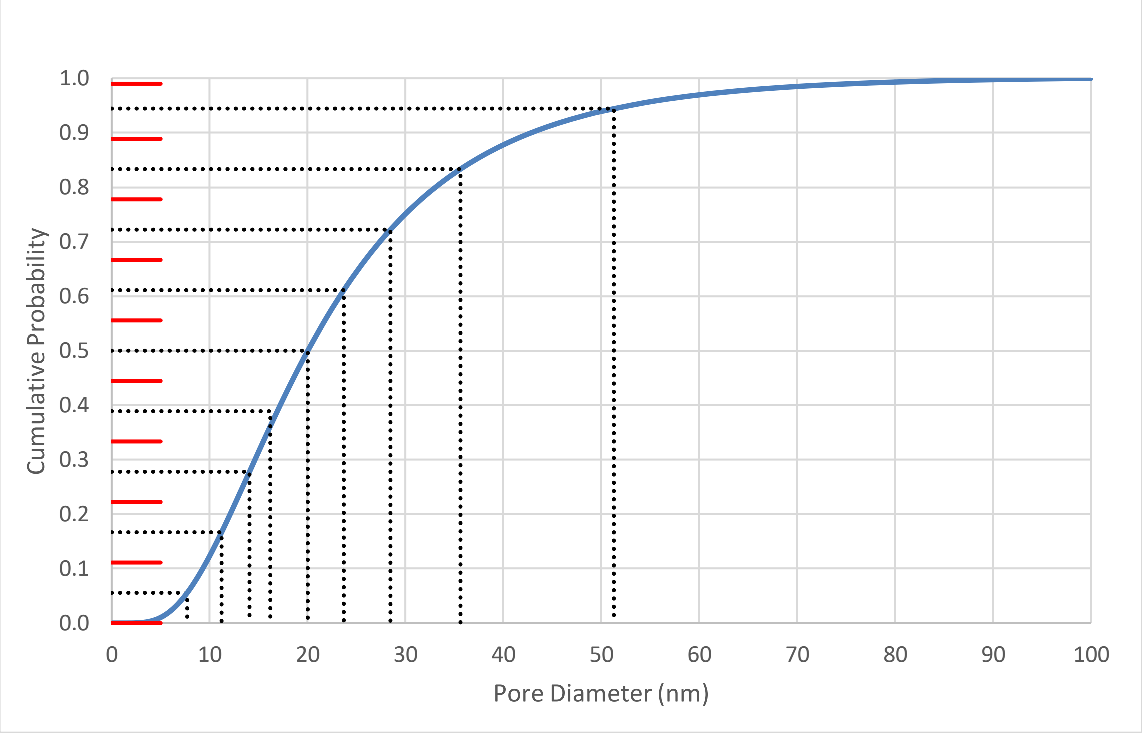

Figure 4.5: Pore sizes for individual cells in the reservoir model are selected by dividing the cumulative probability distribution into 9 equally sized segments and selecting the pore size corresponding to the midpoint of each segment.

The sequence in which pore sizes are assigned is randomized therefore the pore sizes are randomly distributed throughout the reservoir. Figure 4.6 shows the pore size assignment for a reservoir model containing only nine cells. However, if the entire process is repeated using the same input parameters, the same pore sizes may be distributed in a different location each time.

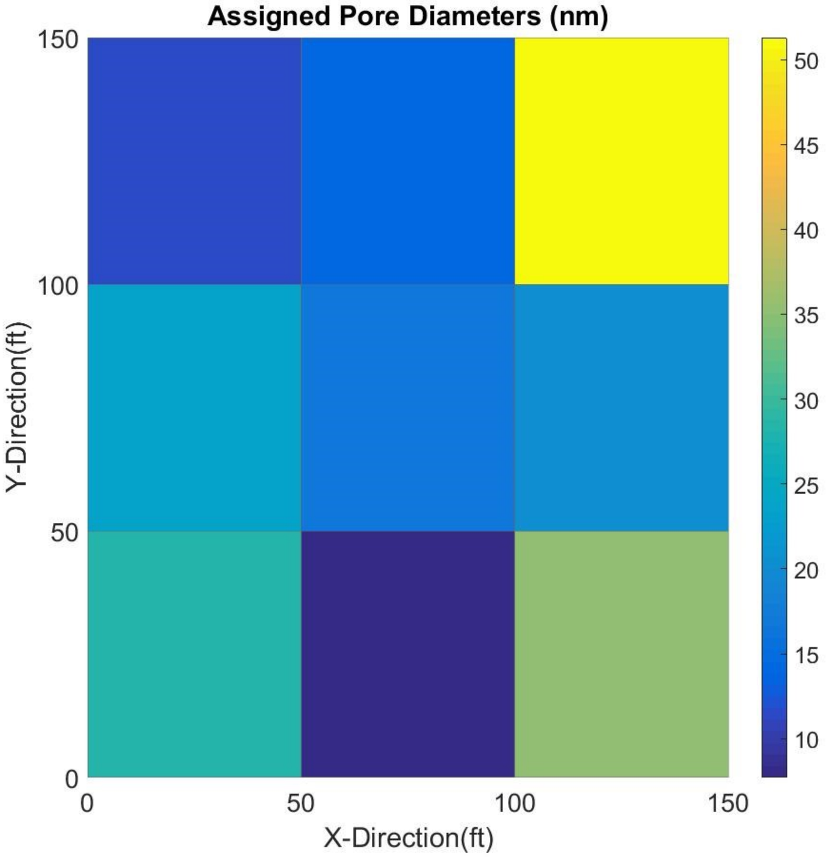

Figure 4.6: The pore size assignment for each cell represents a lognormal distribution. The cells are spatially distributed randomly throughout the reservoir volume.

The same process can be applied to any number of cells. Figure 4.7 below shows the pore diameters assigned when the same pore size distribution is applied to a larger reservoir model containing 1320 cells (10 x 22 x 6).

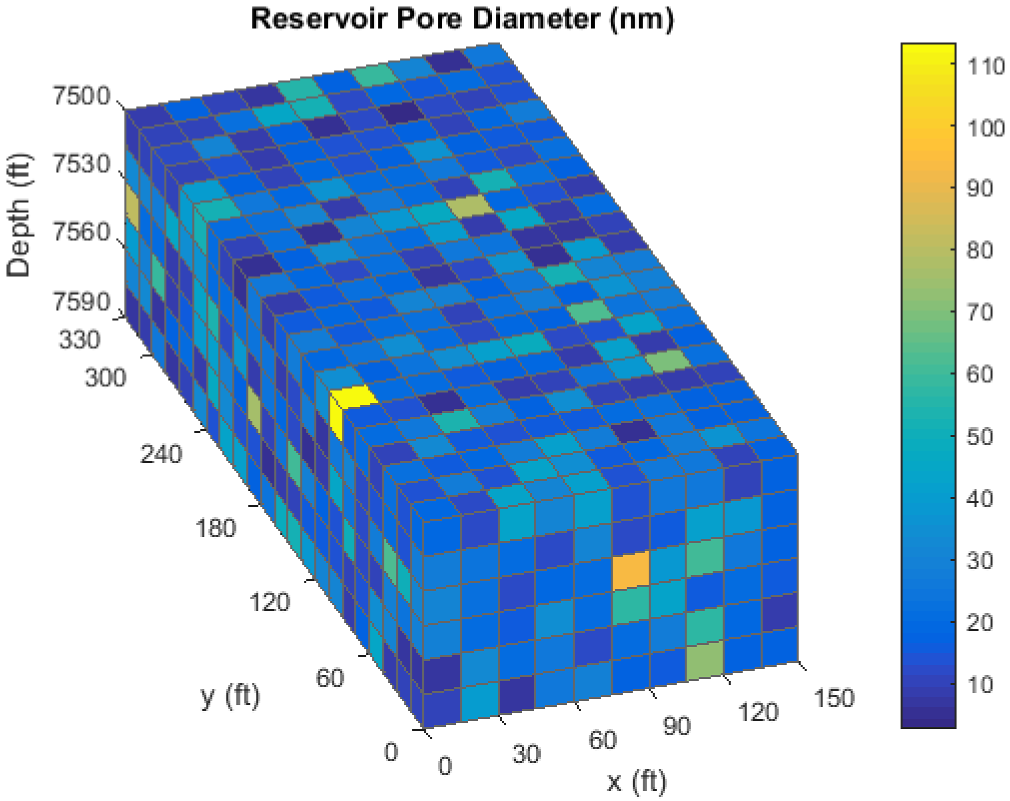

Figure 4.7: Reservoir model pore diameter assignments for a lognormal distribution with log mean 3 nm and a standard deviation of 0.6 nm. Vertical fractures through which hydrocarbons are produced are located at x=0 ft and x=150 ft.

This reservoir model is representative of the reservoir models used in the analyses in Section 5. Since the same pore size distribution and reservoir dimensions are used in Section 5, the same pore sizes in Figure 4.7 above will appear in the Section 5 reservoir models. However, the location in the reservoir of the individual pore sizes will change for each simulation run.

4.2.3 Pore Size Assignment from Experimental Data

In addition to a single pore size or a lognormal pore size distribution, the simulator also has the capability of assigning pore sizes based on experimental data. The data is provided in the form of an input excel file which contains cumulative pore volume as a function of pore size. Data of this form would usually be obtained from a Mercury Injection Capillary Pressure Analysis performed by a commercial testing lab. Once the data is uploaded, the simulator follows the same steps listed in Section 4.2.1 with the following modifications:

- The uploaded data forms the cumulative density profile for the sample therefore there is no need for the simulator to calculate this profile. Additionally, there is no need to normalize the data.
- Since the uploaded data is composed of discrete data points, any values falling between the given data points are determined using linear interpolation.

To illustrate the process a sample distribution was created, loaded into the simulator and used to assign pore size values. In this example, geometric spacing was used for the X and Y axes so that there are multiple different cell dimensions in the model. Figure 4.8 below shows the sample distribution along with the pore sizes that were fit to the distribution by the simulator. The irregular spacing of the assigned pore sizes is partially due to large differences in the volume of the cells in the reservoir model.

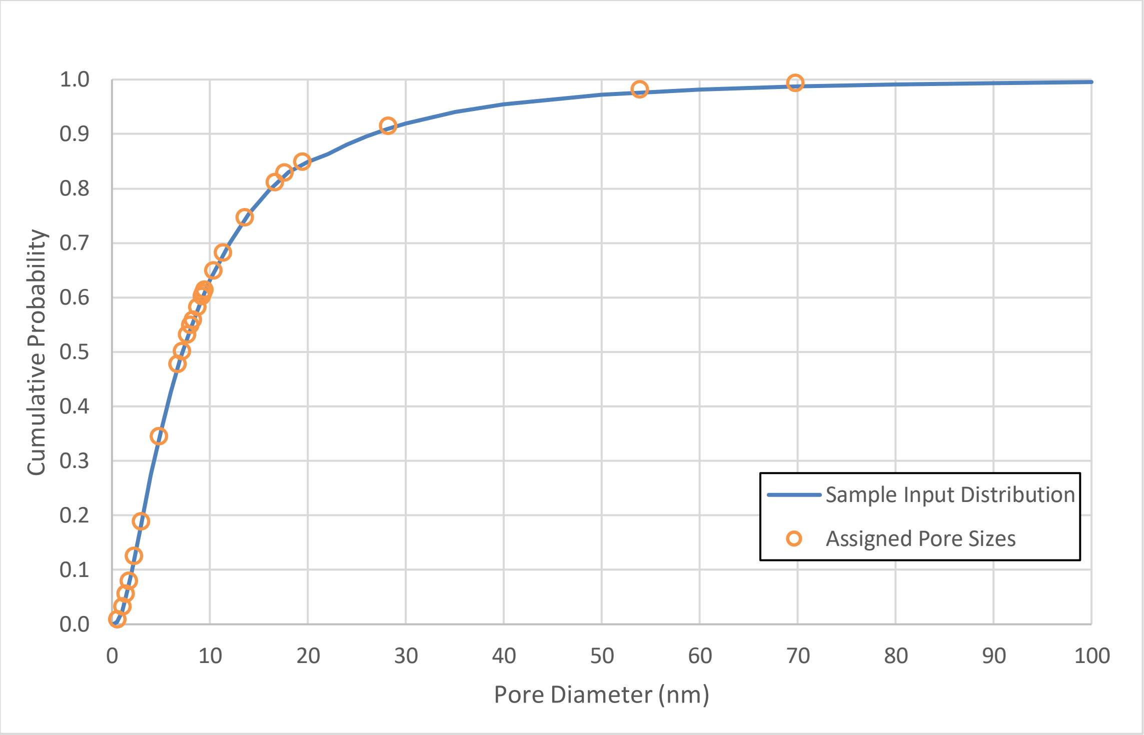

Figure 4.8: Pore sizes for individual cells in the reservoir model created from a sample distribution loaded into the simulator.

Figure 4.9 below shows how the pore sizes are distributed in a 5x5x1 non-uniform grid for the reservoir model.

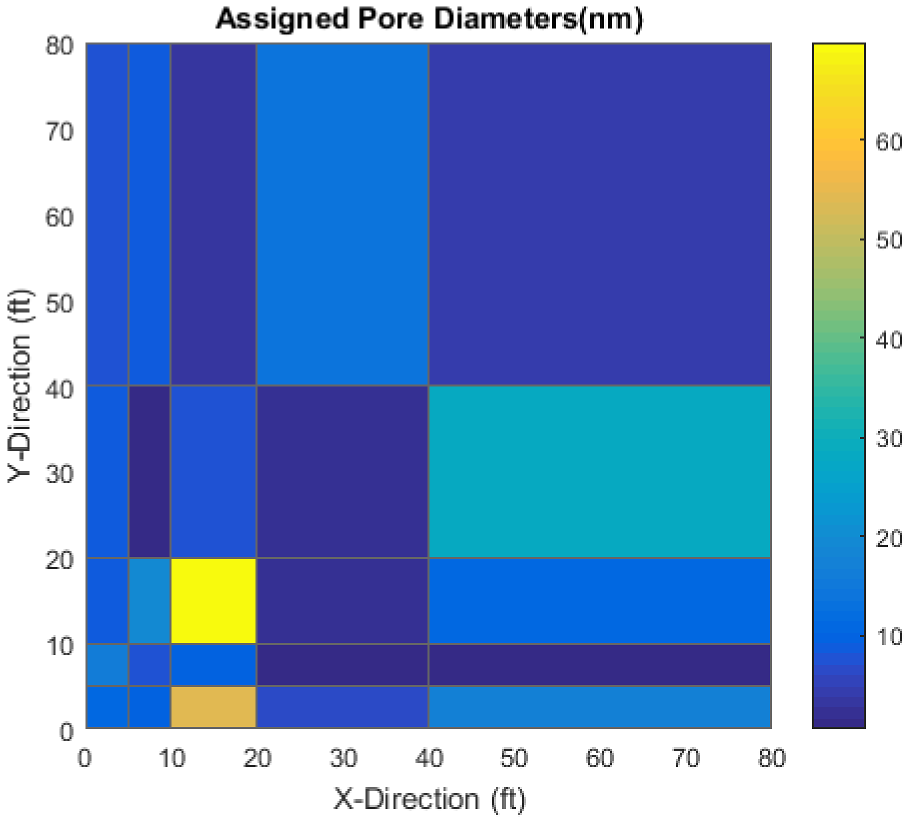

Figure 4.9: Pore size assignments for cells in the reservoir model from the sample distribution.

The pore sizes selected are a function of the cumulative pore size probability specified in the input file and a function of the pore volume of each cell. If the same distribution were used with difference cell sizes the pore sizes selected would be modified accordingly.

5. MECHANISTIC MODEL RESULTS AND COMPARISON

This chapter summarizes the results of a series of runs performed and also summarizes conclusions drawn from these runs. Two different fluid compositions are evaluated in this comparison. One fluid is a black oil, the other is a volatile oil.

5.1 Validation of Mechanistic Model

To ensure that the mechanistic process for generating capillary pressure curves described in Section 2 is working correctly, the generated results are compared against a reservoir simulation run under equivalent conditions. The parameters for this run are selected to be as equivalent as possible for the two methods. The reservoir simulator used for the comparison is described in Section 4.

5.1.1 Description of Validation Run Parameters

Fluid Model – A characterized Eagle Ford oil is used in the comparison runs. The fluid parameters are described in detail in Appendix A. The run begins at a pressure of 2200 psia which exceeds the saturation pressure of all pore sizes so that all pores are initially fully oil saturated.

Pore Size Distribution – A lognormal pore size distribution with a log mean value of 3.0 nm (mean of 20.1 nm) and standard deviation of 0.6 nm is used for the runs. The mechanistic model uses 11 pores to represent the distribution. The reservoir model has 22 cells and therefore 22 pore sizes to represent the distribution. Figure 5.1 below compares the pore diameters between the two models and the lognormal distribution.

Although different pore sizes are selected for each model, the same distribution is maintained.

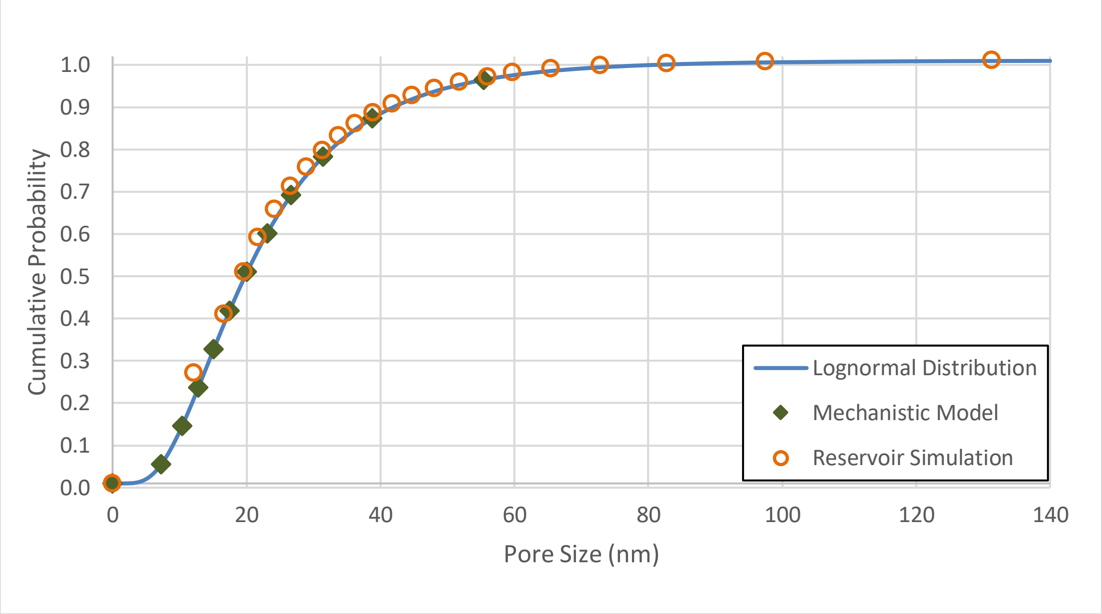

Figure 5.1: Pore sizes selected for a mechanistic model, reservoir simulation model and lognormal distribution with log mean of 3 nm and a standard deviation of 0.6 nm.

<u>Relative Permeability Curves</u> – The same relative permeability curves are used in the mechanistic model and the reservoir simulation. Two sets of curves are used during each run, one set for the initial depletion and a second set for the pore injection and secondary depletion portions of the run, both are shown in Figure 5.2 below. The relative permeability curves used are generated using the integration procedure detailed in Section 3.2.

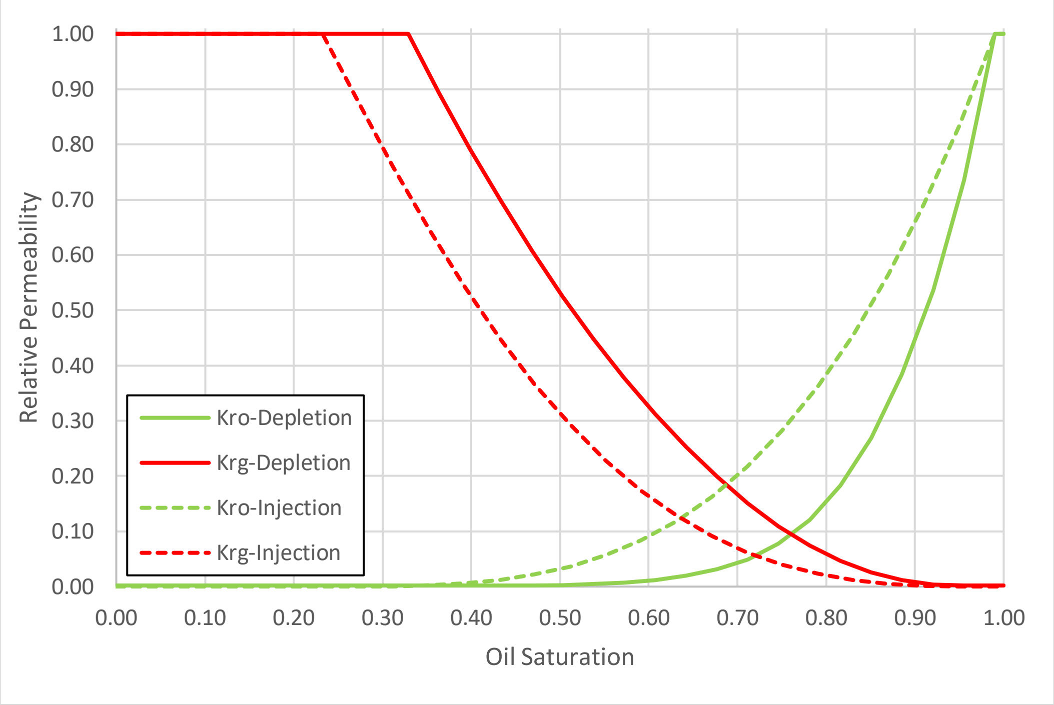

Figure 5.2: Calculated relative permeability curves for the depletion and injection portions of a reservoir simulation run. The secondary depletion portion of the run uses the same curves used for injection.

Permeability – A value of 0.2 mD is assigned to each cell and horizontal isotropy is assumed. A vertical permeability of 0.02 mD is assigned to each cell. This permeability is higher than what would be typically seen in a shale reservoir matrix, however, it is assumed the stimulation process increases the permeability of the matrix due to opening of micro fractures that are not explicitly modeled.

Porosity – A porosity of 0.08 is assigned to each cell in the model. The porosity of a cell is not related to the pore size assigned to the cell.

Reservoir Model – The reservoir model for the reservoir simulation is only 22 cells in size. The model is one cell tall, one cell deep and 22 cells wide. This shape allows direct comparison between the simulation model and the mechanistic model, which is necessary for the validation process. In this configuration, the fracture in the model is in direct contact with every cell in the model. Therefore, hydrocarbons are produced directly from and injection gas is injected into each cell directly which replicates the way the mechanistic model functions. Each cell in the simulation model is 15ft x 15ft x 15ft, however, the results from the simulation model and the mechanistic model are compared on a molar basis therefore the specific cell size does not impact the comparison. Figure 5.3 below shows the reservoir model and the pore diameters assigned to each cell.

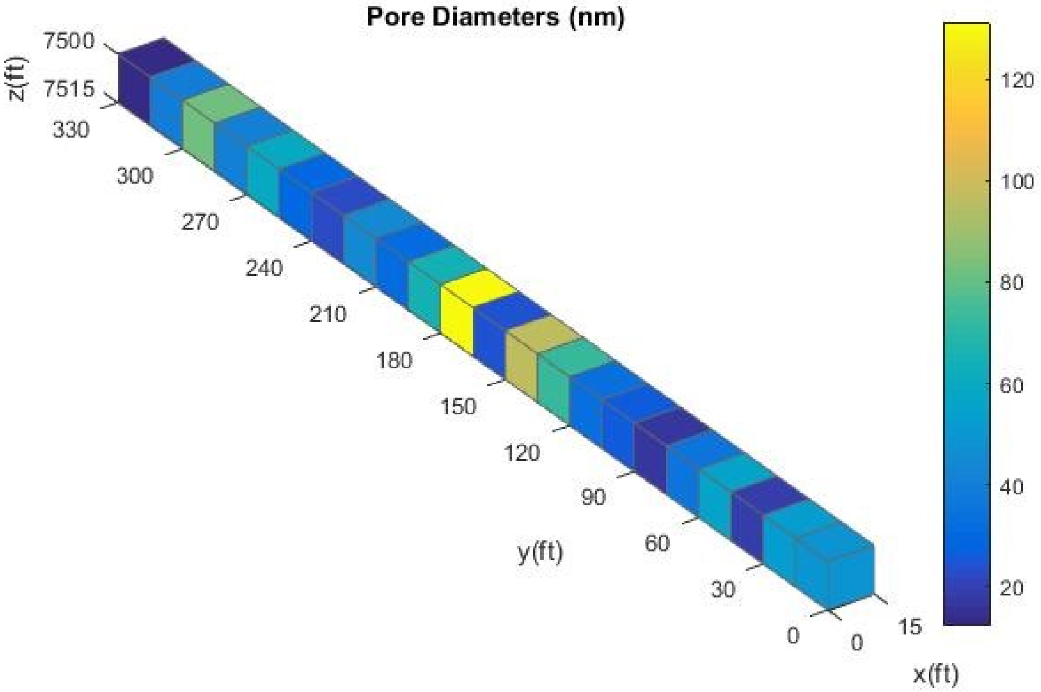

Figure 5.3: Reservoir model for the simulation validation run with assigned pore diameters. The fracture is located at x=0 ft and is in direct contact with all cells in the reservoir model.

<u>Depletion and Injection Sequence</u> – The simulation run starts at a pressure of 2200 psia. The reservoir is depleted down to a pressure of 1500 psia. Pure CO_2 is then injected into

the reservoir, the number of moles injected is set to 20% of the initial moles in place. After the injection is completed, the reservoir is then depleted down to 1500 psia again. The injection and depletion sequence is repeated two additional times with the same number of moles injected each time. The same sequence is used in both the mechanistic model run and the reservoir simulations.

5.1.2 Comparison of Mechanistic Model and Simulation Run Results

To compare the two models, the molar recoveries of each component, excluding the injection gas, are calculated and displayed below in Table 5.1. For the injection gas, CO_2, the recoveries are summarized in Table 5.2. The storage, equal to one minus the recovery, is also included in the table for convenience. For each component in the fluid, recoveries are calculated for the initial depletion (Eq. 5.1), the injection portion of the run (Eq. 5.2) and the total molar recovery (Eq. 5.3) which combines the depletion and injection parts of the run. The injection portion of the run includes the multiple injection and depletion steps following the initial depletion step.

$$Depletion\ Recovery\ of\ Component\ i = \frac{n_{i,prod.\ init.\ dep.}}{n_{i,init.}} \tag{5.1}$$

$$Injection\ Recovery\ of\ Component\ i = \frac{n_{i,prod.\ 2nd\ dep.}}{n_{i,init.} - n_{i,prod.\ init.\ dep.} + n_{i,inj}} \tag{5.2}$$

$$Total\ Recovery\ of\ Component\ i = \frac{n_{i,prod.\ init.\ dep.} + n_{i,prod.\ 2nd\ dep.}}{n_{i,init.} + n_{i,inj}} \tag{5.3}$$

The recovery formulas in Eq. 5.2 and Eq. 5.3 include the amount of injection gas moles added. If the injection gas does not contain a certain component (*i*) the amount injected is set to zero in the formula.

Table 5.1: Molar Recoveries for Mechanistic Model and Reservoir Simulation for Validation Run

Component	C1	C2	C3	N2	Pseudo 1	Pseudo 2	Pseudo 3	Pseudo 4	Total (exclude CO2)
	Initial Depletion Recovery (%)								
Reservoir Simulation	20.6	17.2	15.6	23.5	14.1	13.0	12.7	12.7	16.5
Mechanistic Model	19.5	16.4	14.9	22.3	13.6	12.6	12.3	12.3	15.8
Difference	-1.1	-0.8	-0.7	-1.3	-0.6	-0.5	-0.4	-0.4	-0.7
	Injection Recovery (%)								
Reservoir Simulation	55.9	49.1	44.8	60.7	40.1	35.1	32.9	32.7	44.8
Mechanistic Model	56.0	49.0	44.6	60.8	39.7	34.7	32.5	32.3	44.7
Difference	0.1	-0.1	-0.2	0.1	-0.3	-0.4	-0.4	-0.4	-0.1
	Total Recovery (%)								
Reservoir Simulation	65.0	57.8	53.4	69.9	48.6	43.6	41.4	41.2	53.9
Mechanistic Model	64.6	57.3	52.8	69.5	47.9	42.9	40.8	40.6	53.4
Difference	-0.4	-0.5	-0.6	-0.4	-0.6	-0.6	-0.6	-0.6	-0.5

Table 5.2: Molar Recovery and Storage of CO_2 for Validation Run

	Recovery (%)	Storage (%)
	Initial Depletion	
Reservoir Simulation	17.8	82.2
Mechanistic Model	16.9	83.1
Difference	-0.9	0.9
	Injection	
Reservoir Simulation	37.0	63.0
Mechanistic Model	36.7	63.3
Difference	-0.3	0.3
	Total	
Reservoir Simulation	37.2	62.8
Mechanistic Model	36.9	63.1
Difference	-0.3	0.3

The recoveries from the reservoir simulation and mechanistic model are within one and a half percent of each other for all components including CO_2, which is the injection gas for this run. This agreement confirms that the mechanistic model and reservoir simulation are modeling the same behavior in this idealized setup.

The capillary pressure results for the mechanistic and simulation models are also compared. For the mechanistic model, the capillary pressure curve is generated as described in Section 3.1.5 for the depletion curve and Section 3.1.6 for the injection capillary pressure curve. For the reservoir simulation, the capillary curve is generated by calculating the pore volume weighted, average capillary pressure for the reservoir at the end of each simulation time step. These values are then plotted as a function of average oil saturation in the reservoir model.

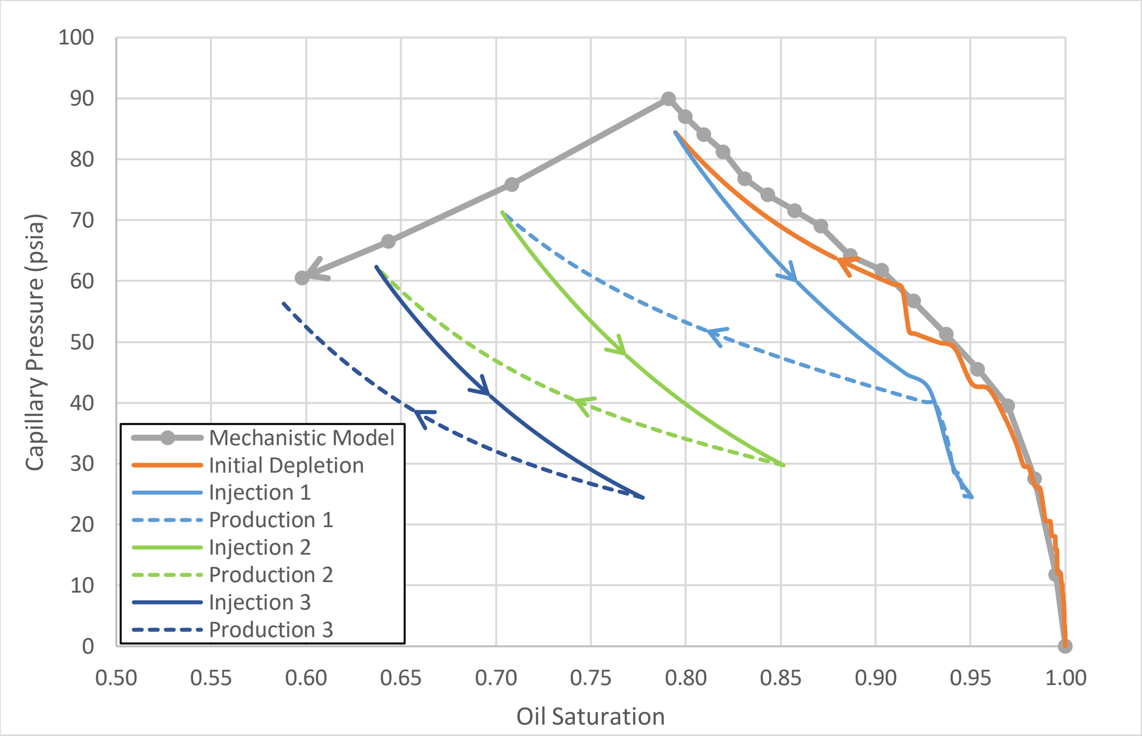

Figure 5.4: Comparison of capillary pressure results from the mechanistic model (heavy gray line) and the reservoir simulation results (all other lines). The simulation model runs through an initial depletion, followed by three injection cycles. Following each injection, additional hydrocarbon production occurs. The arrows indicate the time progression of each run.

The capillary curves from the initial depletion portion of each run look similar and match closely. For the reservoir simulation, the curve is not as smooth as the curve from the mechanistic model. The roughness in the curve occurs due the fact that the reservoir model only contains 22 cells. Each bump in the curve corresponds to a cell transitioning from single phase oil, which has zero capillary pressure, to a two phase oil and gas mixture, which results in a non-zero capillary pressure. This discrete change in the capillary pressure of a single cell causes the sharp increases seen in the average reservoir capillary pressure. As the number of cells in the reservoir model is increased, the curve becomes smoother because each individual cell represents a smaller fraction of the total pore volume and therefore has a smaller impact on the average capillary pressure calculation.

For the injection portion of the run, the curves from the two models look much more dissimilar. The mechanistic model calculates the capillary pressures at the end of each injection cycle while the simulation results show the average reservoir capillary pressure during each simulation time step throughout the injection cycle.

For the reservoir simulation, as CO_2 is injected, the average saturation increases while at the same time average capillary pressure decreases as seen in the solid lines in Figure 5.4. After the CO_2 injection stops and production begins again, shown by the dashed lines, the oil saturation decreases again and there is a corresponding increase in capillary pressure which results in the saw-tooth pattern seen in Figure 5.4. The three sets of these curves correspond to the three injection cycles. The mechanistic model shows the capillary pressure after the end of each injection and production cycle and therefore matches the left endpoints of the reservoir simulation curves in Figure 5.4.

5.2 Application of Mechanistic Model to a Larger Reservoir Volume for a Black Oil

After verifying that the mechanistic model and reservoir simulation are capable of producing similar results for an idealized reservoir shape, the mechanistic model is compared to results for a larger, more realistic reservoir volume. Many of the run parameters described in Section 5.1.1 above are used for the simulation runs in this section. The run parameters that are the same include 1) the fluid model, 2) the pore size distribution and 3) the relative permeability curves. The pore size distribution is the same but since the larger model contains more cells, the actual pore sizes assigned to each cell are different. For reference, Figure 4.7 shows a sample pore size assignment for the pore size distribution used. The depletion and injection parameters are similar to those described in Section 5.1.1 except only one injection sequence is used. The entire run consists of an initial depletion, an injection and a secondary depletion. Additionally, the amount of CO_2 injected is increased to 30 lbmol CO_2 per 100 lbmol of hydrocarbons initially in place.

The reservoir model is the only run parameter that is significantly different from that described in Section 5.1.1. The reservoir model used for simulation is larger and is described in detail in Section 4.1.1. In the larger reservoir model, only a portion of the cells are in contact with either of the two vertical fractures located on opposite ends of the model. This means that unlike the validation model in Section 5.1, the specific fracture used for the depletion and injection portion of the run can impact capillary pressure in the reservoir and the compositions and amounts of hydrocarbons produced.

5.2.1 Single Fracture Run for Black Oil

For this simulation run, the same fracture is used for the initial depletion, the CO_2 injection, and the second depletion portions of the run. Figure 5.5 shows select pressure plots throughout the course of the run. The fracture used for depletion and injection is located on the left side of the plots.

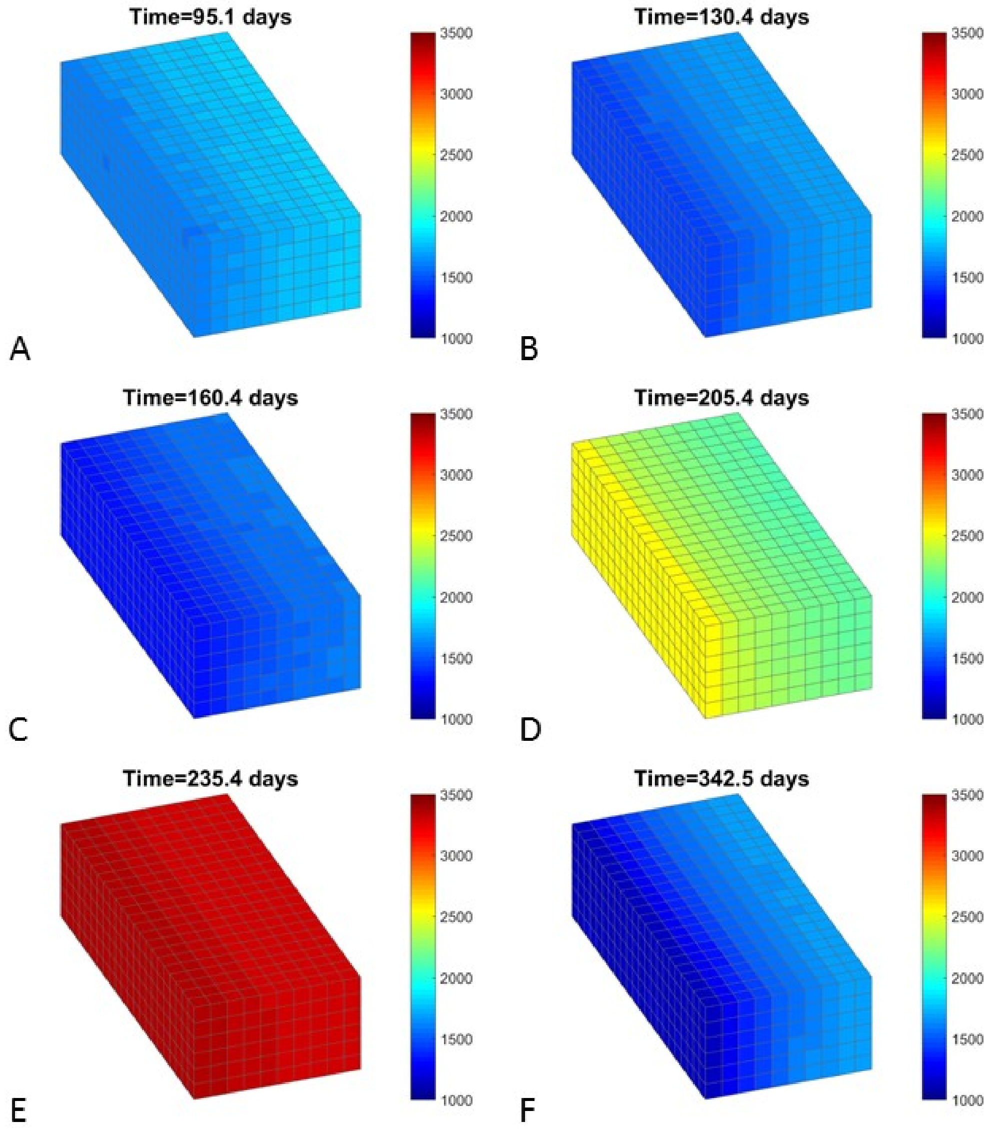

Figure 5.5: Pressure plots for a single fracture simulation run in psia. Plots A and B are during the initial depletion. Plot C is at the end of the initial depletion. Plot D is during injection. Plot E is the start of the 2nd depletion and plot F is the end of the 2nd depletion (end of entire simulation).

As would be expected, the pressure in the reservoir decreases during the initial and secondary depletion portions of the run and increases during the injection. A pressure gradient is seen along the depth of the reservoir with the smallest (or largest) pressures in the cells closest to the fracture during depletion (or injection). Figure 5.6 shows the molar composition of CO_2, which is the injection gas, during the run.

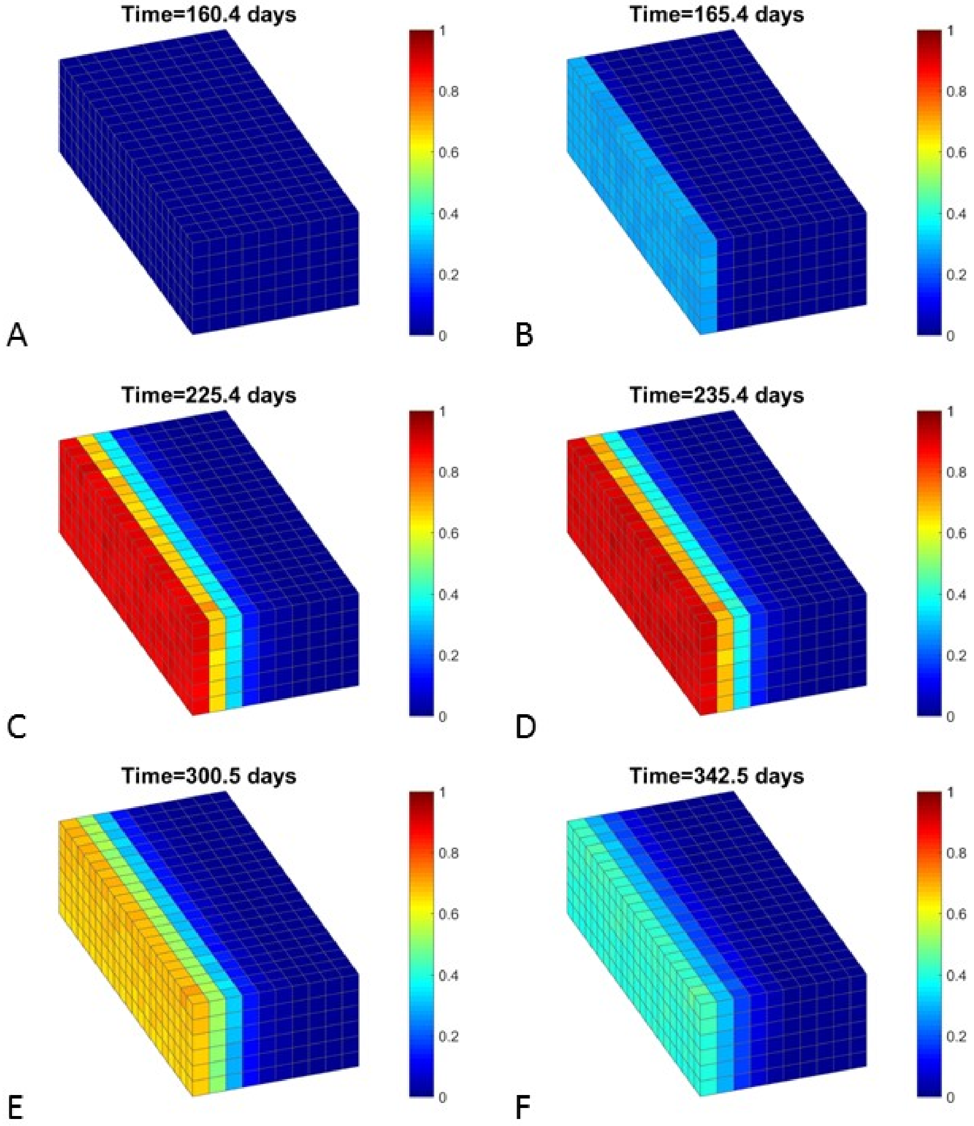

Figure 5.6: Carbon dioxide composition plots for a single fracture simulation run. Plot A is at the start of CO_2 injection, plots B and C are during injection and plot D is at the end of injection. Plot E is during the secondary depletion and plot F is the end of the secondary depletion (end of entire simulation).

The composition plot shows the CO_2 moving into the reservoir during the injection phase and being produced back during the secondary depletion. Figure 5.7 shows the capillary pressure inside the individual cells during the run while Figure 5.8 shows the oil saturations for the corresponding cells at the same times.

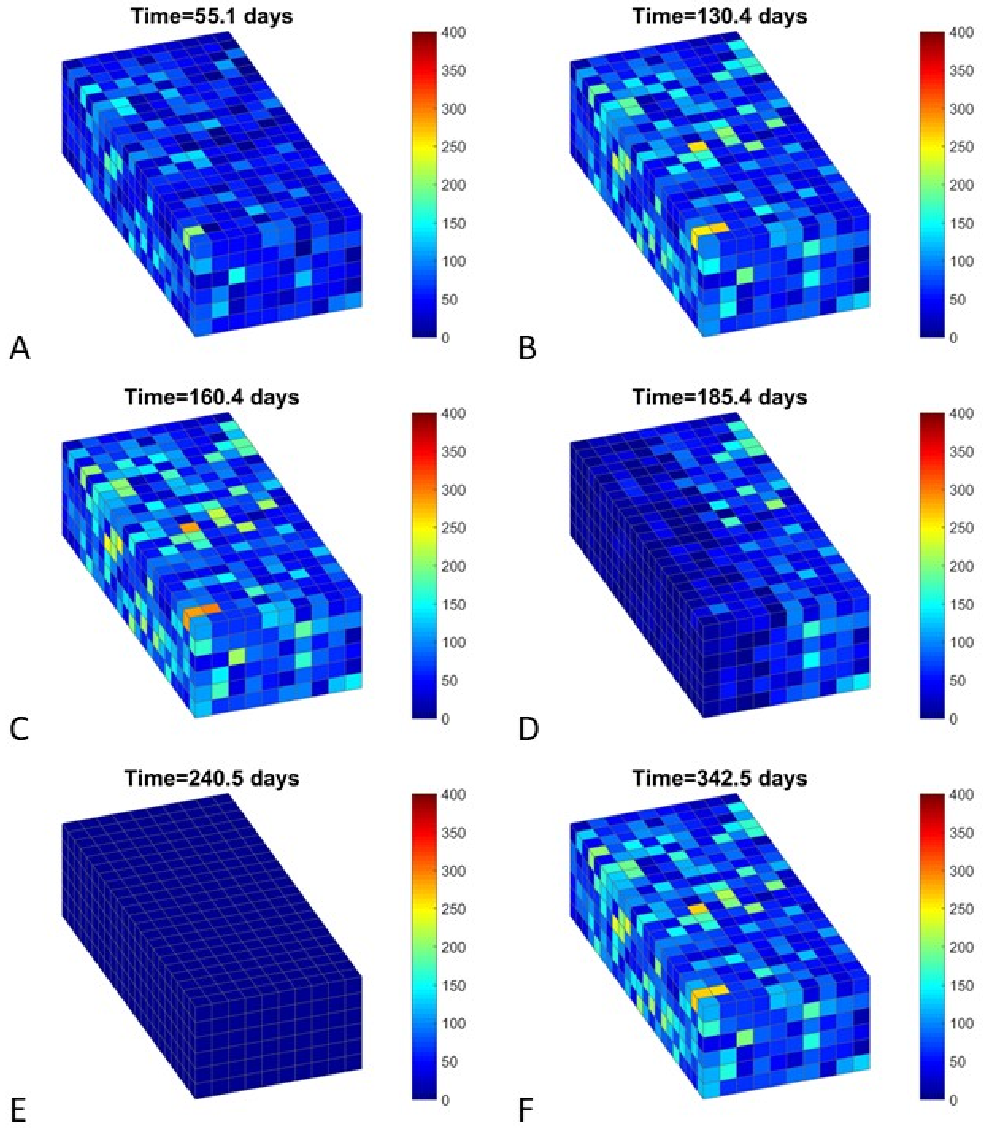

Figure 5.7: Capillary pressure plots for a single fracture simulation run in psi. Plots A and B are during the initial depletion. Plot C is at the start of injection and plot D is during the injection. Plot E is at the start of the secondary depletion and plot F is the end of the secondary depletion.

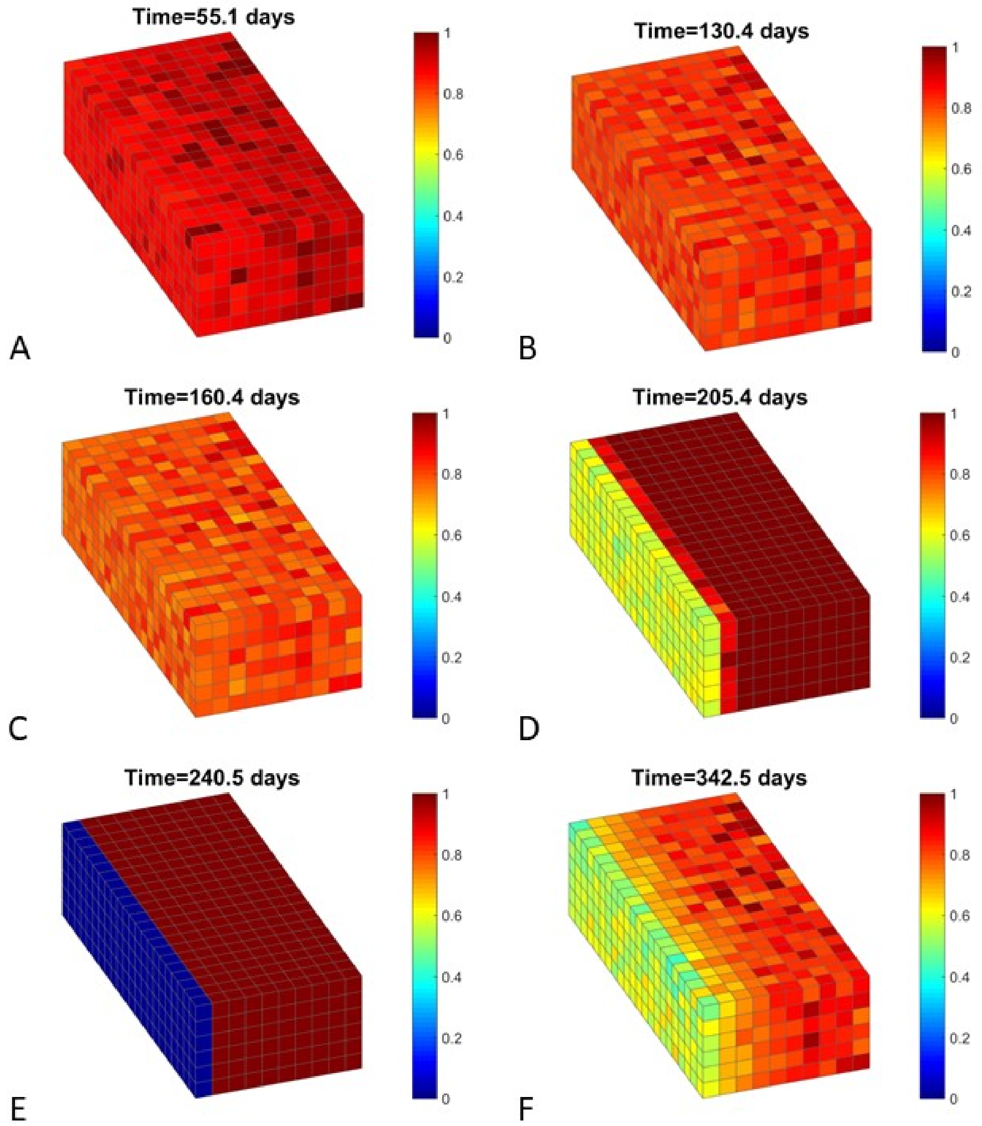
Time=55.1 days

Time=130.4 days

Time=160.4 days

Time=205.4 days

Time=240.5 days

Time=342.5 days

Figure 5.8: Oil saturation plots for a single fracture simulation run. Plots A and B are during the initial depletion. Plot C is at the start of injection and plot D is during the injection. Plot E is at the start of the secondary depletion and plot F is the end of the secondary depletion.

Table 5.3 below summarizes the maximum and minimum cell values for each of the properties shown in the figures above at the end of each portion of the run (initial depletion, injection, and secondary depletion).

Table 5.3 Maximum and Minimum Cell Property Values for Single Fracture Black Oil Run

	Time (days)	So (max)	So (min)	Po (max)	Po (min)	Pcap (max)	Pcap (min)	Z_{CO2} (max)	Z_{CO2} (min)
End of Initial Depletion	160.4	0.99	0.69	1605.8	1324.1	346.2	14.8	0.01	0.01
End of Injection	235.4	1.00	0.0	3356.9	3268.9	0.0	0.0	0.93	0.01
End of 2nd Depletion	342.5	1.00	0.43	1687.2	1137.1	308.7	0.0	0.45	0.01

For the Eagle Ford oil composition and starting pressure, the reservoir is initially 100% oil. During the initial depletion, the reservoir enters two phase flow. As stated above, the injection gas used for this simulation run is CO_2 which is favorable for enhanced oil recovery because it is highly miscible with liquid hydrocarbons. This miscibility combined with the increase in reservoir pressure due to injection causes the reservoir to become single phase liquid again. The only exceptions are the rows of cells adjacent to the fracture. These cells have such a high molar concentration of CO_2 that they become single phase vapor. During the secondary depletion, a portion of the injected CO_2 is produced and the reservoir pressure decreases again. This causes the reservoir to re-enter two phase production.

It is noted that when observing the pressures and compositions of the cells (Figure 5.5 and Figure 5.6 respectively) both properties vary considerably along the depth of the reservoir (x-axis) but show little variation with respect to the height (z-axis) or width (y-axis) of the reservoir. This occurs because a homogenous permeability is used in the simulation and therefore distance from the fracture face is the primary factor affecting the pressure and composition gradients.

In contrast, the capillary pressures (Figure 5.7) and oil saturations (Figure 5.8) of the cells show much more variability along the width and height of the reservoir. There can be considerable difference between two adjacent cells that are the same distance from the fracture face. This occurs because the oil saturation and capillary pressure are strongly dependent on pore size. As described in Section 4.2, pore sizes for individual cells are selected to be representative of the pore size distribution but they are randomly located in the reservoir model. Figure 4.7 above shows a sample pore size assignment for the individual cells representing the lognormal pore size distribution used in this simulation run. All else being equal, the smallest pore sizes will tend to have the largest capillary pressure and highest oil saturations. However, capillary pressure and oil saturation are also dependent on the pressure and molar composition within each cell. Since these quantities vary with distance from the fracture face, the capillary pressure and saturation also vary with distance from the fracture face.

5.2.2 Two Fracture Run for Black Oil

In this second run, the simulation is repeated using two fractures instead of a single one. All run parameters are held constant, the only difference is that the production from the initial depletion and secondary depletion use one fracture while the CO_2 is injected through a separate second fracture located on the opposite side of the reservoir.

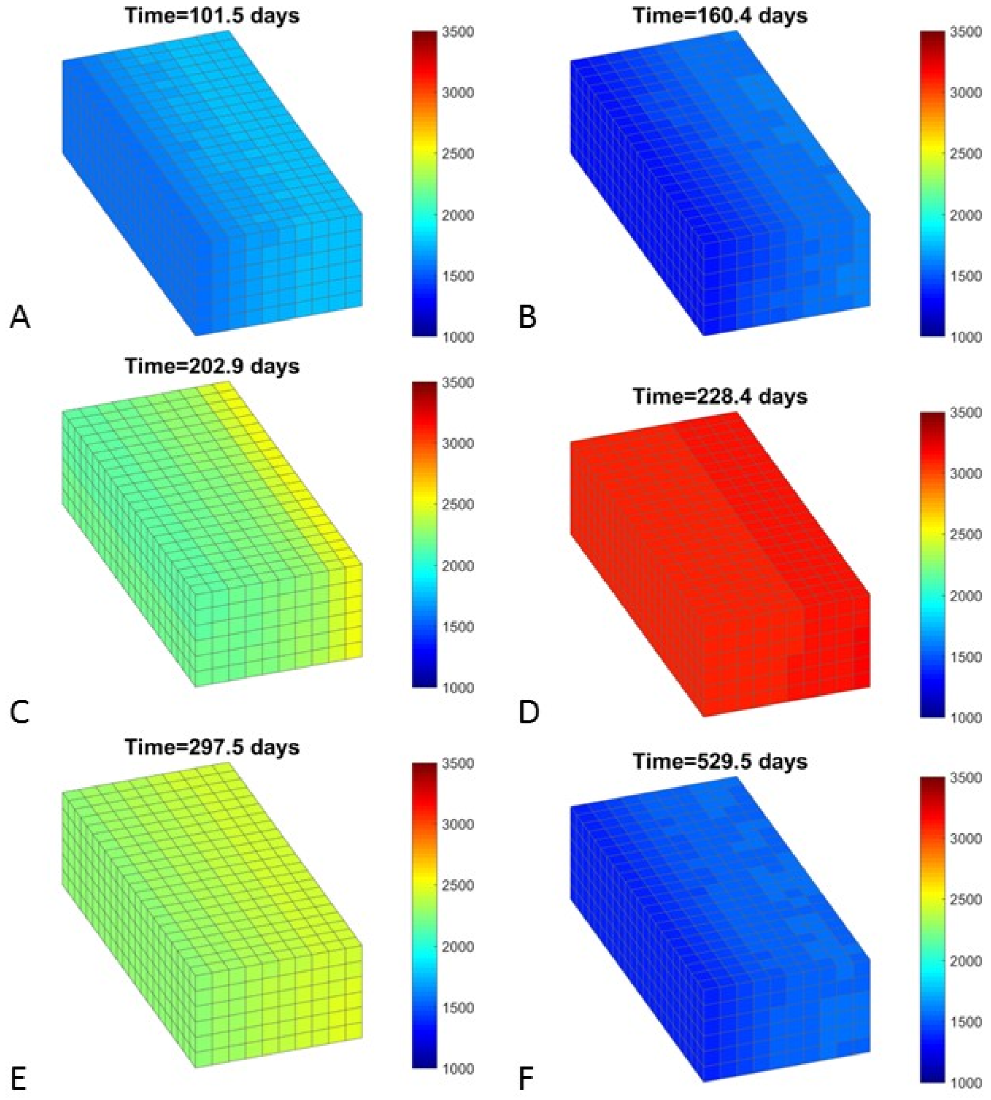

Figure 5.9: Pressure plots for a two fracture simulation run in psia. Plot A is during the initial depletion. Plot B is at the end of the initial depletion. Plot C is during the injection and plot D is at the end of injection. Plot E is during the secondary depletion and plot F is the end of the secondary depletion (end of entire simulation).

A fracture located on the left side of the reservoir is used for both the initial and secondary depletion, resulting in the reduced pressures in the cells on the left side of the reservoir seen in plots A, B, E and F in Figure 5.9. Carbon dioxide is injected through a fracture located on the right side of the reservoir causing increased pressures seen in the cells located on the right side of plot C in Figure 5.9.

Figure 5.10 below shows the CO_2 molar composition in the cells during the simulation run.

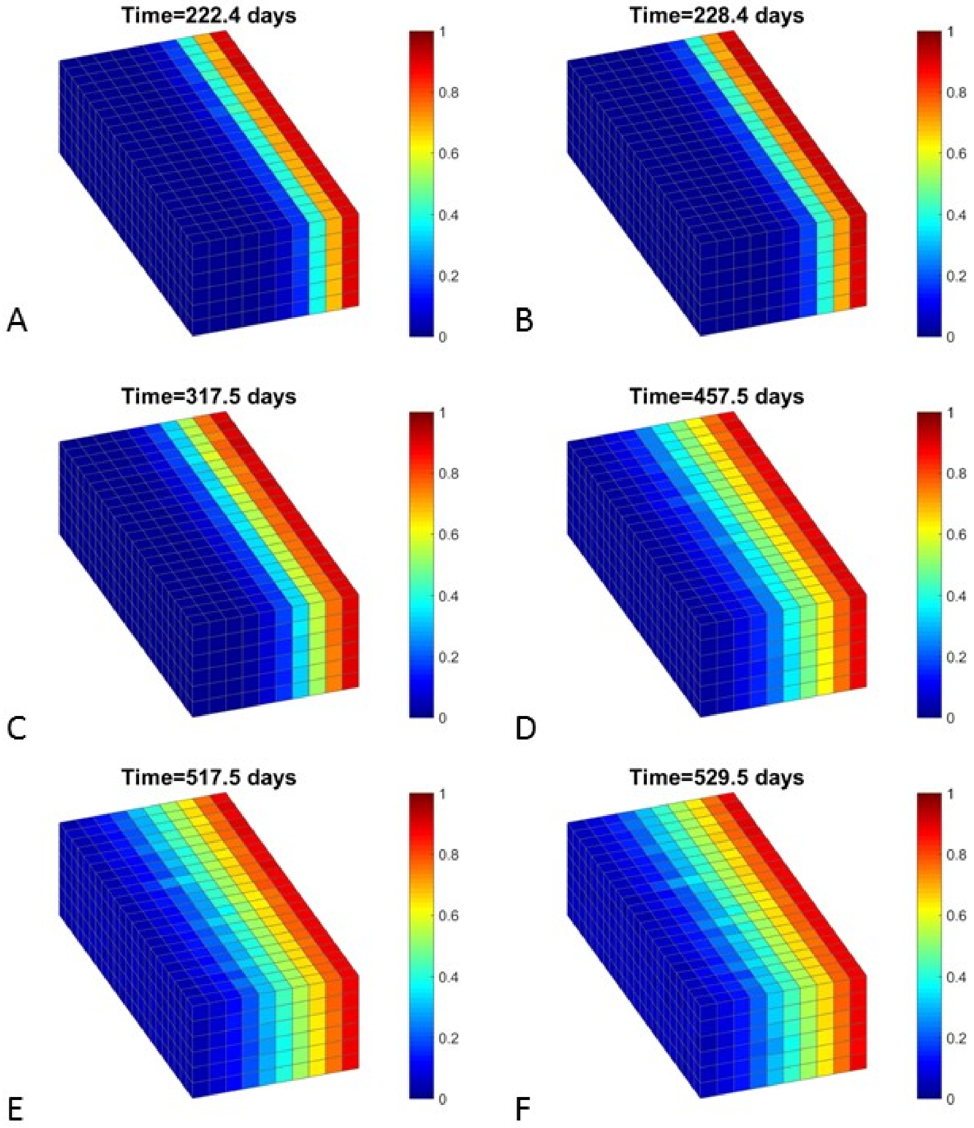

Figure 5.10: Carbon dioxide composition plots for a two fracture simulation run. Plot A is during CO_2 injection and plot B is at the end of injection. Plots C, D and E are during the secondary depletion. Plot F is the end of the secondary depletion (end of entire simulation).

During the injection portion of the simulation run, CO_2 forced into the reservoir through a fracture on the right side of the figure as seen in plots A and B. The CO_2 only penetrates to a limited extent. However, during the secondary depletion, the CO_2 is drawn deeper into the reservoir as seen in plots D through F in Figure 5.10.

Figure 5.11 shows the capillary pressure plots at select points during the simulation while Figure 5.12 shows the oil saturation at the corresponding times.

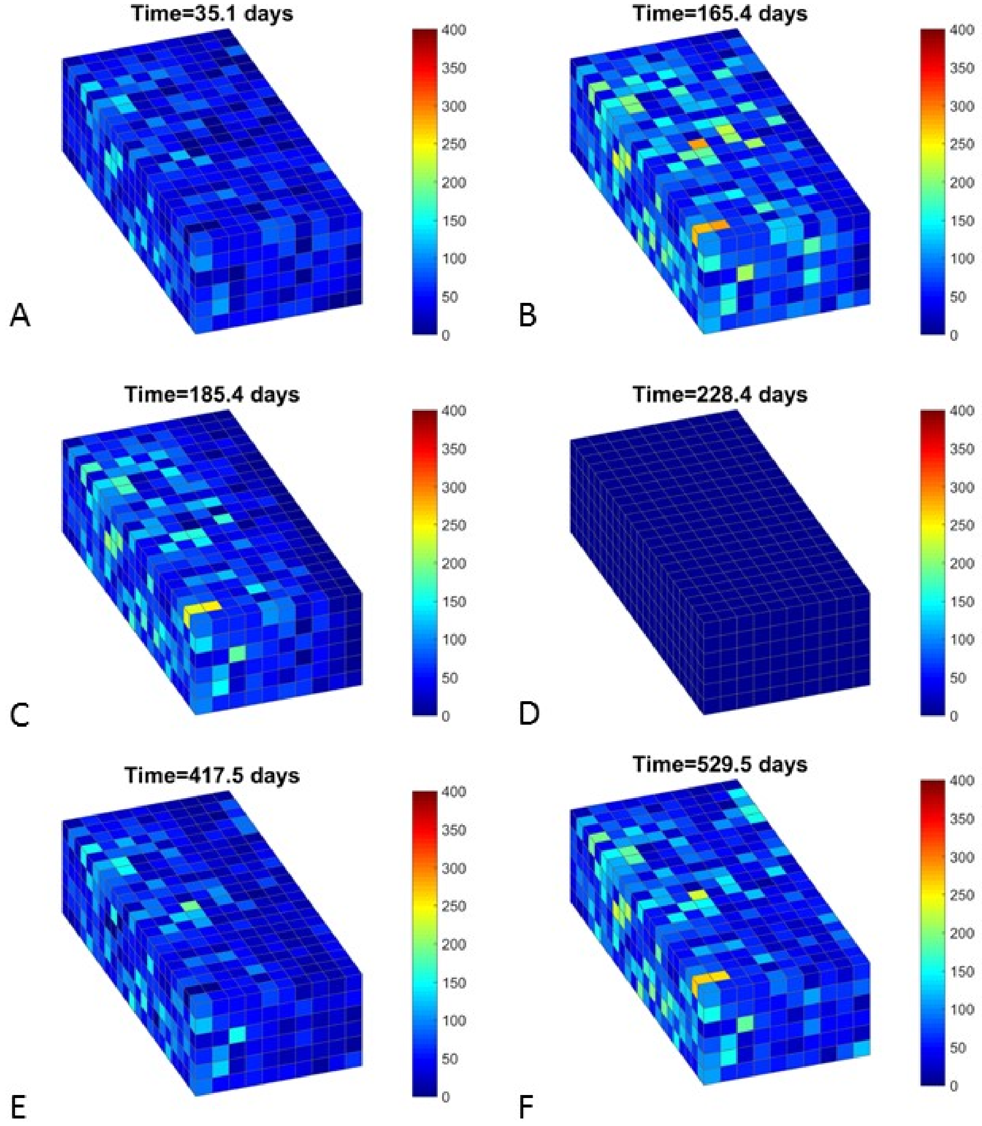
Time=35.1 days

Time=165.4 days

Time=185.4 days

Time=228.4 days

Time=417.5 days

Time=529.5 days

Figure 5.11: Capillary pressure plots for a two fracture simulation run. Plots A is during the initial depletion. Plots B and C are during injection while plot D is at the end of the injection. Plot E is during the secondary depletion and plot F is the end of the secondary depletion.

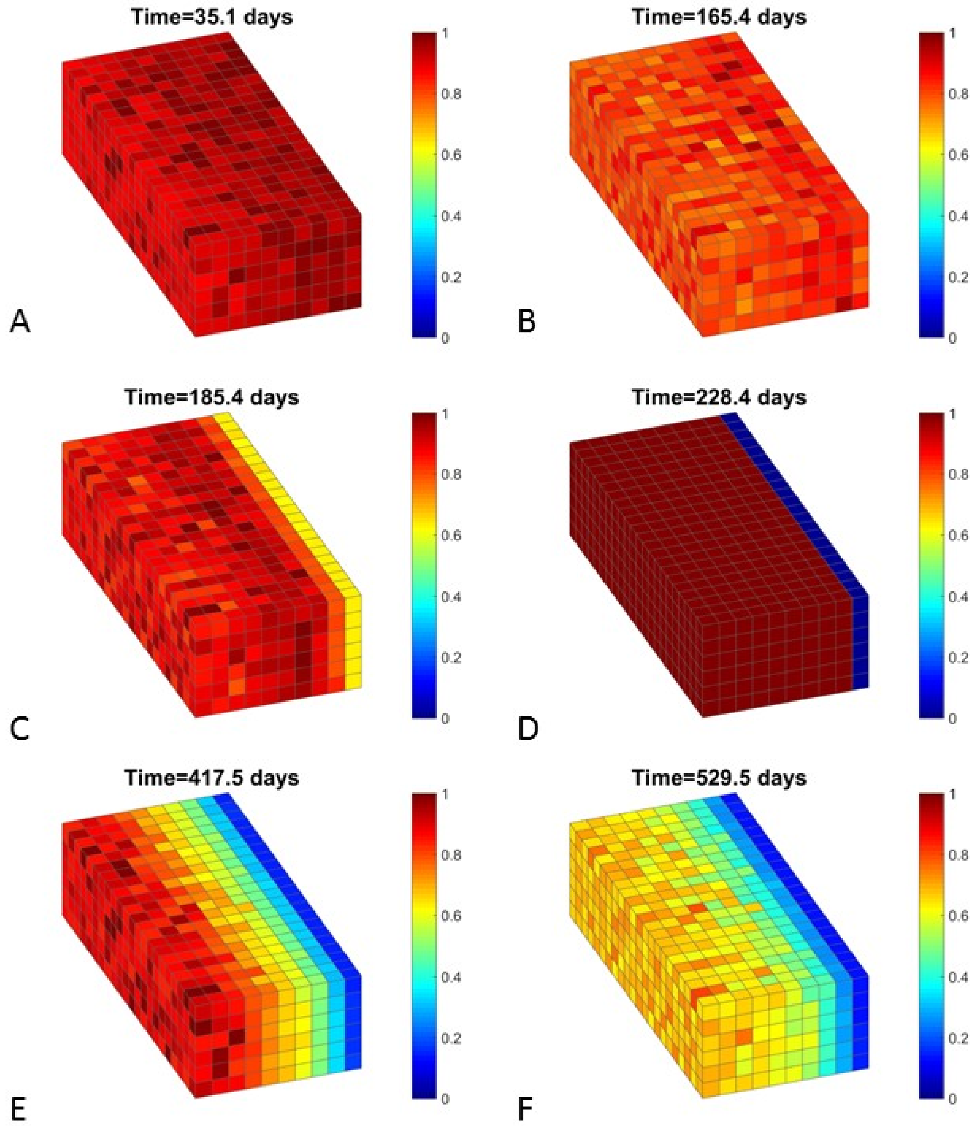

Figure 5.12: Oil saturation plots for a single fracture simulation run. Plots A is during the initial depletion. Plots B and C are during injection while plot D is at the end of the injection. Plot E is during the secondary depletion and plot F is the end of the secondary depletion.

Maximum and minimum cell properties from the preceding figures are summarized in Table 5.4 below.

Table 5.4 Maximum and Minimum Cell Values for Two Fracture Black Oil Run

	Time (days)	So (max)	So (min)	Po (max)	Po (min)	Pcap (max)	Pcap (min)	Z_{CO2} (max)	Z_{CO2} (min)
End of Initial Depletion	160.4	0.99	0.69	1605.8	1324.1	346.2	14.8	0.01	0.01
End of Injection	228.4	1.00	0.0	3149.2	3075.3	0.0	0.0	0.92	0.01
End of 2nd Depletion	529.5	0.88	0.13	1558.5	1357.7	264.2	10.6	0.90	0.04

At the start of the simulation run, the reservoir is single phase oil. It then transitions to two phase flow as the reservoir pressure is reduced due to the depletion. The injection of CO_2 increases the reservoir pressure sufficiently that all cells are single phase by the end of the injection portion of the run. As the pressure reduces during the secondary depletion, the reservoir becomes two phase again.

A crucial difference between the single fracture and two fracture simulations is what happens to the injected gas during the secondary depletion. For the single fracture simulation, much of the injected CO_2 is produced back. For the two fracture simulation run, the injected CO_2 is drawn further into the reservoir as production occurs from the opposite fracture. The CO_2 therefore mixes more completely with the remaining hydrocarbons in the reservoir.

5.2.3 Comparison of Simulations to Mechanistic Model

The mechanistic model is run using the same run parameters used for the reservoir simulation runs described in Sections 5.2.1 and 5.2.2 including the reservoir fluid, starting and ending pressures, injection gas composition and injection gas amount.

The tables below show the recovery of each component during the initial depletion, the recovery during the injection phase and the total recovery at the end of the run. The recoveries are calculated as specified in Eq. 5.1 (initial depletion), Eq. 5.2 (injection) and Eq. 5.3 (total recovery) above. The recoveries predicted by the mechanistic model for all components excluding CO_2 are compared against those from the reservoir simulations using a single fracture in Table 5.5 and for two fractures in Table 5.7. Carbon dioxide recovery is listed separately in Table 5.6 for a single fracture and Table 5.8 for two fractures.

Table 5.5: Molar Recoveries for Mechanistic Model and Single Fracture Reservoir Simulation

Component	C1	C2	C3	N2	Pseudo 1	Pseudo 2	Pseudo 3	Pseudo 4	Total (exclude CO2)
	Initial Depletion Recovery (%)								
Reservoir Simulation	20.0	16.3	14.4	23.1	12.8	11.6	11.2	11.2	15.4
Mechanistic Model	19.5	16.4	14.9	22.3	13.6	12.6	12.3	12.3	15.8
Difference	-0.5	0.1	0.4	-0.8	0.8	1.0	1.1	1.1	0.3
	Injection Recovery (%)								
Reservoir Simulation	11.3	9.6	8.3	16.0	6.5	4.1	2.5	2.1	7.5
Mechanistic Model	29.9	25.3	22.7	33.3	20.1	17.8	17.0	16.9	23.3
Difference	18.6	15.7	14.4	17.4	13.6	13.7	14.5	14.8	15.8
	Total Recovery (%)								
Reservoir Simulation	29.0	24.3	21.5	35.4	18.5	15.2	13.4	13.0	21.8
Mechanistic Model	43.6	37.5	34.2	48.2	31.0	28.1	27.1	27.1	35.4
Difference	14.5	13.2	12.7	12.8	12.5	12.9	13.7	14.1	13.6

Table 5.6: Molar Recovery and Storage of CO_2 for Mechanistic Model and Single Fracture Simulation Run

	Recovery (%)	Storage (%)
	Initial Depletion	
Reservoir Simulation	16.9	83.1
Mechanistic Model	16.9	83.1
Difference	-0.04	0.04
	Injection	
Reservoir Simulation	71.2	28.8
Mechanistic Model	26.2	73.8
Difference	-45.0	45.0
	Total	
Reservoir Simulation	71.3	28.7
Mechanistic Model	26.5	73.5
Difference	-44.8	44.8

For the single fracture simulation, the recovery predicted by the mechanistic model is close to the reservoir simulation results for the initial depletion phase. However, once the injection portion of the run begins, the mechanistic model results are significantly different from the simulation.

The mechanistic model predicts much higher recoveries than those seen in the simulation results. The exception is the recovery of CO_2, which was the injection gas for the run. For CO_2, the reservoir simulation predicts a much higher recovery than the mechanistic model. This corresponds to a higher CO_2 storage for the mechanistic model.

The difference in CO_2 storage between the mechanistic and reservoir simulation models occurs due to key differences in how injection gasses mix with the reservoir fluids. In the mechanistic model, the injected CO_2 is assumed to mix perfectly with the reservoir fluids. As the pores are depleted down to the final pressure, a portion of the injected CO_2 is recovered along with the other components.

This is in contrast to the reservoir simulation where the injected CO_2 only penetrates the reservoir to a limited extent. The cells furthest from the fracture see almost no increase in CO_2 composition. As the reservoir is depleted a second time, much of the injected CO_2 which is located near the fracture is produced back. The hydrocarbons further from the fracture remain in place. Figure 5.6 above shows the movement of CO_2 at select points during the simulation run.

This difference in how the mixing of the injection gas is treated by each model causes the difference in recoveries. The mechanistic model predicts greater storage of injection gas (lower recovery) and higher recoveries of all other components compared to the reservoir simulation model for the single fracture run.

The comparison of the two fracture simulation is summarized in Tables 5.7 and 5.8 and compared against the mechanistic model results.

Table 5.7: Molar Recoveries for Mechanistic Model and Two Fracture Reservoir Simulation

Component	C1	C2	C3	N2	Pseudo 1	Pseudo 2	Pseudo 3	Pseudo 4	Total (exclude CO2)
	Initial Depletion Recovery (%)								
Reservoir Simulation	20.0	16.3	14.4	23.1	12.8	11.6	11.2	11.2	15.4
Mechanistic Model	19.5	16.4	14.9	22.3	13.6	12.6	12.3	12.3	15.8
Difference	-0.5	0.1	0.4	-0.8	0.8	1.0	1.1	1.1	0.3
	Injection Recovery (%)								
Reservoir Simulation	44.7	42.3	41.1	47.9	40.1	39.2	39.0	39.0	41.7
Mechanistic Model	29.9	25.3	22.7	33.3	20.1	17.8	17.0	16.9	23.3
Difference	-14.8	-17.0	-18.4	-14.5	-19.9	-21.5	-22.1	-22.1	-18.3
	Total Recovery (%)								
Reservoir Simulation	55.8	51.7	49.6	59.9	47.7	46.3	45.8	45.8	50.7
Mechanistic Model	43.6	37.5	34.2	48.2	31.0	28.1	27.1	27.1	35.4
Difference	-12.2	-14.2	-15.4	-11.7	-16.8	-18.2	-18.7	-18.7	-15.3

Table 5.8: Molar Recovery and Storage of CO_2 for Mechanistic Model and Two Fracture Simulation Run

	Recovery (%)	Storage (%)
	Initial Depletion	
Reservoir Simulation	16.9	83.1
Mechanistic Model	16.9	83.1
Difference	-0.04	0.04
	Injection	
Reservoir Simulation	2.2	97.8
Mechanistic Model	26.2	73.8
Difference	24.0	-24.0
	Total	
Reservoir Simulation	2.7	97.3
Mechanistic Model	26.5	73.5
Difference	23.9	-23.9

For the initial depletion portion of the run, the simulation results are the same as those presented for the single fracture simulation in Tables 5.5 and 5.6. In both cases, the initial depletion is identical. Once injection starts, the recovery results for the two fracture run show the opposite trend seen in the single fracture results. For the two fracture case, the simulation model has higher recoveries than the mechanistic model for every component other than CO_2. The reservoir simulation shows greater CO_2 storage than the mechanistic model. This difference is again due to the mixing of the injection gas with the reservoir fluids.

When the CO_2 injection and production occur at opposite ends of the reservoir, much of the injected CO_2 remains stored in the reservoir and only a small fraction is produced back during the secondary depletion. The displacement of hydrocarbons by the CO_2 also causes higher recovery of all the other components compared to what is predicted by the mechanistic model. Figure 5.10 shows the CO_2 composition throughout the reservoir during the simulation run. This figure clearly shows that only a small amount of the injected CO_2 reaches the producing fracture during the secondary depletion. Therefore, most of the injected CO_2 remains in the reservoir.

Figure 5.13 below compares the capillary pressure plots generated using the mechanistic model with those from the single fracture and two fracture simulation runs. The oil saturation and capillary pressures are pore volume weighted, average values for the entire reservoir.

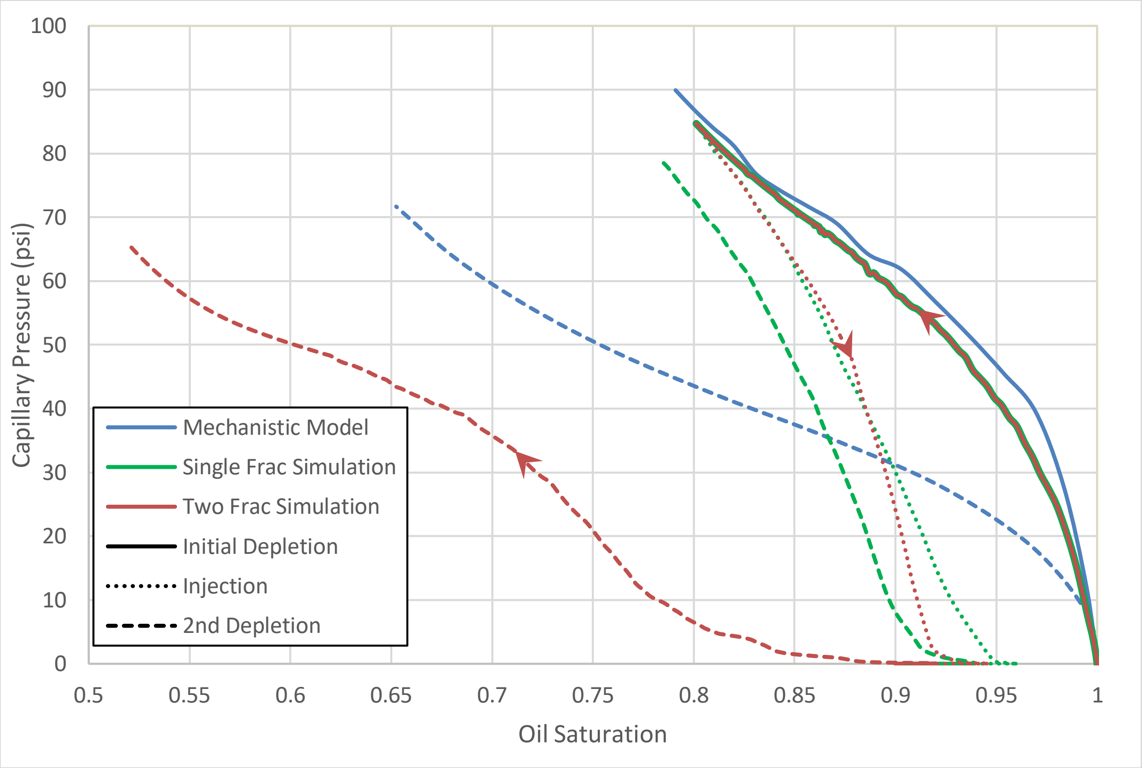

Figure 5.13: Comparison of capillary pressure plot from the mechanistic model, single fracture simulation and two fracture simulation. Line color indicates model (i.e. mechanistic, one or two fracture) while line type indicates the portion of the run (i.e. depletion, injection or secondary depletion). The arrows indicate the time progression of the simulation. The one and two fracture simulations have the same initial depletion data, therefore both lines lay exactly on top of one another. The injection capillary data for the mechanistic model is not plotted.

For the initial depletion portion of the run, the capillary pressure plot for the mechanistic model matches the reservoir simulation results fairly well. The one fracture and two fracture reservoir simulation results are identical because the initial depletion is identical for both runs.

For the secondary depletion, the results of the two different simulation runs are different from one another and are also different from the mechanistic model results. The single fracture curve has the steepest increase in capillary pressure as oil saturation decreases while the two fracture curve has the shallowest increase in capillary pressure. The capillary pressure curve from the mechanistic model lies roughly in between the two simulation curves.

This difference is again explained by how the mixing of the injection gas is modeled. It is important to note that CO_2 is very miscible with hydrocarbons and causes a decrease in interfacial tension between the liquid and vapor phases. For the single fracture simulation, a large portion of the injected CO_2 is removed from the reservoir during secondary depletion. This results in the steep increase in capillary pressure during secondary recovery. For the two fracture simulation, most of the injected gas remains stored in the reservoir. The CO_2 mixes with the reservoir fluids which decreases the interfacial tension and therefore results in the gradual increase in capillary pressure seen in Figure 5.13. The mechanistic model is an intermediate between the two simulation results. The injected CO_2 mixes completely with the reservoir fluids but a significant portion of the CO_2 is produced back during the secondary depletion. Therefore, the amount of CO_2 stored is less than in the two fracture simulation but greater than in the one fracture simulation. This results in a capillary pressure curve that lies roughly between the two sets of simulation results as seen in Figure 5.13.

5.3 Application of Mechanistic Model to a Volatile Oil Reservoir

The previous section compares the mechanistic model against simulation results for a black oil. In this section, a similar comparison is shown using an Eagle Ford volatile oil. The following run parameters are used for the reservoir simulation runs:

Fluid Model – The composition of the volatile oil used is provided in Table A.2 in the Appendix.

Pore Size Distribution – The same pore size distribution described in Section 5.1 and used for the simulation runs in Section 5.2 is used.

Relative Permeability Curves – A new set of relative permeability curves are calculated for this reservoir fluid and injection gas combination. The curves were calculated according to the process described in Section 3.2 and are shown in Figure 5.14 below.

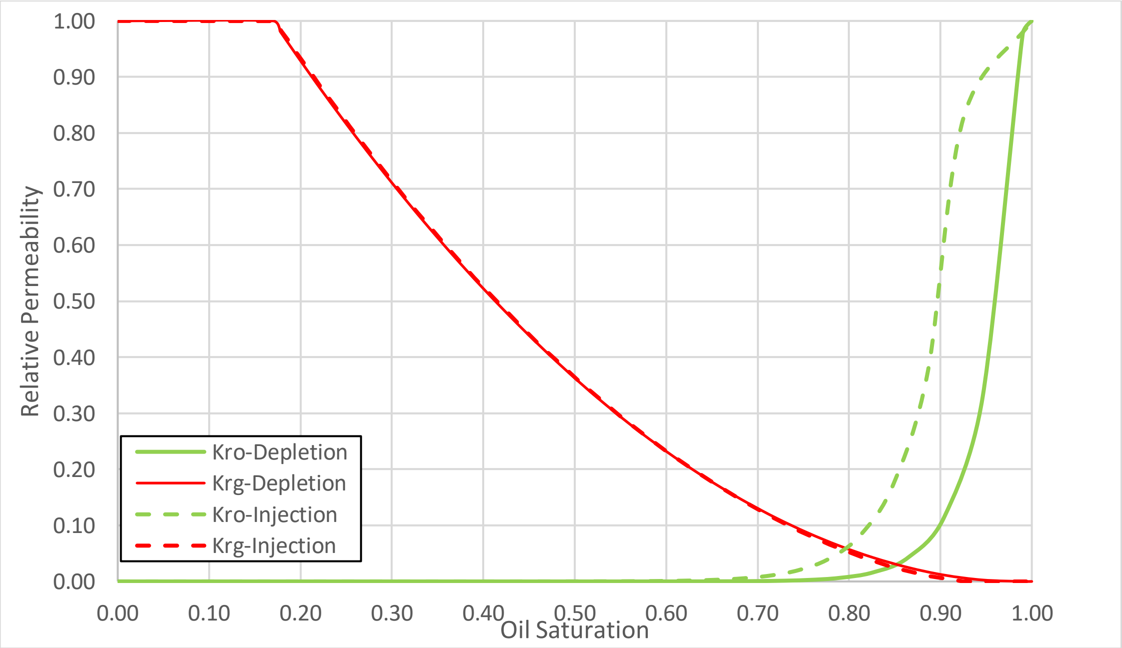

Figure 5.14: Calculated relative permeability curves for the depletion and injection portions of a reservoir simulation using a volatile oil and methane injection. The injection curves are also used for the secondary depletion.

Reservoir Model – The same reservoir model described in Section 5.2 is used for this set of reservoir simulations. The dimensions and number of cells are held constant.

Depletion and Injection Sequence – The same sequence of initial depletion, gas injection and then secondary depletion is modeled in these simulations. A key difference is that the starting pressure used is 3800 psia which is selected because it is just above the bubble point of the volatile oil. The depletion ends at an average reservoir pressure of 2000 psia. The amount of injection gas is again set to 30 lbmol for every 100 lbmol of hydrocarbons initially in place. This is the same proportion used for CO_2 injection in the black oil reservoir in Section 5.2. For these runs, C_1 is used as the injection gas. There are two key differences noted about the use of methane as an injection gas. The first is that methane (C_1) is considerably less miscible with hydrocarbons than carbon dioxide. The second is that the starting composition of the reservoir fluid contains 65% C_1. For the black oil injection runs in Section 2.2, CO_2 was less than 1% of the starting oil composition.

5.3.1 Single Fracture Run for Volatile Oil

As was done with the black oil reservoir in Section 5.2, the reservoir simulations will evaluate the difference between the use of a single fracture for both depletion and injection compared to two separate fractures; one for depletion and the other for injection.

The results for the single fracture are summarized in this section. The following figure shows the reservoir pressure at select times during the simulation run. The fracture located on the left side of the model is used for both depletion and injection operations.

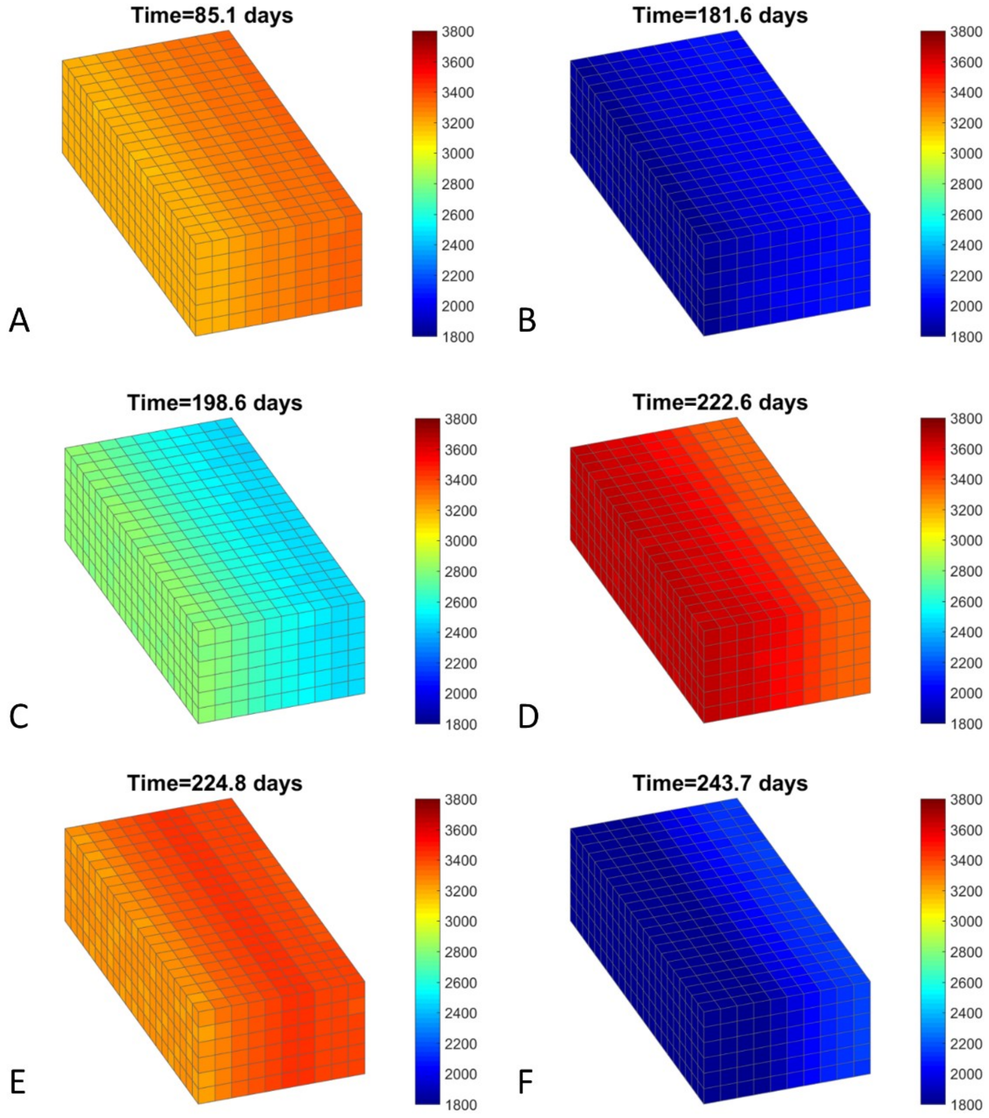

Time=85.1 days

Time=181.6 days

Time=198.6 days

Time=222.6 days

Time=224.8 days

Time=243.7 days

Figure 5.15: Pressure plots (in psia) for a single fracture simulation for a volatile oil reservoir. Plot A is during the initial depletion. Plot B is at the end of the initial depletion. Plot C is during the injection phase and plot D is the end of injection. Plot E is during the secondary depletion and plot F is the end of the secondary depletion (end of entire simulation).

Figure 5.15 shows how a pressure gradient develops along the depth of the reservoir and changes over the course of the simulation. The following figure shows the molar composition of C_1 for select times during the simulation run.

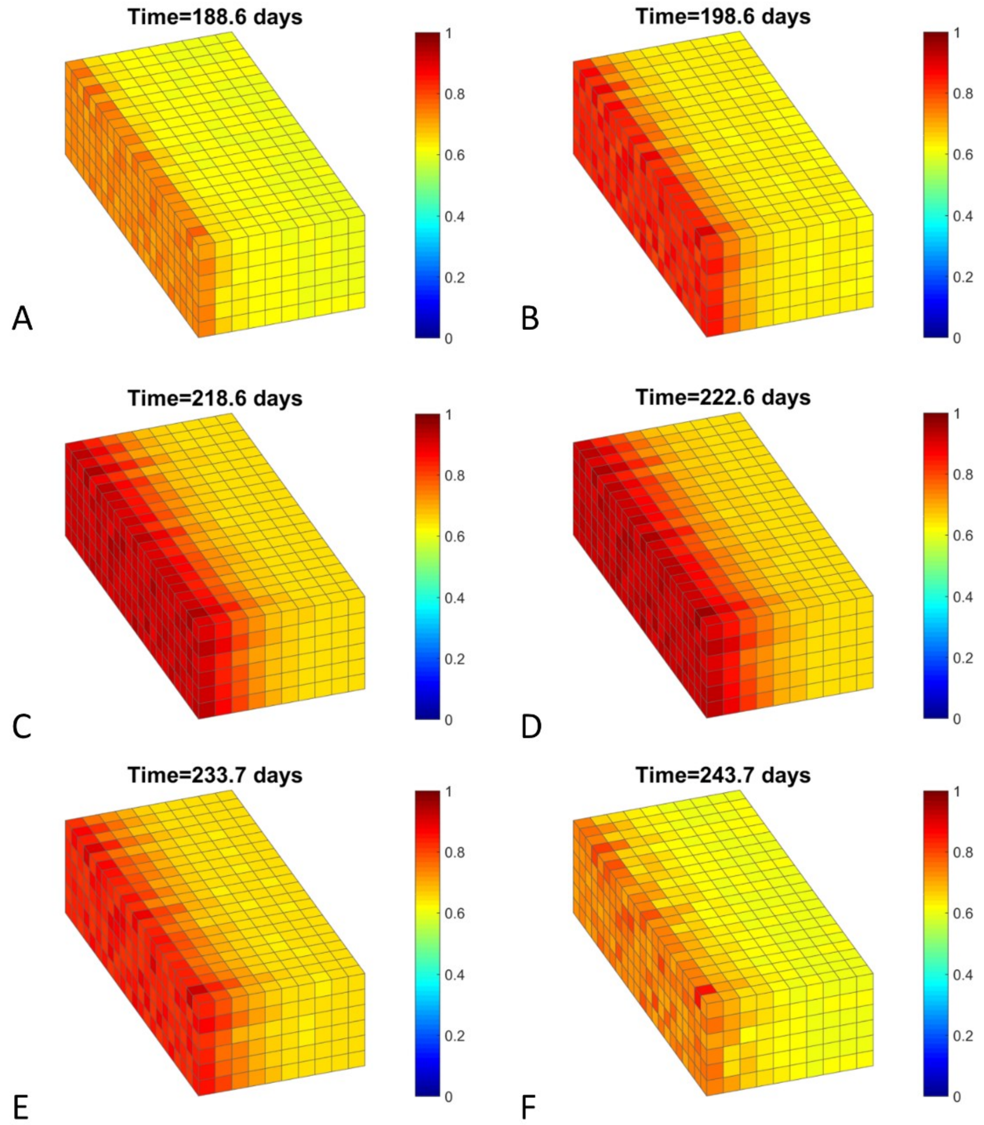

Figure 5.16: Methane composition plots for a single fracture simulation for a volatile oil reservoir. Plots A, B, and C are during the injection phase of the simulation run. Plot D is at the end of injection. Plot E is during the secondary depletion and plot F is the end of the secondary depletion (end of entire simulation).

As stated before, the initial volatile oil composition is 65% methane. During the initial depletion, the methane composition changes very little, therefore, plots from the initial depletion are not shown. The molar fraction of methane increases during the injection with the highest composition in the cells closest to the fracture on the left side of the model. During the secondary depletion, much of the injected methane is produced back. This production combined with an influx of reservoir fluids from deeper within the reservoir causes the methane composition in the cells to decrease again.

Figure 5.17 shows the capillary pressure in the reservoir during select points during the simulation. Figure 5.18 shows the oil saturation at the corresponding times.

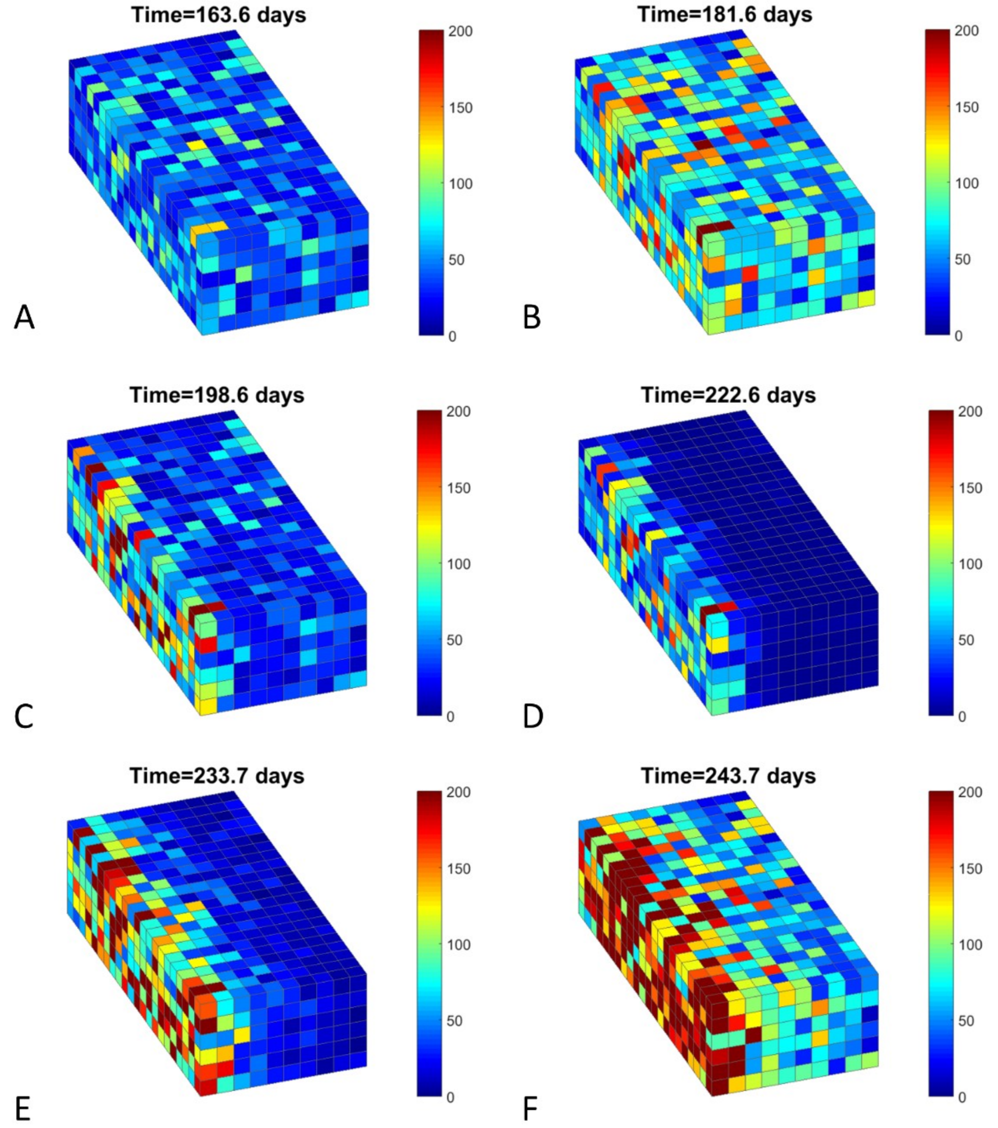

Figure 5.17: Capillary pressure plots (in psi) for a single fracture simulation for a volatile oil reservoir. Plot A is during the initial depletion. Plot B is at the end of the initial depletion. Plot C is during injection and plot D is at the end of injection. Plot E is during the secondary depletion and plot F is the end of the secondary depletion (end of entire simulation).

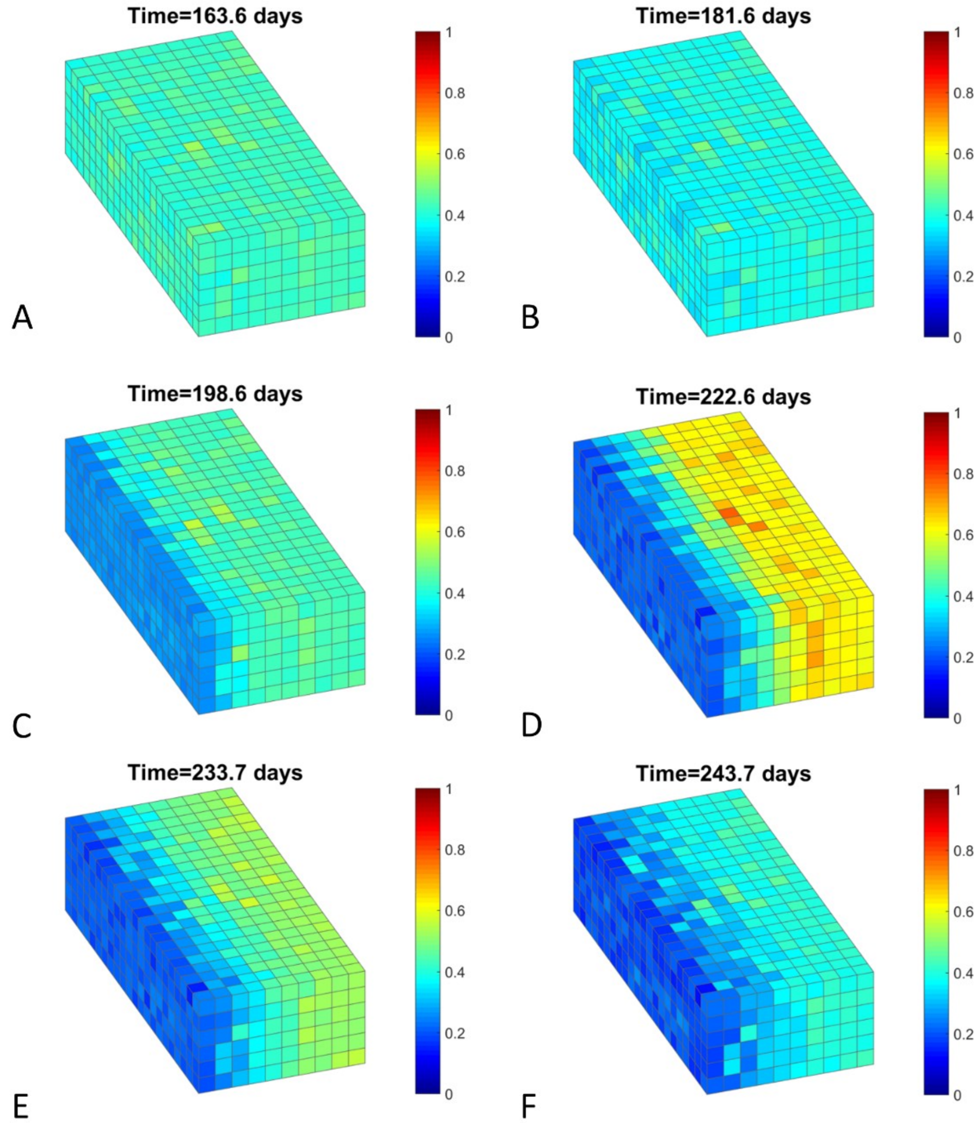

Figure 5.18: Oil saturation plots for a single fracture simulation for a volatile oil reservoir. Plot A is during the initial depletion. Plot B is at the end of the initial depletion. Plot C is during injection and plot D is at the end of injection. Plot E is during the secondary depletion and plot F is the end of the secondary depletion (end of entire simulation).

The maximum and minimum cell values are summarized in the table below.

Table 5.9 Maximum and Minimum Cell Values for Single Fracture Volatile Oil Run

	Time (days)	So (max)	So (min)	Po (max)	Po (min)	Pcap (max)	Pcap (min)	Z_{C1} (max)	Z_{C1} (min)
End of Initial Depletion	181.6	0.52	0.32	2073.9	1815.3	227.5	13.7	0.61	0.58
End of Injection	222.6	0.81	0.15	3659.7	3337.9	218.4	0.5	0.95	0.64
End of 2nd Depletion	243.7	0.51	0.13	2160.3	1417.1	579.9	12.1	0.85	0.60

During the initial depletion, the reservoir starts at 100% oil saturation but quickly enters two phase flow. Plot B of Figure 5.18 shows a fairly uniform oil saturation at the end of the initial depletion. However, the capillary pressure at the same time (plot B in Figure 5.17) shows a large variability in the capillary pressures of individual cells. This occurs due to the different pore sizes assigned to individual cells. The highest capillary pressures correspond to cells assigned the smallest diameters.

During the gas injection shown in plots C and D in Figure 5.18, the oil saturation changes differently depending on cells location. The cells farthest from the fracture (right side of the reservoir) see an increase in oil saturation. This occurs due to the pressure increase in the reservoir resulting from injection. However, the cells closest to the fracture (left side of reservoir), which experience an even larger increase in pressure, experience a decrease in oil saturation. This occurs because the fluid composition in these cells has been altered due to the injection gas, as seen in Figure 5.16. The large amount of methane in these cells creates a volatile mixture which results in a decrease oil saturation in spite of the increased pressure.

During secondary depletion, the cells farthest from the fracture see a decrease in oil saturation as the pressure in the reservoir decreases again. The cells close to the fracture face only see a small change in oil saturation. During the secondary depletion, the pressure in these cells decreases which would tend to decrease oil saturation. At the same time, the methane composition of these cells decreases which tends to increase the oil saturation as the methane in the cells is replaced by heavier components. These two effects working in opposite directions cause the oil saturation to remain essentially unchanged in these cells.

5.3.2 Two Fracture Run for Volatile Oil

This section examines the reservoir simulation results when separate fractures are used for depletion and for injection. The fracture on the left side of the reservoir is used for initial and secondary depletion. The fracture on the right side of the model is used for gas injection. Other than this, all other aspects of the run are identical to the single fracture run for the volatile oil. Figure 5.19 shows the reservoir pressure at select times during the simulation.

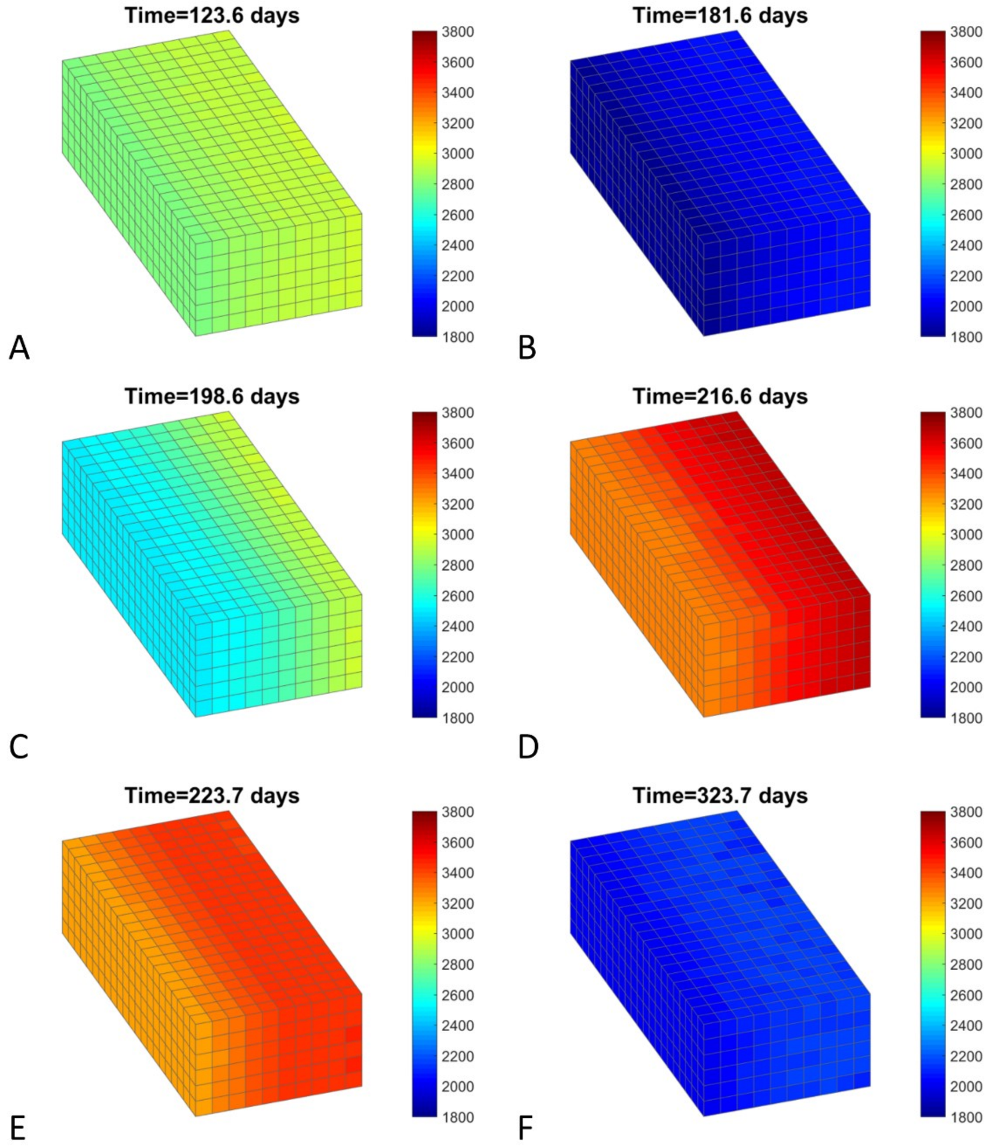

Time=123.6 days

Time=181.6 days

Time=198.6 days

Time=216.6 days

Time=223.7 days

Time=323.7 days

Figure 5.19: Pressure plots (in psia) for a two fracture simulation for a volatile oil reservoir. Plot A is during the initial depletion. Plot B is at the end of the initial depletion. Plot C is during the injection phase. Plots D is the end of injection. Plots E and F are during the secondary depletion.

Since depletion and injection occur through opposite fractures, the cells on the right side of the model maintain a higher pressure than those on the left side throughout the duration of the run.

The following figure shows the C_1 composition during the injection and secondary depletion portions of the simulation run.

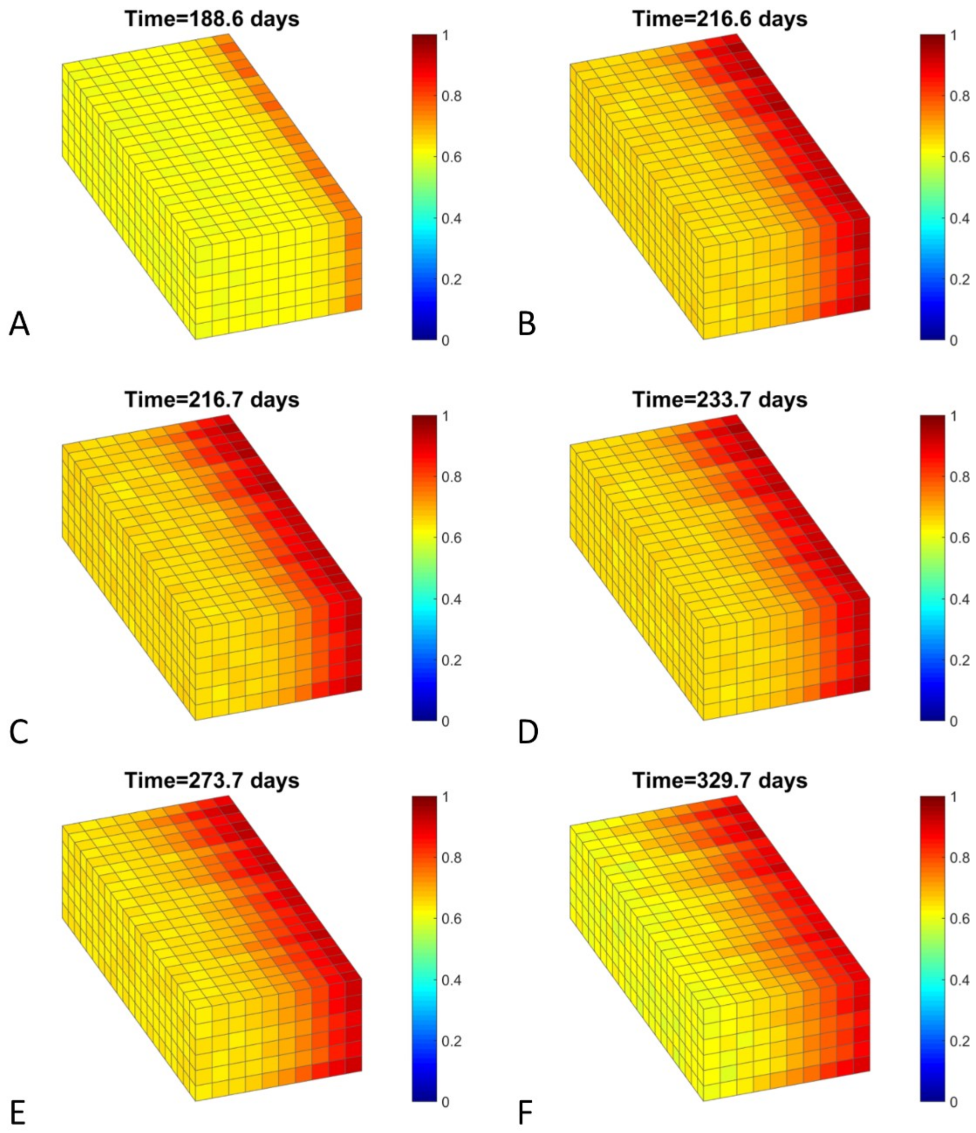

Figure 5.20: Methane composition plots for a two fracture simulation for a volatile oil reservoir. Plot A is during the injection. Plot B is at the end of injection. Plots C, D, and E are during the secondary depletion. Plot F is the end of the secondary depletion (end of entire simulation).

During injection the C_1 composition of all cells increases with the greatest increase occurring in the cells nearest the fracture on the right side. During the secondary depletion, the C_1 composition decreases a small amount in the cells on both the right and left sides of the reservoir. The cells in the middle of the reservoir do not experience much change in C_1 composition. Figure 5.21 shows the capillary pressure during select times during the simulation run. Figure 5.22 shows the oil saturations at the corresponding times.

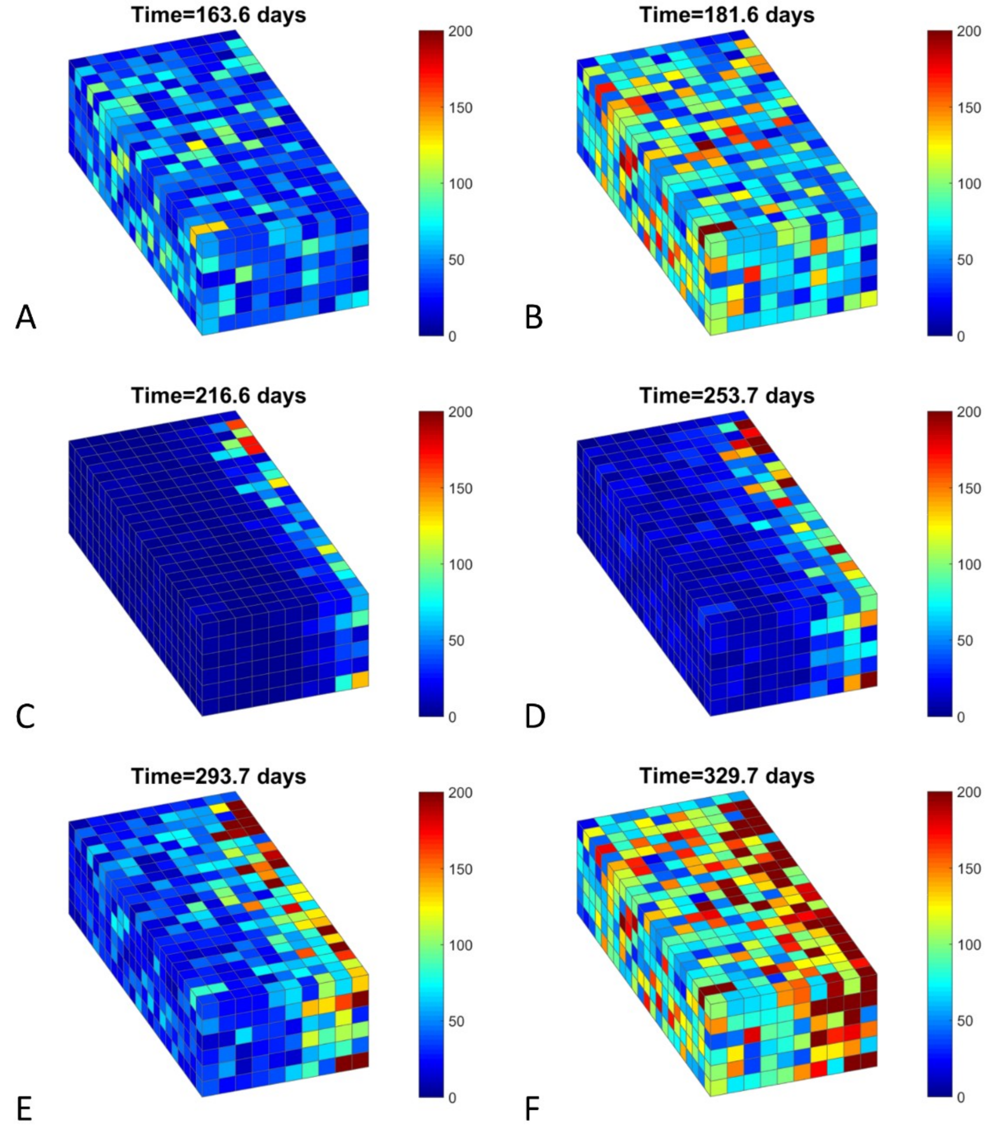

Figure 5.21: Capillary pressure plots for a two fracture simulation for a volatile oil reservoir. Plot A is during the initial depletion. Plot B is at the end of the initial depletion. Plot C is at the end of injection. Plot D and E are during the secondary depletion and plot F is the end of the secondary depletion (end of entire simulation).

The following figure shows the oil saturation plots during the simulation.

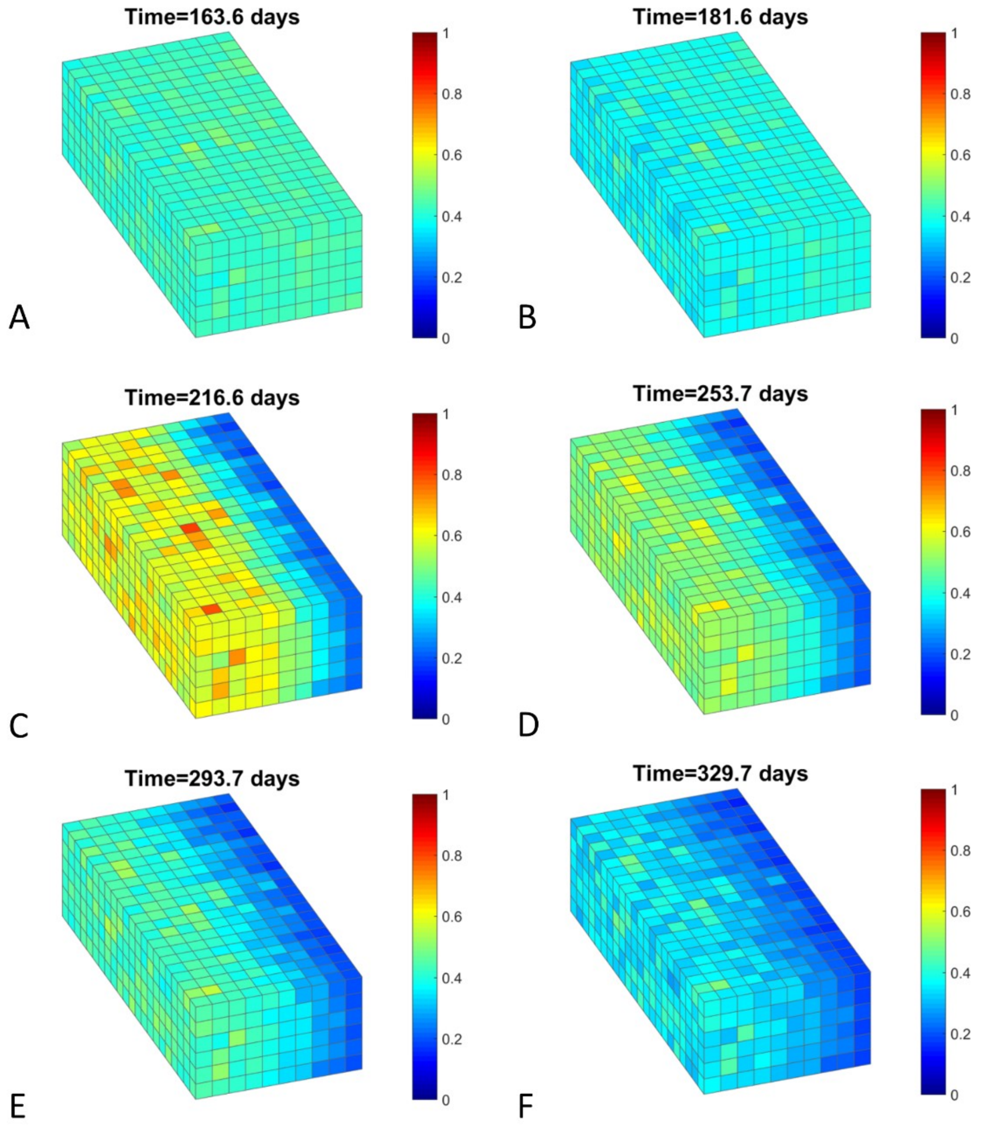

Figure 5.22: Oil saturation plots for a two fracture simulation for a volatile oil reservoir. Plot A is during the initial depletion. Plot B is at the end of the initial depletion. Plot C is at the end of the injection. Plot D and E are during the secondary depletion and plot F is the end of the secondary depletion (end of entire simulation).

Table 5.10 Maximum and Minimum Cell Values for Two Fracture Volatile Oil Run

	Time (days)	So (max)	So (min)	Po (max)	Po (min)	Pcap (max)	Pcap (min)	Z_{C1} (max)	Z_{C1} (min)
End of Initial Depletion	181.6	0.52	0.32	2073.9	1815.3	227.5	13.7	0.61	0.58
End of Injection	216.6	0.82	0.16	3666.5	3279.5	197.8	0.8	0.95	0.63
End of 2nd Depletion	329.7	0.49	0.14	2034.2	1824.9	573.7	19.9	0.93	0.58

During initial depletion, the oil saturation in plots A and B in Figure 5.22 decreases as the reservoir pressure decreases. Accordingly, the capillary pressures in Figure 5.21 increase. At the end of injection, plot C, the cells farthest from the fracture see an increase in oil saturation and a decrease in capillary pressure. The cells near the fracture see a decrease in oil saturation and an increase in capillary pressures. Even though, the entire reservoir experiences a pressure increase due to the addition of injection gas, the large increase in C_1 molar composition in the cells near the injection fracture on the right side causes the decrease in oil saturation observed.

The secondary depletion reduces the reservoir pressure again and a decrease in oil saturation occurs throughout the reservoir as seen in plots C, D and E in Figure 5.22.

5.3.3 Comparison of Simulations to Mechanistic Model for Volatile Oil

In this section, the reservoir simulation results are compared against the mechanistic model results for molar recovery and capillary pressure. To the greatest degree possible, the mechanistic model uses the same input parameters as the reservoir simulation. It is noted that the mechanistic model does not consider fracture location. Therefore, the mechanistic model is only run once and the mechanistic results are the same in Tables

5.11 and 5.12. The mechanistic model is initially compared against the single fracture simulation.

Table 5.11: Molar Recoveries for Mechanistic Model and Single Fracture Reservoir Simulation for Volatile Oil

Component	C1	C2	C3	nC4	iC4	nC5	iC5	C6	N2	CO2	C7+	Total
	Initial Depletion Recovery (%)											
Reservoir Simulation	40.4	34.0	29.2	24.4	26.0	20.3	21.3	17.0	44.1	34.9	5.3	35.1
Mechanistic Model	40.1	33.9	29.2	24.6	26.1	20.6	21.6	17.5	43.7	34.7	6.1	34.9
Difference	-0.3	-0.2	0.0	0.1	0.1	0.3	0.3	0.4	-0.4	-0.2	0.7	-0.2
	Injection Recovery (%)											
Reservoir Simulation	40.4	12.7	11.3	9.6	10.1	7.8	8.2	6.5	19.0	13.1	1.0	31.8
Mechanistic Model	40.6	34.7	29.9	24.9	26.5	20.4	21.4	16.7	43.7	35.6	3.7	35.9
Difference	0.3	22.0	18.6	15.3	16.4	12.5	13.2	10.3	24.7	22.5	2.7	4.2
	Total Recovery (%)											
Reservoir Simulation	56.8	42.4	37.2	31.7	33.5	26.5	27.8	22.4	54.7	43.4	6.3	50.1
Mechanistic Model	56.8	56.8	50.3	43.3	45.7	36.8	38.4	31.3	68.3	57.9	9.6	53.0
Difference	0.04	14.4	13.1	11.7	12.2	10.2	10.6	8.9	13.6	14.5	3.3	3.0

Similar to what was observed with the black oil comparison in Section 5.2.3, the mechanistic model matches the reservoir simulation results closely for the initial depletion portion of the run. The mechanistic model is much less accurate for the injection and total recoveries.

For the injection results, both the reservoir simulation and mechanistic model predict a similar recovery of C_1. For all other components, the mechanistic model predicts higher recoveries than the reservoir simulation run. This is true for both the injection recoveries and total recoveries in Table 5.11. As seen in Figure 5.16, the injected C_1 only penetrates into the reservoir to a limited extent and therefore does not have a chance to mix thoroughly with the reservoir fluids. Once again, this is in contrast to the complete mixing assumed in the mechanistic model which causes the higher predicted recoveries. The results for the two fracture simulation are compared below.

Table 5.12: Molar Recoveries for Mechanistic Model and Two Fracture Reservoir Simulation for Volatile Oil

Component	C1	C2	C3	nC4	iC4	nC5	iC5	C6	N2	CO2	C7+	Total
	Initial Depletion Recovery (%)											
Reservoir Simulation	40.4	34.0	29.2	24.4	26.0	20.3	21.3	17.0	44.1	34.9	5.3	35.1
Mechanistic Model	40.1	33.9	29.2	24.6	26.1	20.6	21.6	17.5	43.7	34.7	6.1	34.9
Difference	-0.3	-0.2	0.0	0.1	0.1	0.3	0.3	0.4	-0.4	-0.2	0.7	-0.2
	Injection Recovery (%)											
Reservoir Simulation	35.6	46.7	37.4	29.1	31.7	22.5	24.0	17.7	75.4	48.5	3.4	33.9
Mechanistic Model	40.6	34.7	29.9	24.9	26.5	20.4	21.4	16.7	43.7	35.6	3.7	35.9
Difference	5.0	-12.0	-7.6	-4.2	-5.2	-2.1	-2.5	-0.9	-31.7	-12.9	0.4	2.0
	Total Recovery (%)											
Reservoir Simulation	53.3	64.8	55.7	46.4	49.5	38.2	40.2	31.7	86.2	66.5	8.5	51.6
Mechanistic Model	56.8	56.8	50.3	43.3	45.7	36.8	38.4	31.3	68.3	57.9	9.6	53.0
Difference	3.49	-8.0	-5.4	-3.1	-3.8	-1.4	-1.8	-0.4	-17.9	-8.5	1.1	1.4

For the two fracture simulation, initial depletion is exactly the same as the single fracture results in Table 5.11. For the injection recovery, the mechanistic model predicts a higher recovery of C_1. For all other components besides the C_{7+} fraction, the mechanistic model predicts lower molar recoveries than the simulation result. Because the injection and production occur from opposite ends of the reservoir, the injection gas forces more of the other components towards the producing fracture. At the same time, a large portion of the injected C_1 does not reach the producing fracture and is left behind in the reservoir, as seen in Figure 5.20. For the C_{7+} fraction, both models predict a similar very small recovery indicating that in both models, most of the C_{7+} fraction is left behind in the reservoir.

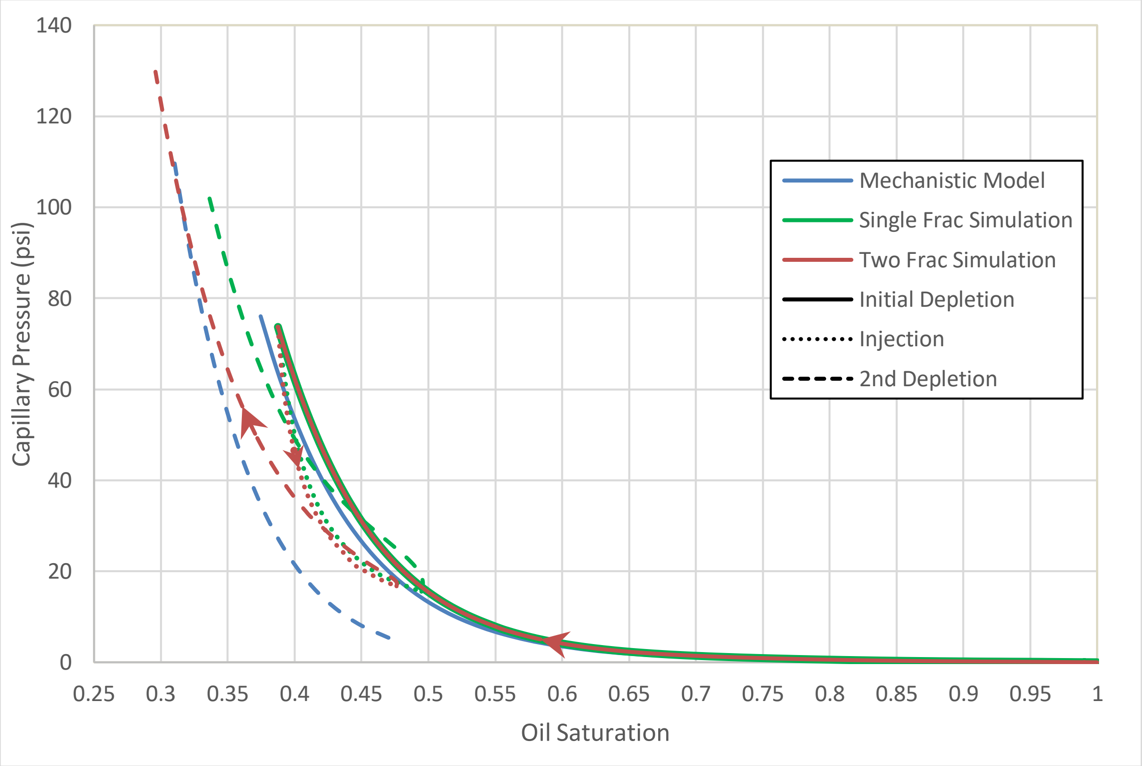

Figure 5.23: Comparison of capillary pressure plot from the mechanistic model, single fracture simulation and two fracture simulation for a volatile oil reservoir. Line color indicates model (i.e. mechanistic, one or two fracture) while line type indicates the part of the model (i.e. depletion, injection or secondary depletion). The arrows indicate the time progression of the simulation. The one and two fracture simulations have the same initial depletion data, therefore both lines lay exactly on top of one another. The injection capillary data for the mechanistic model is not plotted.

The capillary pressure results for the two simulation runs and the mechanistic model are shown in Figure 5.23 above. For the initial depletion, the capillary results from the mechanistic model match the simulation results closely. During the initial depletion, the capillary pressure remains very low from an oil saturation of 1.0 down to approximately

0.6. This occurs because the reservoir fluid is a near critical fluid and therefore the interfacial tension between the oil and gas phases is low which results in a low capillary pressure. As the pressure is reduced, the oil saturation decreases and the oil and gas phases become increasingly compositionally dissimilar. This causes the increase in capillary pressure seen in Figure 5.23. This behavior is in contrast to the capillary results for the Eagle Ford black oil in Figure 5.13 which show much larger values for capillary pressure.

During the injection portion of the run, the additional C_1 added causes a decrease in capillary pressure and a small increase in oil saturation. During secondary recovery, the capillary pressure begins to increase again as oil saturation decreases. The simulation results and the mechanistic model show the same general trend, however, the mechanistic model does not match either simulation result very closely for the secondary depletion. Again, this discrepancy arises out of the way the mechanistic model handles mixing of injection gas compared to the reservoir simulations.

5.4 Discussion of the Accuracy of the Mechanistic Model

As discussed above, the mechanistic model matches the simulation results for the initial depletion fairly closely but is not able to match the simulation results for injection or secondary depletion. This is true for both the black oil (Section 5.2) and the volatile oil (Section 5.3) comparisons.

It is however noted that the mechanistic model matches the secondary depletion results for the volatile oil much more closely than for the black oil. This is seen in the capillary pressure curves in Figure 5.13 (black oil) and Figure 5.23 (volatile oil).

To help illustrate the source of this difference, the molar composition in a row of cells is recorded and plotted over the course of the simulation runs evaluated above. Figure 5.24 below shows the row of cells selected for this comparison.

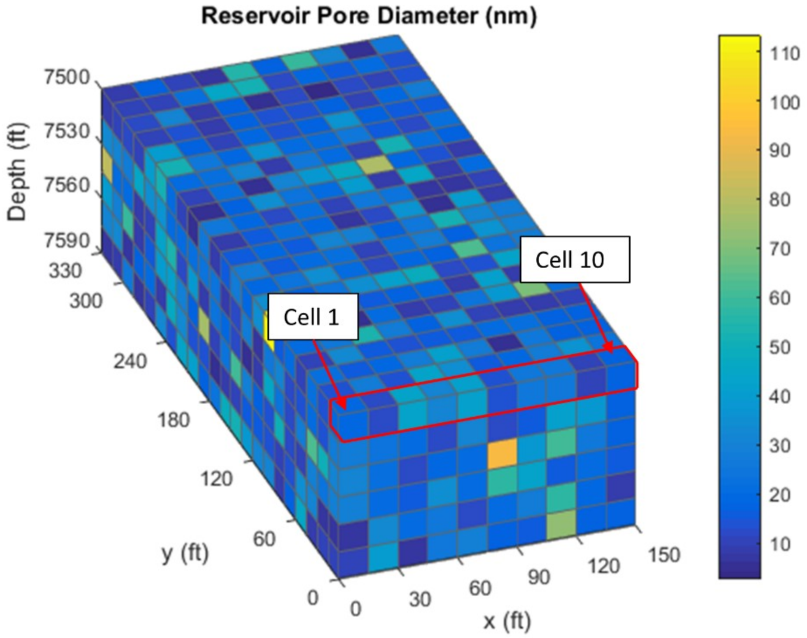

Figure 5.24: Reservoir model with pore sizes identified. The row of cells boxed in red indicates the cells that are examined in this section. The cells are numbered sequentially from cell 1 to cell 10 as pictured.

For reference, the initial depletion and secondary depletion for all runs occur through the fracture touching cell 1. For the single fracture simulations, the injection also occurs through the fracture touching cell 1. For the two fracture simulations, injection occurs through the fracture in contact with cell 10.

For the cells identified, the molar composition of the injection gas is plotted during the course of the simulation run in Figure 5.25 below. Each plot includes the initial depletion, injection, and secondary depletion portions of the simulation. The results from the following four simulations runs are examined:

1) one fracture black oil reservoir fluid simulation with CO_2 injection (Section 5.2.1),
2) two fracture black oil simulation with CO_2 injection (Section 5.2.2),
3) single fracture volatile oil reservoir fluid simulation with C_1 injection (Section 5.3.1),
4) two fracture volatile oil simulation with C_1 injection (Section 5.3.2).

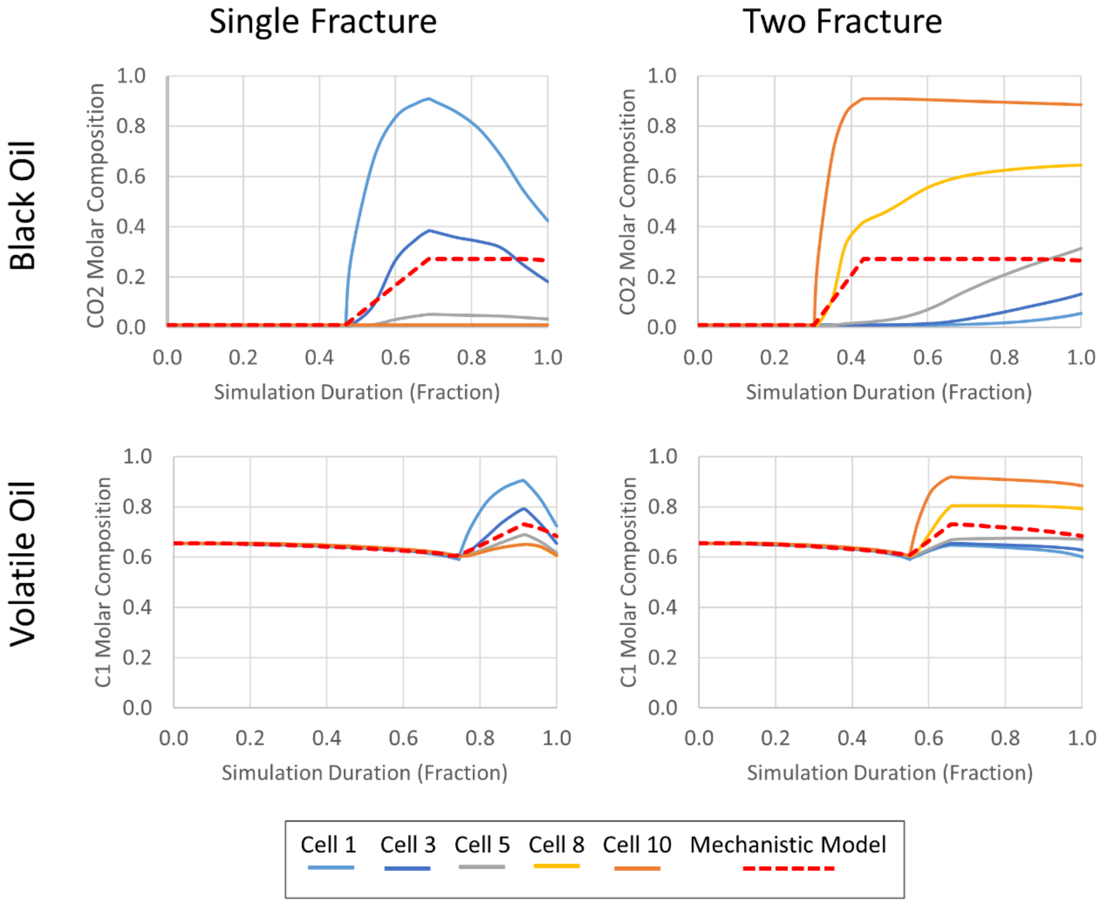

Figure 5.25: Injection gas compositions in individual reservoir model cells for four different simulation runs. Each plot also contains the results from the mechanistic model for the corresponding conditions. Each run starts with the initial depletion. The increase in composition marks the injection portion of the simulation. The subsequent decrease in composition indicates the start of secondary depletion.

The plots in the figure above correspond to composition plots shown in Figure 5.6 and 5.10 for the black oil runs and Figure 5.16 and Figure 5.20 for the volatile oil runs. The results from the mechanistic model are included in each plot. It is noted that the mechanistic model does not consider time so the mechanistic results are assigned a timespan that matches the corresponding simulation results to allow direct comparison.

This is done so that each portion of the simulation (initial depletion, injection and secondary depletion) matches the same portion of the mechanistic model results.

One consequence of this approach is that the timespan of the mechanistic results may appear “stretched” or “compressed”. For example, for the black oil simulations, the same mechanistic model results are used for both the single fracture and two fracture plots. For the two fracture simulation, the secondary depletion occupies approximately 60% of the total simulation time. For the single fracture, the secondary depletion only occupies approximately 35% of the total simulation time. For both cases, the mechanistic results are proportioned to match the corresponding fraction of the total simulation time.

From the plots in the Figure 5.25, it is seen that for the initial depletion, the injection gas compositions in each of the cells match one another very closely. The results also match the mechanistic model results closely. This explains why the mechanistic model is able to match the simulation results so closely for the initial depletion for both the black oil and volatile oil results.

This is in contrast to the injection and secondary depletion portions of the simulations in the Figure 5.25. During these portions of the runs, the compositions in the individual cells begin to diverge from one another. The largest changes occur in the cells in contact with the injection fracture (cell 1 or cell 10 depending on which fracture is used for injection). In each case, the mechanistic model results represent a rough average of the individual cell compositions but it is difficult to accurately represent the complex behavior of each individual cell with a single average value. This presents a key limitation of the mechanistic model and explains why the mechanistic model does not match the simulation results closely for the secondary depletion for either fluid.

For the black oil simulations, the spread in the compositions between cell 1 and cell 10 is very large compared to the volatile oil simulations. Therefore, for the black oil model the difference between the mechanistic model plot and that of any individual cell is larger than for the volatile oil results. This difference helps explain why, for the volatile oil, the capillary pressure plot from the mechanistic model in Figure 5.23 has the same general trend as the curves from the simulation runs. This is in contrast to the black oil capillary pressure curves in Figure 5.13 where the mechanistic model result is very different from either of the simulation results. The mechanistic model is able to more closely approximate the behavior of the individual cells for the volatile oil runs than for the black oil runs.

6. EFFECTS OF CONFINEMENT ON RESERVOIR SIMULATION RESULTS AND PRODUCTION

In this chapter, the effect of confinement on production is examined. For each fluid considered, each simulation is run twice, once with confinement effects enabled and again with confinement effects off (i.e. bulk fluid behavior). The production results from the two runs are compared and analyzed below. Other than confinement, all other run parameters are held constant between runs. Only two fracture simulation runs, where opposite fractures are used for injection and production, are evaluated.

The following naming convention for simulation runs is used throughout this section:
Confinement On – This simulation run is conducted with confinement effects turned on as described in Section 2 and Section 4 above. For this run, the capillary pressure in each cell is calculated as part of the flash calculation.
Confinement Off – This simulation run is conducted with confinement effects turned off and capillary pressure has no impact on any portion of the simulation calculations. The standard Peng Robinson equation of state with volume translation is used in the flash calculations.

6.1 Black Oil Simulation Results

In this section, reservoir simulation results for the Eagle Ford black oil composition (Table A.1 in Appendix A) are examined with CO_2 used as the injection gas. Confinement effects can have a large impact on the pressure response of the reservoir.

This is mentioned because for the simulation runs analyzed in this work, the endpoint of both the initial and secondary depletions is determined by average reservoir pressure. Therefore, as is illustrated below, the simulation time of the runs with and without confinement are not equal. To allow comparison, Table 6.1 below summarizes the start and end time of each portion of the two simulation runs along with the molar amounts of hydrocarbons produced at each time. The bottom row in the table is included to show the molar amount of gas injected in each case. Table 6.2 displays the lbmols injected in terms of standard volume and reservoir pore volumes.

Table 6.1: Simulation Time and Molar Production for Runs with and without Confinement Effects

Portion of Simulation Run	Simulation Time (days)		Hydrocarbons Produced (lbmol)	
	Confine On	Confine Off	Confine On	Confine Off
Start of Initial Depletion	0	0	0	0
End of Initial Depletion=Start of Injection	160.4	243.1	29429	34936
End of Injection=Start of 2nd Depletion	228.4	293.1	29429	34936
End of 2nd Depletion	529.5	617.9	97159	99098
CO_2 Injection	-	-	58030	57914

Table 6.2: Volumes of CO_2 Injected for Runs with and without Confinement

CO_2 Injection Amount	Confine On	Confine Off
Volume Injected at Standard Conditions (Mscf)	21897	21853
Pore Volumes Injected	0.558	0.557

6.1.1 Field Production and Properties

This section compares the production results for the entire reservoir. Table 6.3 below compares total molar production for each component, for each portion of the simulation run, with and without confinement effects. The depletion recoveries are calculated per

Eq. 5.1 (initial depletion), Eq. 5.2 (injection) and Eq. 5.3 (total recovery). The rightmost column indicates the total molar recovery for all components combined.

Table 6.3: Comparison of Fluid Component Molar Recovery for each Portion of the Simulation Run

Component	C1	C2	C3	N2	CO2	Pseudo 1	Pseudo 2	Pseudo 3	Pseudo 4	Total
	Initial Depletion Recovery (%)									
Confine On	20.0	16.3	14.4	23.1	16.9	12.8	11.6	11.2	11.2	15.5
Confine Off	25.4	19.8	16.9	30.0	20.8	14.3	12.2	11.6	11.6	18.4
Difference	-5.5	-3.5	-2.4	-7.0	-3.8	-1.4	-0.6	-0.4	-0.4	-2.9
	Injection Recovery (%)									
Confine On	44.7	42.3	41.1	47.9	2.2	40.1	39.2	39.0	39.0	30.9
Confine Off	45.9	41.9	40.0	50.5	2.4	38.3	37.0	36.6	36.6	30.5
Difference	-1.2	0.4	1.1	-2.6	-0.2	1.8	2.3	2.4	2.4	0.4
	Total Recovery (%)									
Confine On	55.8	51.7	49.6	59.9	2.7	47.7	46.3	45.8	45.8	39.1
Confine Off	59.7	53.4	50.1	65.3	3.0	47.1	44.7	43.9	43.9	40.3
Difference	-3.9	-1.7	-0.5	-5.5	-0.3	0.7	1.6	1.9	1.9	-1.1

With confinement on, the recovery of the lighter components is smaller than the recovery with confinement effects off. These light components are concentrated in the vapor phase. The opposite trend is true for the heavier pseudo-components in the fluid. Confinement results in higher recovery of these heavy pseudo-components which tend to concentrate in the liquid phase. This difference in distribution of the components, resulting from confinement, determines the recovery of each component and the impact on production seen in the plots below.

Figure 6.1 below compares total oil production while Figure 6.2 compares gas production as a function of simulation time. In Figure 6.1, the start and end injection time for each case is explicitly marked to draw attention to the fact that no production occurs during the injection and the curve remains flat. It also shows that the injection time for the two cases is not equal. Subsequent figures lack these explicit lines but the same behavior is occurring.

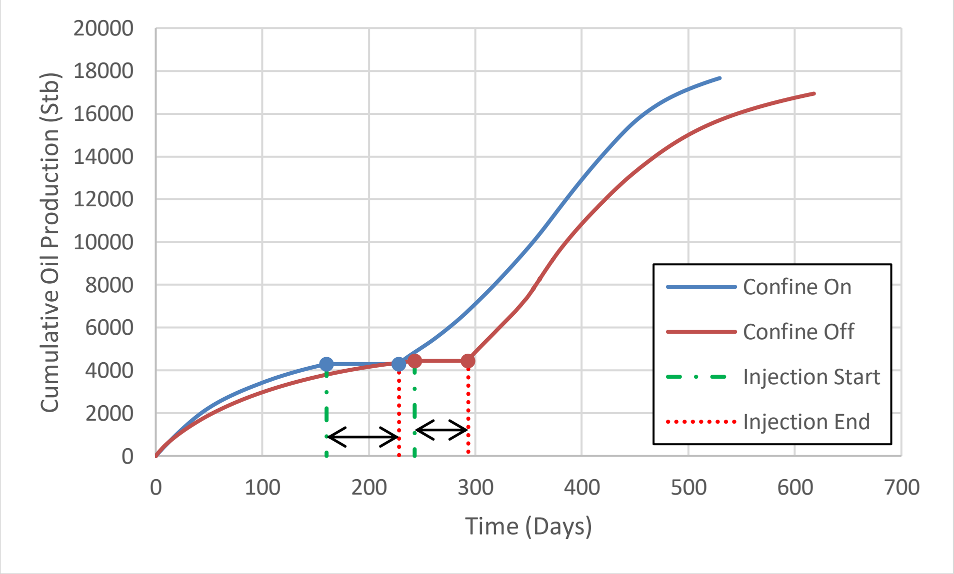

Figure 6.1: Comparison of confinement effects on field oil production in stock tank barrels. The entire simulation run includes an initial depletion, CO_2 injection and a secondary depletion. The round dots indicate the transition from one portion of the simulation run to the next. During injection (between the two dots) the curves are flat because no production is occurring at this time. The length of the injection time between the two runs is different, however, approximately the same molar amount of gas is injected in both runs.

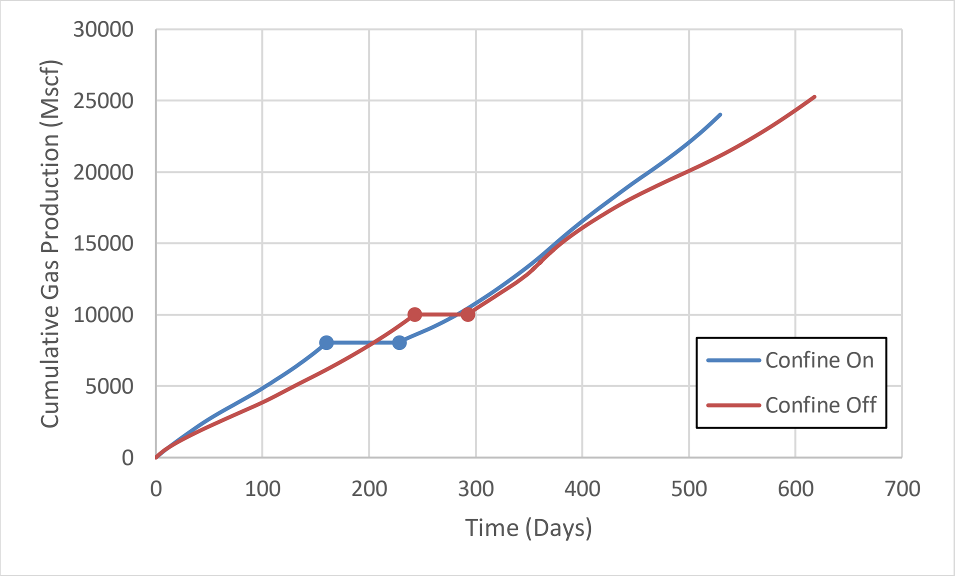

Figure 6.2: Comparison of confinement effects on field gas production in thousands of standard cubic feet. Each plot contains two dots which mark the transition from initial depletion to injection and from injection to secondary depletion. The run with confinement effects enabled results in lower overall gas production.

For the initial depletion, the runs with and without confinement produce a similar amount of oil. At the same time, the run without confinement effects produces a larger amount of gas. Looking at the full simulation time, the run with confinement effects produces a greater amount of oil and a smaller amount of gas than the run without confinement effects. It may be difficult to see the effects of confinement when looking at total oil and gas production because the two runs produce different total amounts of hydrocarbons. Figure 6.3 helps to isolate the impact of confinement effects by showing how the instantaneous producing Gas-Oil Ratio (GOR) changes with time for both simulation runs.

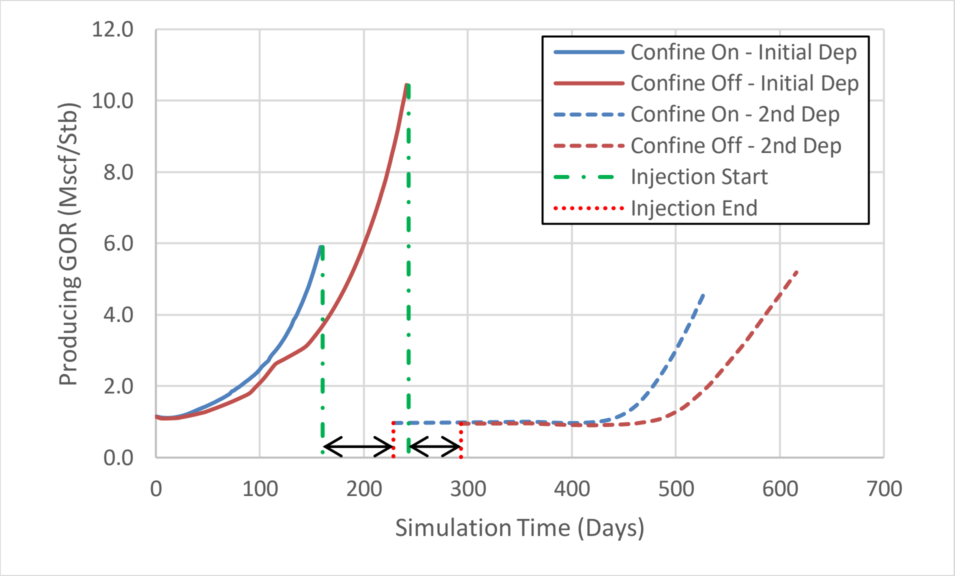

Figure 6.3: Instantaneous producing gas-oil ratio for runs with and without confinement effects. The two sets of lines correspond to the initial depletion and secondary depletion. The injection portion of the run occurs during the time separating the two sets of plots. No production occurs during the gas injection, therefore, there is no GOR for this portion of the simulation run. For both runs, the same molar amount of gas is injected. The secondary depletion starts after this full amount of gas is injected.

The plot of producing GOR clearly shows the impact of confinement on production characteristics. For the initial depletion indicated by a solid line, both plots start at the same GOR because the initial reservoir pressure is above the saturation pressure for the black oil and single phase production occurs initially. As pressure drops below the saturation pressure, both runs see an increase in GOR indicating two phase production. At the end of the initial depletion, the GOR with confinement is lower than for the run without confinement considered. The lower GOR occurs because confinement effects in small pores increase oil saturation which results in higher oil relative permeability and lower gas relative permeability as compared to the run without confinement.

The space separating the two sets of curves indicates the gas injection portion of the run. The second set of dashed curves indicate the secondary depletion results. After the CO_2 injection is complete, there is a large decrease in producing GOR for both runs. The injection of CO_2 increases the pressure in the reservoir to the point that the cells near the producing fracture become single phase oil again. Single phase production causes the flat portion of the GOR plot at the start of secondary depletion seen in Figure 6.3. As two phase production begins again, the GOR begins increasing. The final GOR with confinement effects is lower than for the run without confinement effects. Again, this results from the tendency of confinement effects to increase oil saturation.

Confinement can also have an impact on the pressure response of the reservoir. Figure 6.4 below shows the average pressure of the reservoir as a function of total molar hydrocarbon production.

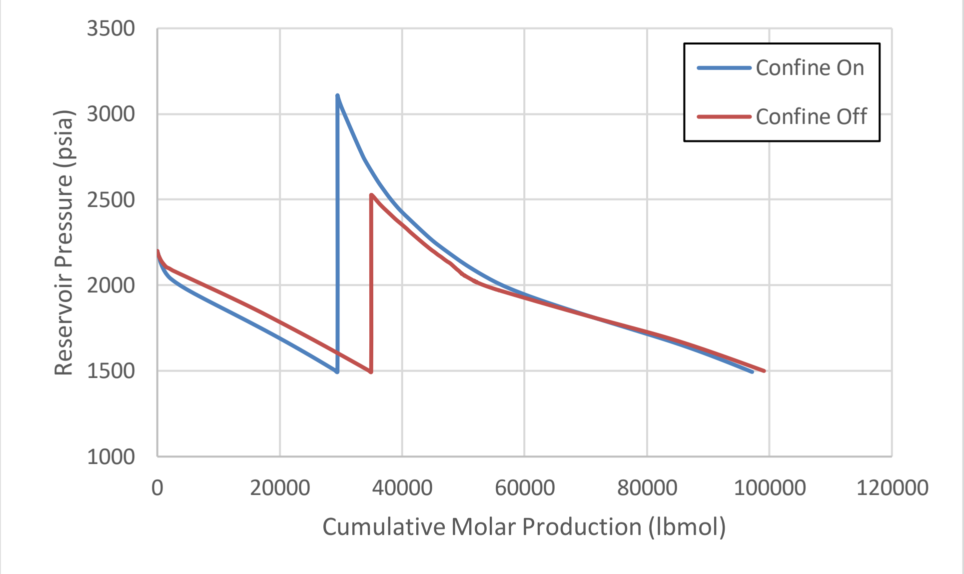

Figure 6.4: Average reservoir pressure as function of hydrocarbon production. The reservoir pressure with and without confinement effects is compared. No production occurs during the injection portion of the run, therefore, the entire injection is represented as a vertical line.

In the figure above, both simulations start with an equal number of lbmols of hydrocarbons in the reservoir and at the same pressure. With confinement effects on, the average reservoir pressure decreases more for each lbmol of hydrocarbon production during the initial depletion. As a result, fewer lbmols of hydrocarbons are produced before the average reservoir pressure reaches 1500 psia and the initial depletion terminates.

For the gas injection portion of the run, the same molar amount of CO_2 is injected in each of the two runs. The spike in the pressure plots in Figure 6.4 indicates the pressure increase due to injection. With confinement on, the pressure increase is much larger than for the run without confinement. This difference arises from the fact that at the end of initial depletion, the reservoir with confinement on contains more lbmols of hydrocarbons than the reservoir with confinement off. Since both runs inject the same amount of CO_2, at the end of injection, the reservoir with confinement contains more mass than the reservoir without confinement. The larger mass results in the larger pressure increase seen. The pressures begin to decline again during the secondary depletion. For both runs, the simulation terminates when the average reservoir pressure reaches 1500 psia.

6.1.2 Fluid Properties in Individual Cells

This section presents results showing the effect of confinement on fluid properties in individual cells in the reservoir model. The reservoir model dimensions and number of cells match those shown in Figure 4.7. Four cells with a representative range of pore sizes are examined from the run with confinement. Figure 6.5 shows the position of each cell along with the corresponding pore size assigned to the cell. The cells selected for analysis are located in the same row and are in contact with the producing fracture. As a result, each cell experiences approximately the same pressures and contains the approximately the same fluid composition.

The results for the confined cells are compared against the results for Cell 1 from the simulation without confinement. Only one cell is examined for the no confinement case because the results for Cells 261, 771 and 1311 are almost identical to those for Cell 1 so including them would be unnecessarily repetitive. The cells numbers correspond to the cell numbers assigned to the model by the simulator. The cells are numbered by iterating along the X-axis first, then along the Y-axis and finally along the Z-axis (increasing depth).

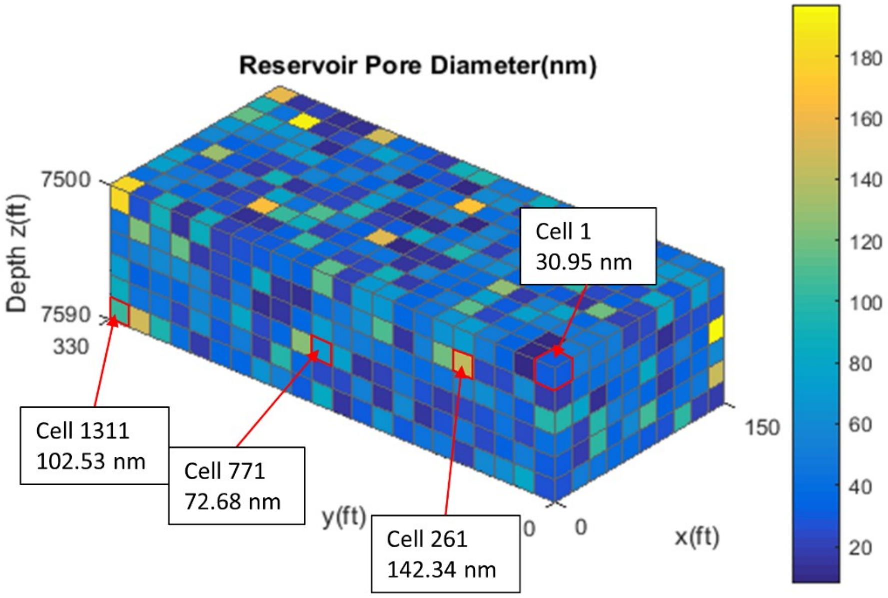

Figure 6.5: Positions and pore sizes for cells analyzed from a simulation run with confinement. The results for the cell in position 1 for the no confinement case are also analyzed.

Figure 6.6 below shows the oil phase density as a function of pressure for each cell during the initial depletion portion of the run.

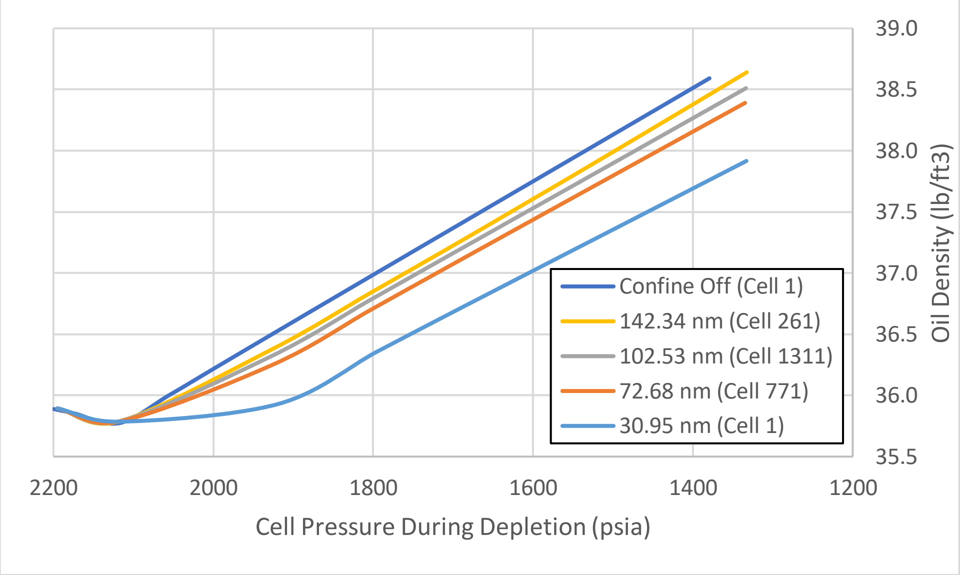

Figure 6.6: Oil phase density as a function of cell pressure during initial depletion. Results for four cells under confinement are shown along with a single cell without confinement effects.

The results for oil density follow a trend where density decreases for decreasing pore size. The result without confinement shows the highest density of all the results. The gas phase density for the same cells during initial depletion are shown in Figure 6.7.

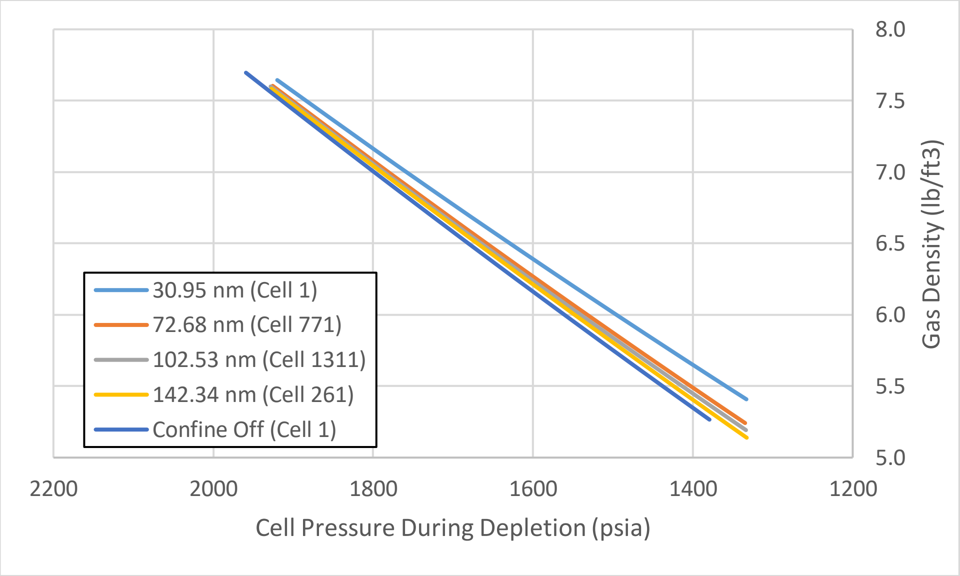

Figure 6.7: Gas phase density as a function of cell pressure during initial depletion.

The gas phase density results show the oppose trend of the oil density results. The gas phase density increases with decreasing pore size. The cell without confinement effects has the lowest gas density.

Figure 6.8 below shows the oil density for the same set of cells during the CO_2 injection portion of the run. Figure 6.9 shows the oil density during the secondary depletion. It is noted that for the simulation run without confinement, the reservoir pressure increases less during the injection portion of the simulation run. For comparison, at the end of injection, with confinement on, the pressure in Cell 1 is 3075 psia while without confinement the pressure in Cell 1 is 2417 psia.

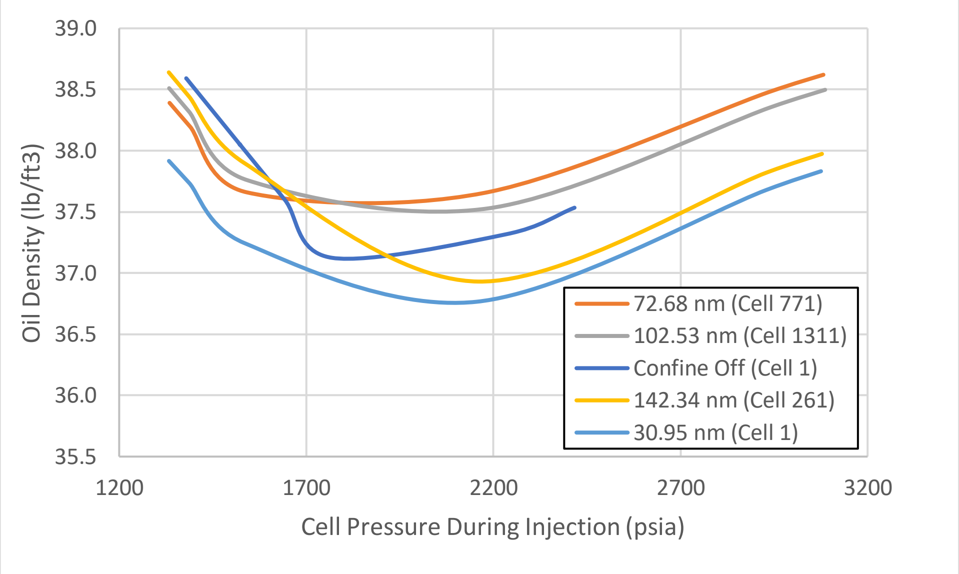

Figure 6.8: Oil phase density as a function of cell pressure during injection.

The density results in Figure 6.8 continue from the initial depletion results in Figure 6.6. As the injection progresses and the pressure increases, the trend in oil densities changes. At the end of injection the trend is no longer a function of pore size. This occurs because by the end of injection, the pressure in the cells exceeds the saturation pressure and the cells become single phase oil again. Table 6.4 shows the overall molar composition of methane in each cell at the end of the injection portion of the run when all cells are fully oil saturated.

Table 6.4: Final Total Molar Composition of Methane in Cells at the End of Gas Injection

Cell No.	Pore Size (nm)	Total Molar C_1 Composition (%)
771	72.68	31.0
1311	102.53	31.2
1	Confine Off	31.8
261	142.34	32.5
1	30.95	33.6

The final trend in density in Figure 6.8 matches the total molar composition of C_1 in the cells. The cells containing a higher concentration of C_1 have a lower oil density.

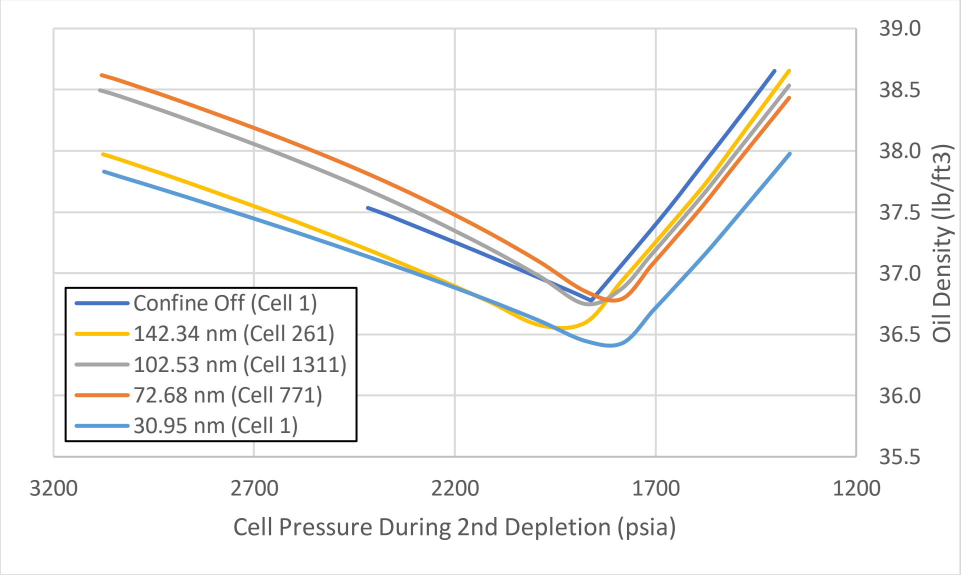

Figure 6.9: Oil phase density as a function of cell pressure during secondary depletion.

During secondary depletion, the density trend initially matches the final trend from the injection (Figure 6.8). As the pressure in the cells decreases past the saturation pressure, the cells enter two phase flow again and the trend changes. The final oil density trend at the end of the secondary depletion once again matches the order of pore sizes with the smallest pore size corresponding to the lowest oil density.

6.2 Volatile Oil Simulation Results

The effect of confinement is examined for a different reservoir fluid composition in this section. Reservoir simulations are run using the Eagle Ford volatile oil from Table A.2 in Appendix A with C_1 as the injection gas and the same pore size distribution. As in the previous section, the simulation is run once with confinement effects and again without confinement effects considered and the results are compared. It is important to note that the volatile oil is a near critical fluid and as a result the confinement effects are diminished. Generally speaking, for near critical fluids, the interfacial tension between the oil and gas phases is low and therefore capillary effects are minimized. Figure 6.10 below shows the phase diagram for the starting fluid composition and indicates the pressure range and temperature for the initial depletion.

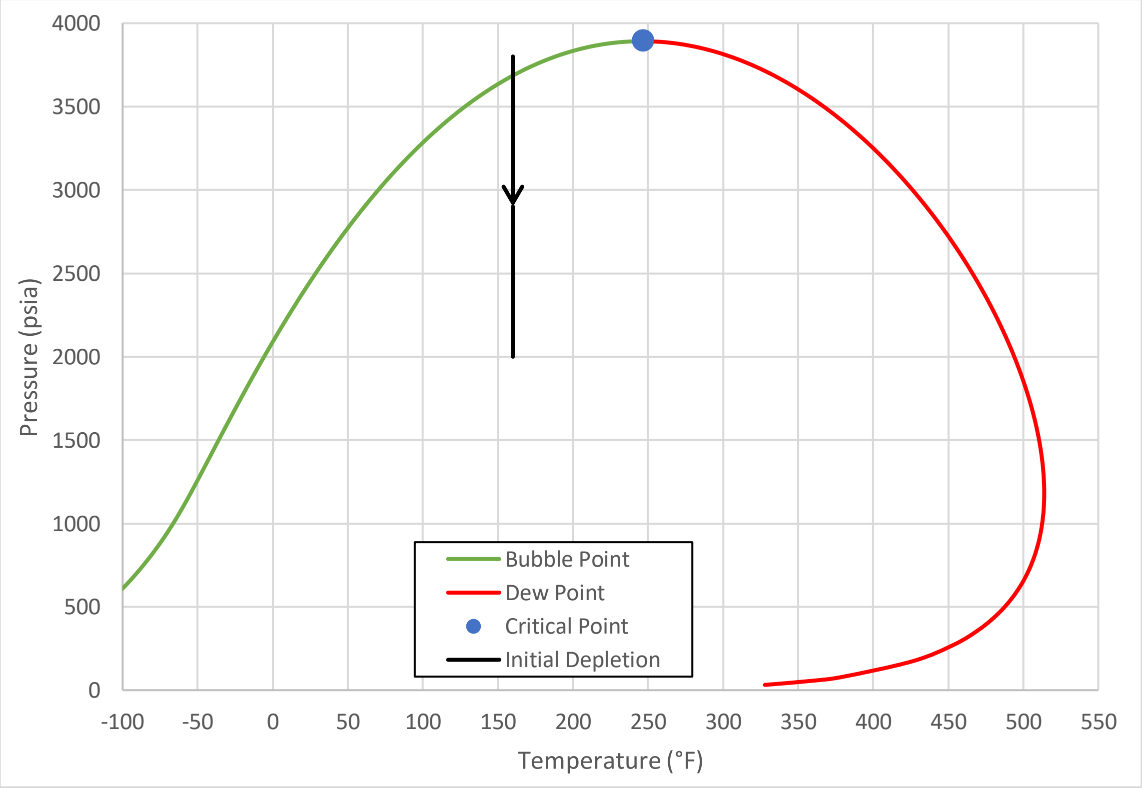

Figure 6.10: Phase Diagram for Eagle Ford Volatile Oil with the Reservoir Simulation Temperature and Pressure Range Indicated on the Diagram.

For reference Table 6.5 provides the start and end time for each portion of the simulation run along with the hydrocarbon production corresponding to each time. The bottom row shows the molar amount of C_1 injected. Table 6.6 shows the corresponding injected volumes.

Table 6.5: Simulation Time and Molar Production for Reservoir Simulation Runs for Eagle Ford Volatile Oil

Portion of Simulation Run	Simulation Time (days)		Hydrocarbons Produced (lbmol)	
	Confine On	Confine Off	Confine On	Confine Off
Start of Initial Depletion	0	0	0	0
End of Initial Depletion=Start of Injection	181.6	210.6	95902	103080
End of Injection=Start of 2nd Depletion	216.6	298.1	95902	103080
End of 2nd Depletion	329.7	444.2	184845	197202
C_1 Injection	-	-	84394	83092

Table 6.6: Volumes of C_1 Injected for Runs with and without Confinement

C_1 Injection Amount	Confine On	Confine Off
Volume Injected at Standard Conditions (Mscf)	31964	31471
Pore Volumes Injected	0.657	0.647

6.2.1 Field Production and Properties for Volatile Oil

This section examines the effect of confinement on field production values. The total molar recovery for each component for each portion of the simulation run is summarized in Table 6.7 below.

Table 6.7: Fluid Component Recovery for each Portion of the Simulation Runs for Volatile Oil

Component	C1	C2	C3	nC4	iC4	nC5	iC5	C6	N2	CO2	C7+	Total
	Initial Depletion Recovery (%)											
Confine On	40.4	34.0	29.2	24.4	26.0	20.3	21.3	17.0	44.1	34.9	5.3	35.1
Confine Off	43.3	36.8	31.8	26.8	28.4	22.3	23.4	18.7	46.9	37.7	5.8	37.7
Difference	-2.9	-2.8	-2.6	-2.4	-2.4	-2.0	-2.1	-1.7	-2.8	-2.8	-0.5	-2.6
	Injection Recovery (%)											
Confine On	35.6	46.7	37.4	29.1	31.7	22.5	24.0	17.7	75.4	48.5	3.4	9.5
Confine Off	38.9	51.9	41.8	32.5	35.5	25.1	26.8	19.7	82.4	53.7	3.8	13.7
Difference	-3.3	-5.2	-4.4	-3.4	-3.8	-2.6	-2.8	-2.0	-7.0	-5.2	-0.4	-4.2
	Total Recovery (%)											
Confine On	53.3	64.8	55.7	46.4	49.5	38.2	40.2	31.7	86.2	66.5	8.5	51.6
Confine Off	57.0	69.6	60.3	50.6	53.8	41.8	43.9	34.7	90.7	71.2	9.3	55.3
Difference	-3.7	-4.8	-4.6	-4.2	-4.3	-3.6	-3.7	-3.0	-4.5	-4.7	-0.8	-3.7

For the simulation runs in this section, the injection gas is methane (C_1). The run with confinement effects has lower recovery of all components compared to the run without confinement. Figures 6.11 and 6.12 below show the field production of oil and gas respectively during the full simulation run.

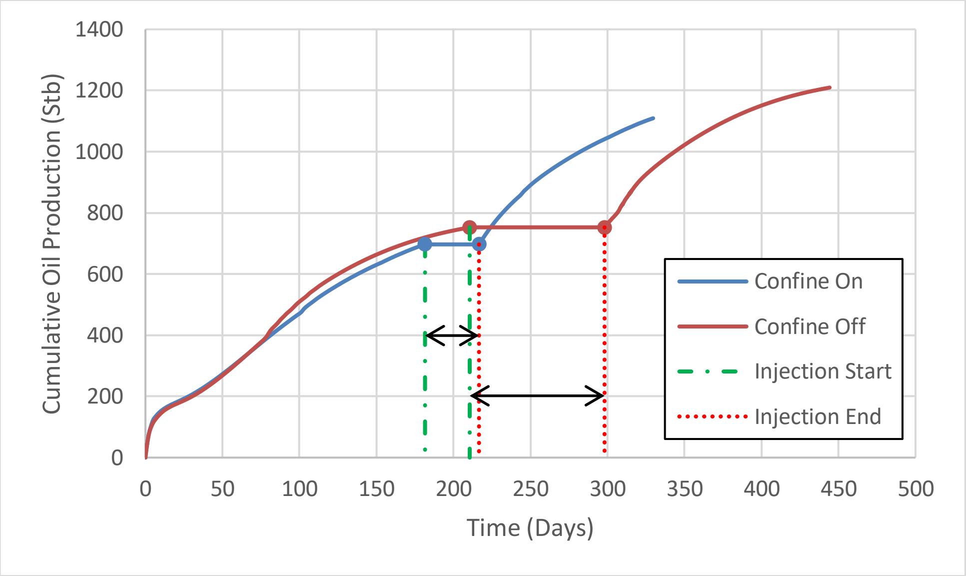

Figure 6.11: Field oil production comparison for simulation runs with and without confinement effects. Each run consists of an initial depletion which starts at time zero and ends at the first dot, a C_1 injection which ends at the second dot and a secondary depletion.

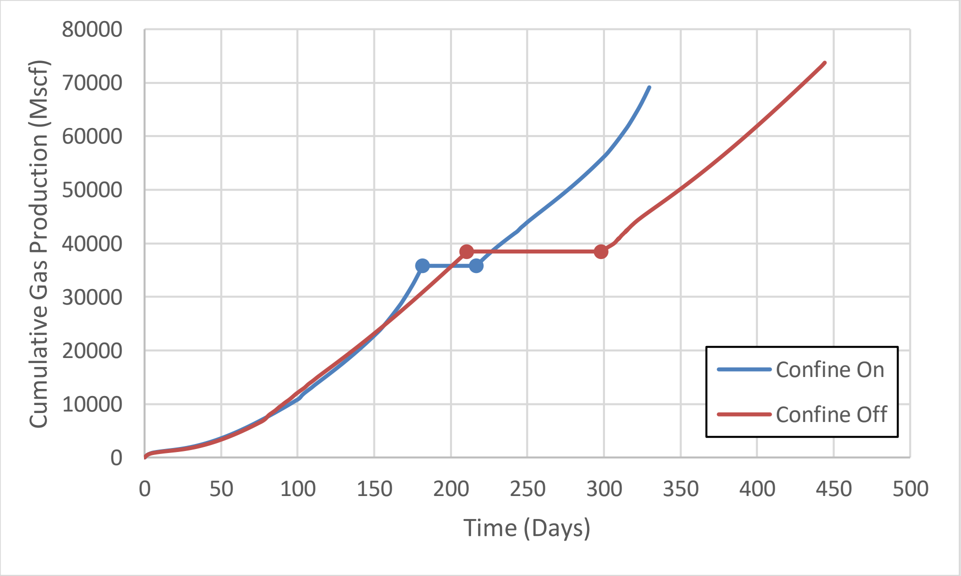

Figure 6.12: Field gas production comparison for simulation runs with and without confinement effects. Each run consists of an initial depletion which starts at time zero and ends at the first dot, a C_1 injection which ends at the second dot and a secondary depletion.

The simulation without confinement indicates higher production of both oil and gas during the initial depletion and also during the secondary depletion.

Reservoir pressure controls the end of the initial depletion and the secondary depletion. Figure 6.13 below shows the average reservoir pressure as a function of total molar production.

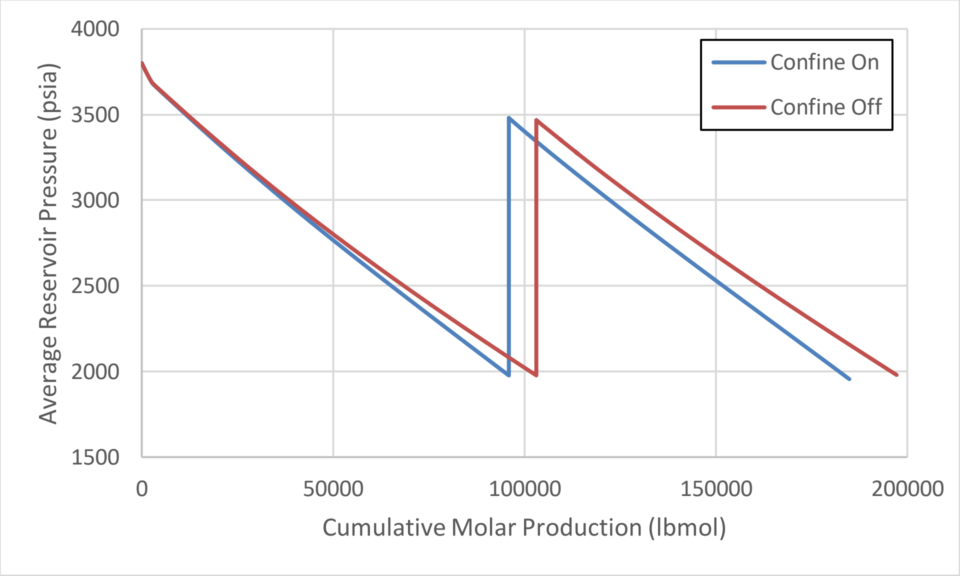

Figure 6.13: Average reservoir pressure as a function of hydrocarbon molar production for simulation runs with and without confinement effects.

The initial decrease in pressure corresponds to production that occurs during the initial depletion portion of the run. With confinement effects considered, the average reservoir pressure decreases more for each lbmol of hydrocarbon production. The vertical step increase in pressure corresponds to the gas injection portion of the simulation run. The second slope corresponds to the production occurring during the secondary depletion. The run with confinement effects included reaches the threshold pressure to end the simulation at a lower hydrocarbon production than the run without confinement effects. Overall, the confinement effects result in a lower hydrocarbon production. This is consistent with the oil and gas production shown in Figures 6.11 and 6.12, respectively.

To investigate the effect of confinement on ratio of oil and gas produced, Figure 6.14 below shows the cumulative produced Gas-Oil Ratio (GOR) for the simulation runs.

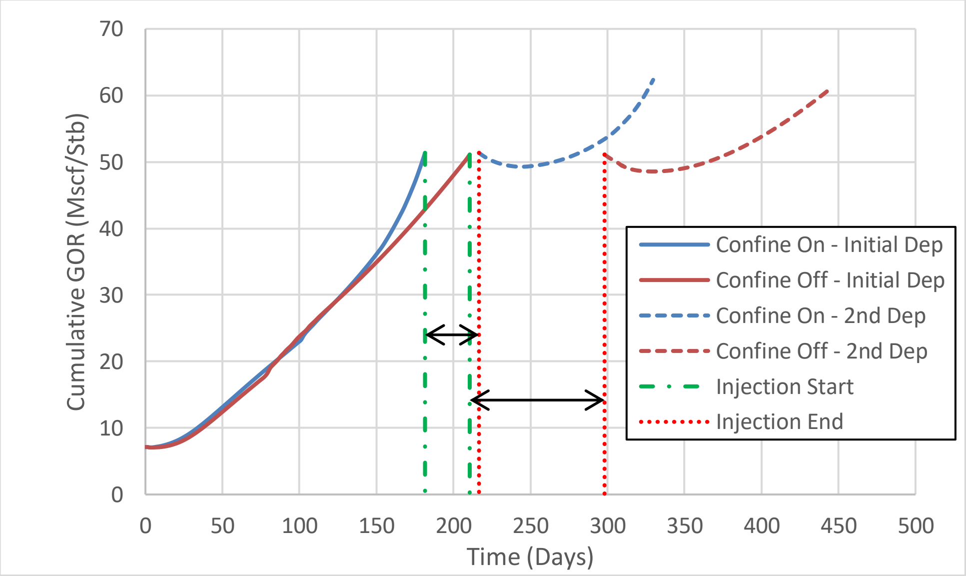

Figure 6.14: Cumulative produced gas-oil ratio for simulation runs with and without confinement effects considered. The two sets of lines correspond to the initial depletion (solid line) and the secondary depletion (dashed line). The injection portion of the run is not shown because no production occurs while gas is being injected. Injection occurs in the time between the end of the initial depletion curve and the start of the secondary depletion curve.

The ratio of total gas to oil produced is similar for both runs. This is true at the end of the initial depletion and also at the end of the entire simulation run. The time offset of the two sets of curves in Figure 6.14 is due to time differences between the two simulation runs.

For field production of the volatile oil, confinement effects reduce total hydrocarbon production but have a minimal impact on the ratio of gas to oil production. This is partially due to relative permeability values for the volatile oil (Figure 5.14). The oil relative permeability drops off very quickly and as result much of the oil production occurs from volatilized oil contained in the gas phase.

6.2.2 Fluid Properties for Individual Cells for Volatile Oil

This section looks at properties of individual cells during the reservoir simulation runs to illustrate the effect of confinement. Figure 6.15 below indicates the location of the cells examined in this section and the pore size assigned to each cell. Each figure also contains the results for Cell 11 from the simulation run without confinement effects.

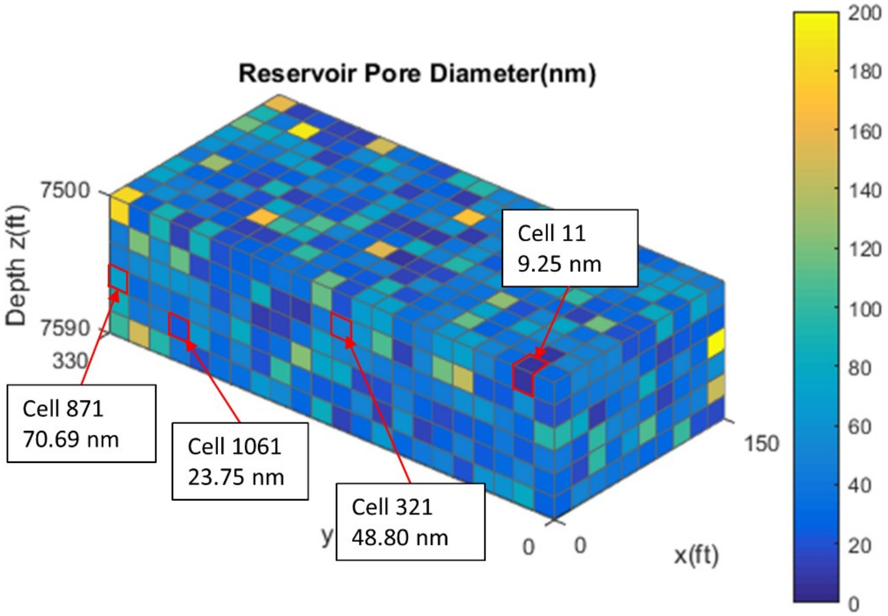

Figure 6.15: Cell locations and pore sizes analyzed during a confinement simulation run for volatile oil. Results for Cell 11 for the simulation without confinement are also analyzed.

The cells selected all contact the producing fracture face and cover a range of pore sizes. For the run with confinement off, all of the cells pictured show very similar behavior therefore only Cell 11 is included in each of the figures below to illustrate the unconfined behavior.

Figures 6.16 and 6.17 below show the oil and gas density, respectively, for each cell during the initial depletion.

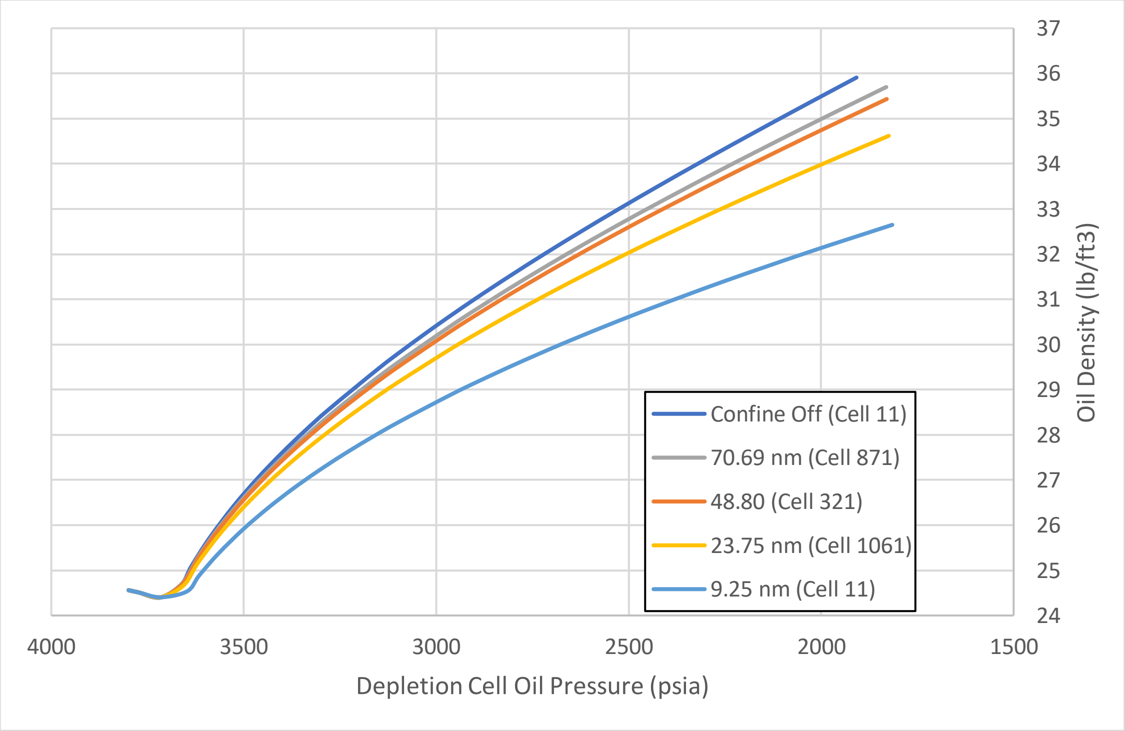

Figure 6.16: Oil phase density as a function of depletion pressure for four confined cells with different pore sizes and a single unconfined cell.

The depletion starts with single phase oil in all cells. Below the saturation pressure, the densities begin to vary from one another. As the pressure decreases further, the difference in density between pore sizes increases further. The unconfined cell has the highest oil density and density decreases for progressively smaller pore sizes.

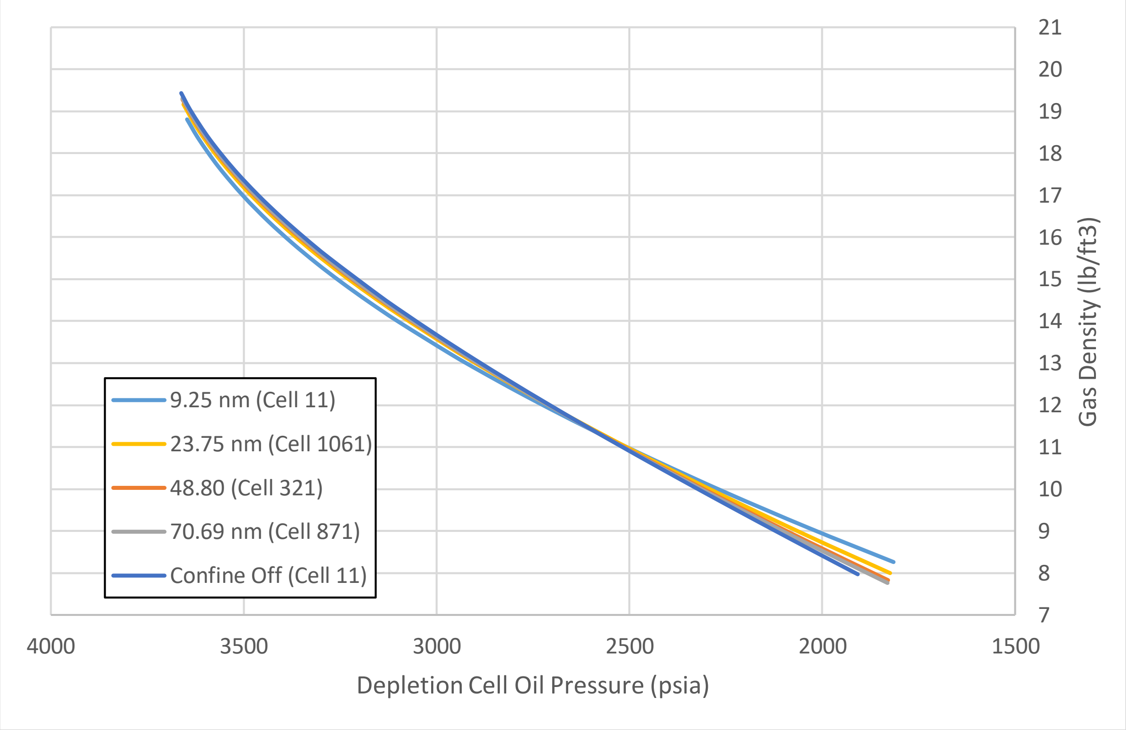

Figure 6.17: Gas phase density as a function of depletion pressure for four confined cells and a single unconfined cell.

As stated earlier, the cells are single phase oil and the gas phase does not appear until the cell pressure reduces below the saturation pressure. At high pressure, the gas phase density is very similar to that of the oil phase in Figure 6.16. This behavior is characteristic of a near critical reservoir. At high pressure, the gas phase density plots for all cells are very similar and do not vary much from one another until lower cell pressures. At the end of depletion, the gas density values for all cells lie within 1 lb/ft^3 of each other. The smallest pore size corresponds to the highest density gas. As the pore size increases, the final density is progressively lower. The lowest gas phase density corresponds to the cell without confinement.

The behavior seen in Figures 6.16 and 6.17 occurs because at smaller pore sizes, confinement effects tend to keep light components like methane in the liquid phase. This results in a lower liquid phase density and a higher gas phase density. Figure 6.18 shows the oil saturation of each cell during the initial depletion and is consistent with the behavior described above.

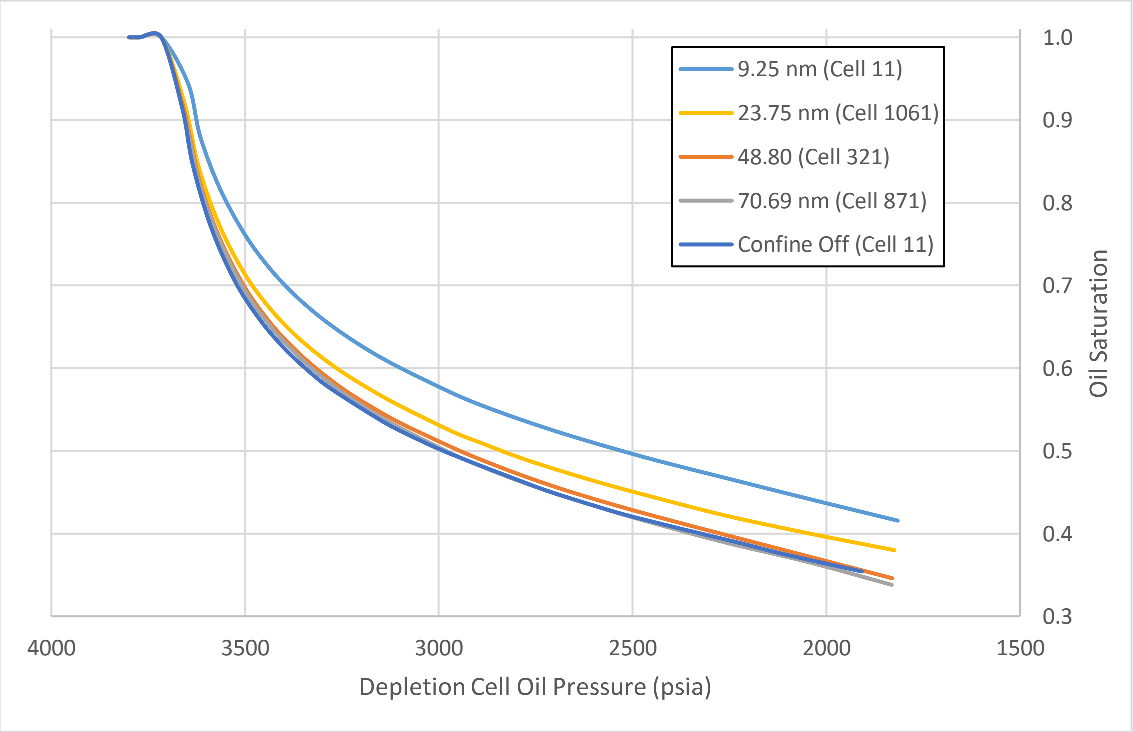

Figure 6.18: Oil saturation as a function of depletion pressure for four confined cells and a single unconfined cell.

For a given cell pressure, the cell with the smallest pore size has the highest oil saturation, while cells with larger pores have progressively lower oil saturations. The unconfined cell has the lowest oil saturation.

Figures 6.19 and 6.20 below show the oil density for the injection portion of the run and the secondary depletion respectively. These figures show a similar trend to the oil phase density during the initial depletion shown in Figure 6.16 above.

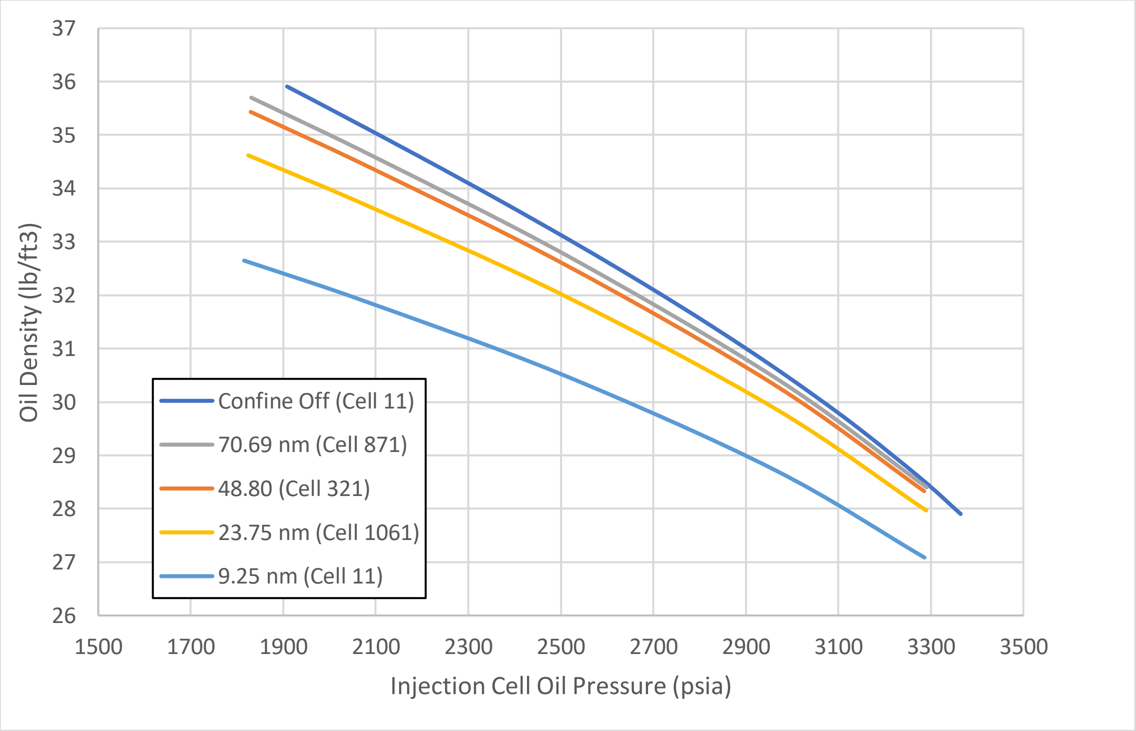

Figure 6.19: Oil phase density as a function of cell pressure for the injection portion of the simulation run.

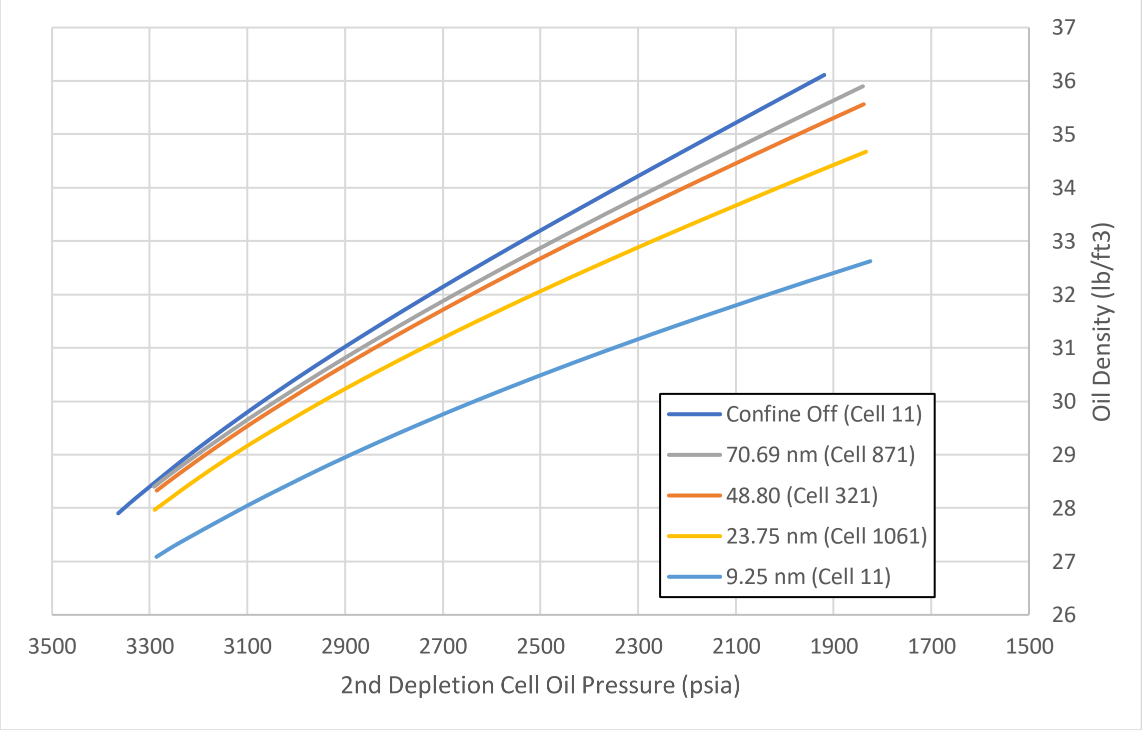

Figure 6.20: Oil phase density as a function of cell pressure for the secondary depletion portion of the simulation run.

The gas phase density and oil saturation for the injection and secondary depletion are not shown, however, they follow the same trend seen in Figure 6.17 for gas density and Figure 6.18 for oil saturation. Smaller pore sizes result in higher gas phase density and higher oil saturation for a given pressure. The unconfined cell had the lowest density gas and the lowest oil saturation of the cells examined.

7. CONCLUSIONS AND RECOMMENDATIONS FOR FUTURE WORK

The following conclusions are drawn based on the research presented in this thesis:

1) Inclusion of capillarity, via the Young-Laplace equation, into the calculation of phase equilibrium is a thermodynamically consistent method to account for confinement effects. This method requires only a modest increase in computational time over a normal flash calculation.
2) The mechanistic model presented in this work can be used with reasonable accuracy to produce capillary pressure curves and to calculate recovery factors for initial depletion of a tight reservoir.
3) The mechanistic model presented in this work should not be used for calculations of gas injection in tight reservoirs. The reason is because it does not account for the location of the injection source and therefore cannot account for the degree of mixing that occurs during injection and secondary recovery.
4) The capillary pressure results obtained from the mechanistic model can be used to determine a unique set of relative permeability curves for the pore size distribution, reservoir fluid and pressure range considered.
5) When using gas injection as an enhanced oil recovery technique, more efficient hydrocarbon recovery can be achieved by using separate fractures for gas injection and production.
6) Confinement effects in small pore sizes favor production of heavier components found in the liquid phase for black oil reservoirs. For near critical reservoirs, the impact of confinement effects on production are minimized.

The following recommendations are made for future work related to this topic:

1) Couple the mechanistic model with a production model to provide a time component to the recovery results.
2) Modify the mechanistic model to account for an initial transient production period.
3) For reservoir simulations involving gas injection, the simulations can be adjusted to include a soaking period between the gas injection and the secondary depletion.
4) Modify the reservoir simulator to include diffusion as a transport mechanism. This is especially important if the soaking period recommended above is included in the simulation runs.
5) Incorporate a relationship between pore size and absolute permeability to evaluate production for a heterogeneous reservoir.

REFERENCES

Addison, V. 2016. EOG Shifts Drilling Strategy, Pushes EOR. *EP Mag*, May 6, 2016, https://www.epmag.com/eog-shifts-drilling-strategy-pushes-eor-847741#p=full (accessed September 22, 2017).

Alkan, H. and Luan, G. 1993. Estimation of Parachors from Critical Properties. SPE-27633-MS

Australian School of Petroleum: The University of Adelaide. 2014. Mercury Injection Capillary Pressure Analysis (April 17, 2014), http://www.asp.adelaide.edu.au/research/micp-page/ (accessed October 2, 2016).

Clayperon, E. 1834. Memoire Sur La Puissance Motrice de la Chaleur (Memoir on the Motive Power of Heat). *Journal de l'Ecole Royale Polytechnique* **14**(23): 153-190.

Didar, B.R. and Akkutlu, I.Y. 2015. Confinement Effects on Hydrocarbon Mixture Phase Behavior in Organic Nanopore. Unconventional Resources Technology Conference, San Antonio, Texas, July 20-22, 2015. URTEC-2151854 /SPE-178519-MS.

Energy Information Administration (EIA). 2017. Today In Energy: Tight oil expected to make up most of US oil production increase through 2040 (Updated February 22, 2017), https://www.eia.gov/todayinenergy/detail.php?id=29932 (accessed December 11, 2017).

Firincioglu, T., Ozkan, E., and Ozgen, C. 2012. Thermodynamics of Multiphase Flow in Unconventional Liquids-Rich Reservoirs. SPE Annual Technical Conference and Exhibition, San Antonio, Texas, October 8-10, 2012. SPE-159869-MS. DOI: 10.2118/159869-MS.

Firoozabadi, A. 1999. *Thermodynamics of Hydrocarbon Reservoirs*, 1st Edition, Chapter 4, 209-293. New York, NY: McGraw-Hill Education.

Fragoso, A., Wang, Y., Jing, G. et al. 2015. Improving Recovery of Liquids from Shales through Gas Recycling and Dry Gas Injection. SPE Latin American and Caribbean Petroleum Engineering Conference, Quito, Ecuador, November 18-20, 2015. SPE-177278-MS. DOI: 10.2118/177278-MS.

Gauss, F.C. 1830. *Principia Generalia Theoriae Figurae Fluidorum in Statu Aequilibrii*, Original Edition. Gottingen, Germany: Sumtibus Dieterichianis

Gong, X., Tian, Y., McVay, D.A. et al. 2013. Assessment of Eagle Ford Shale Oil and Gas Resources. SPE Unconventional Resources Conference, Calgary, Alberta, Canada, November 5-7, 2013. SPE-167241-MS. DOI: 10.2118/167241-MS.

Gonzalez Abad, K.G. 2016. *Adaptive Mesh Refinement and Coarsening for Compositional Reservoir Simulation*. PhD Dissertation, Texas A&M University, College Station, Texas (August 2016).

Haider, B.A. 2015. *Impact of Capillary Pressure and Critical Properties Shift Due to Confinement on Hydrocarbon Production from Shale Reservoirs.* MS Thesis, Stanford University, Department of Energy Resources, Stanford, California (August 2015).

Hauksbee, F. 1710. An Account of an Experiment Touching the Ascent of Water between Two Glass Planes, in an Hyperbolick Figure. *Philosophical Transactions of the Royal Society of London* 27: 539-540

Honarpour, M.M., Nagarajan, N.R., Orangi, A. et al. 2012. Characterization of Critical Fluid, Rock, and Rock-Fluid Properties-Impact on Reservoir Performance of Liquid-rich Shales. SPE Annual Technical Conference and Exhibition, San Antonio, Texas, October 8-10, 2012. SPE-158042-MS. DOI: 10.2118/158042-MS.

Jacobs, T. 2014. The Shale Evolution: Zipper Fracture Takes Hold. *Journal of Petroleum Technology* 66(10): 60-67. http://dx.doi.org.ezproxy.library.tamu.edu/10.2118/1014-0060-JPT

Jin, L., Ma, Y. and Jamili, A. 2013. Investigating the Effect of Pore Proximity on Phase Behavior and Fluid Properties in Shale Formations. SPE Annual Technical Conference and Exhibition, New Orleans, Louisiana, September 30-October 2, 2013. SPE-166192-MS. DOI: 10.2118/166192-MS.

Kalla, S., Leonardi, S.A., Berry D.W. et. al. 2015. Factors That Affect Gas-Condensate Relative Permeability. *SPE Reservoir Evaluation & Engineering* 18(01): 5-10. https://doi.org/10.2118/173177-PA

Laplace, P.S. (1805). *Supplement Au Dixieme Livre Du Traite De Mecanique Celeste. Sur L'Action Capillaire*, Original Edition.Volume 4. Paris, France

Leverett, M.C. (1941). Capillary Behavior in Porous Solids. *Transaction of the AIME* 142(1): 152-169. http://dx.doi.org.ezproxy.library.tamu.edu/10.2118/941152-G

Loucks, R.G., Reed, R.M., Ruppel, S.C., et. al. 2009. Morphology, Genesis, and Distribution of Nanometer-Scale Pores in Siliceous Mudstones of the Mississippian Barnett Shale. *Journal of Sedimentary Research* 79: 848-861. http://dx.doi.org/10.2110/jsr.2009.092

Lohrenz, J., Bray, B.G., and Clark, C.R. 1964. Calculating Viscosities of Reservoir Fluids from Their Compositions. Paper presented at the SPE Annual Fall Meeting, Houston. Society of Petroleum Engineers. DOI: http://dx.doi.org/10.2118/915-PA.

Luo, S., Nasbrabadi, H. and Lutkenhaus, J.L. 2016. Effect of Confinement on the Bubble Points of Hydrocarbons in Nanoporous Media. *AIChE Journal* 62(5): 1772-1780. http://dx.doi.org/10.1002/aic.15154

Michelsen, M.L. 1982. The Isothermal Flash Problem. Part II. Phase-Split Calculation. *Fluid Phase Equilibria* 9(1): 21-40. http://dx.doi.org/10.1016/0378-3812(82)85002-4

Miqueu, C., Mendibourne, B., Graciaa, A, et al. 2003. Modeling of the Surface Tension of Pure Components with the Gradient Theory of Fluid Interfaces: A Simple and Accurate Expression for the Influence Parameters. Fluid Phase Equilibria 207(1-2): 225-246. https://doi.org/10.1016/S0378-3812(03)00028-1

Mosbacher, R.A., Bailey, R.E., and Nichols, M.W. 1984. Enhanced Oil Recovery. National Petroleum Council, Washington, D.C.

Nakornthap, K. and Evans, R.D. 1986. Temperature-Dependent Relative Permeability and Its Effect on Oil Displacement by Thermal Methods. *SPE Reservoir Engineering* 1(3): 230-242. DOI: 10.2118/11217-PA

Nelson, P.H., 2009. Pore-throat Sizes in Sandstones, Tight Sandstones, and Shales. *American Association of Petroleum Geologists Bulletin* 93(3): 329-340. http://dx.doi.org/10.1306/10240808059

Peneloux, A., Rauzy, E. and Freze, R. 1982. A Consistent Correction for Redlich-Kwong-Soave Volumes. *Fluid Phase Equilibria* 8(1): 17-23. http://dx.doi.org/10.1016/0378-3812(82)80002-2

Peng, D.Y. and Robinson, D.B. 1976. A New Two-Constant Equation of State. *Industrial & Engineering Chemistry Fundamentals* 15(1): 59-64. http://dx.doi.org/10.1021/i160057a011

Pommer, M.E. 2014. Quantitative Assessment of Pore Types and Pore Size Distribution Across Thermal Maturity, Eagle Ford Formation, South Texas. MS Thesis, University of Texas, Austin, Texas (August 2014)

Purcell, W.R. 1949. Capillary Pressures – Their Measurement Using Mercury and the Calculation of Permeability Therefrom. *Journal of Petroleum Technology* 1(2): 39-48. http://dx.doi.org.ezproxy.library.tamu.edu/10.2118/949039-G

Quayle, O.R. 1953. The Parachors of Organic Compounds. An Interpretation and Catalogue. *Chemical Reviews* 53(3): 439-589.

Rachford Jr., H.H. and Rice, J.D. 1952. Procedure for Use of Electronic Digital Computers in Calculating Flash Vaporization Hydrocarbon Equilibrium. Journal of Petroleum Technology 4(10): 327-328. https://doi.org/10.2118/952327-G

Ramirez, J.F. and Aguilera, R. 2016. Factors Controlling Fluid Migration and Distribution in the Eagle Ford Shale. *SPE Reservoir Evaluation & Engineering* 19(03): 403-414. https://doi.org/10.2118/171626-PA

Redlich,O. and Kwong, J.N.S. 1949. On the Thermodynamics of Solutions. V. An Equations of State. Fugacities of Gaseous Solutions. *Chemical Reviews* 44 (1): 233-244. http://dx.doi.org/10.1021/cr60137a013

Riazi, M.R. and Daubert, T.E. 1987. Characterization Parameters for Petroleum Fractions. *Industrial & Engineering Chemistry* **26**(4): 755-759.

Sanaei, A., Jamili, A., and Callard, J. 2014. Effect of Pore Size Distribution and Connectivity on Phase Behavior and Gas Condensate Production from Unconventional Resources. SPE Unconventional Resources Conference, The Woodlands, Texas, April 1-3, 2014. SPE-168970-MS. DOI: 10.2118/168970-MS.

Stimpson, B.C. and Barrufet, M.A. 2017. Constructing Oil/Gas Capillary Pressure and Relative Permeability Curves From a Distribution of Pores in Shale Reservoirs. Unconventional Resources Technology Conference, Austin, Texas, July 24-26, 2017. URTeC-2670123-MS. DOI: 10.15530-urtec-2017-2670123.

Stimpson, B.C. 2017. *Impacts of Confined Space on Production from Tight Reservoirs*. MS Thesis, Texas A&M University, College Station, Texas (January 2017).

Stimpson, B.C. and Barrufet, M.A. 2016. Effect of Confined Space on Production from Tight Reservoirs. SPE Annual Technical Conference and Exhibition, Dubai, UAE, September 26-28, 2016. SPE-181686-MS. DOI: 10.2118/181686-MS.

Soave, G. 1972. Equilibrium constants from a modified Redlich-Kwong equation of state. *Chemical Engineering Science* 27(6): 1197-1203. http://dx.doi.org/10.1016/0009-2509(72)80096-4

Sugden, S.S. *The Parachor and Valency*. 1930. 1st Ed. London. G Routledge

Tovar, F.D., Eide, O., Graue, A., et al. 2014. Experimental Investigation of Enhanced Recovery in Unconventional Liquid Reservoirs using CO_2: A Look Ahead to the Future of Unconventional EOR. SPE Unconventional Resources Conference, The Woodlands, Texas, April 1-3, 2014. SPE-169022-MS. DOI: 10.2118/169022-MS.

Van der Waals, J.D. 1873. *De Continuiteit Van Den Gas-En Vloeiistoftoestand (on the continuity of the gas and liquid state).* Ph.D. Dissertation. Leiden, The Netherlands

Weinaug, C.F. and Katz, D.L. 1943. Surface Tension of Methane-Propane Mixtures. *Industrial & Engineering Chemistry* 35(2): 239-246.

Wilson, G.M. 1969. A Modified Redlich-Kwong Equation of State, Application to General Physical Data Calculation. Paper No.15C. Presented at AIChE 65th National Meeting, Cleveland, Ohio, March 4-7, 1969.

Young, T. 1805. An Essay on the Cohesion of Fluids. *Philosophical Transactions of the Royal Society of London* 95: 65-87

Zhang, K., Dong, X., Jing, L., et al. 2016. Effect of Nanoscale Pore Confinement on Multi-Component Phase Equilibrium. Unconventional Resources Technology Conference, San Antonio, Texas, August 1-3, 2016. URTeC-2456191-MS. DOI: 10.15530-urtec-2016-2456191.

APPENDIX A

FLUID COMPOSITIONS

This appendix contains a listing of the fluid compositions and component characterizations of properties that were used as part of this thesis. For each fluid, the source material is provided. In some instances, some of the fluid parameters, most often volume shift parameter (s), critical compressibility (Zc) and parachor (P) were not provided in the source material. When dealing with known components these values were referenced from another source. For pseudo-components, common correlations were used to calculate the missing component information. Shift parameters were calculated using a correlation from Miqueu et al. (2003). Critical compressibility was calculated using a correlation from Riazi and Daubert (1987). Parachors were calculated using a correlation Alkan and Luan (1993).

Eagle Ford Black Oil

The Eagle Ford oil composition used for analysis throughout this thesis is obtained from Ramirez and Aguilera (2016) and listed below. A reservoir temperature of 225°F is used. All binary interaction coefficients are zero.

Table A.1: Eagle Ford Black Oil Composition and Component Properties

Component	z_i (%)	M_i (lb/lbmol)	$p_{c,i}$ (psia)	$T_{c,i}$ (°F)	ω	s_i	P_i	Z_c
CO_2	0.91	44.01	1070.2	87.6	0.225	-0.0577	78	0.274
N_2	0.16	28.013	492.5	-232.8	0.04	-0.1356	41	0.292
C_1	36.47	16.043	667.4	-116.9	0.008	-0.1540	77	0.288
C_2	9.67	30.07	708.5	89.7	0.098	-0.1002	108	0.284
C_3	6.95	44.097	615.9	205.6	0.152	-0.08501	150.3	0.280
C_4-C_6	12.55	66.869	532	346.2	0.200	-0.0682	206.9	0.277
$C_{7+,1}$	20	107.76	430.6	561.1	0.345	-0.0072	337	0.269
$C_{7+,2}$	10	198.52	263.1	824.8	0.645	0.1191	613.1	0.239
$C_{7+,3}$	3.29	335.11	147	1072.3	1.067	0.2968	1075.1	0.190

Eagle Ford Volatile Oil

The volatile oil composition from Gong et al. (2013) is used with a reservoir temperature of 160°F. All binary interaction coefficients are zero.

Table A.2: Eagle Ford Volatile Oil Composition and Component Properties

Component	z_i (%)	M_i (lb/lbmol)	$p_{c,i}$ (psia)	$T_{c,i}$ (°F)	ω	s_i	P_i	Z_c
CO_2	0.81	44.01	1070.2	87.6	0.225	-0.0577	78	0.274
N_2	0.07	28.01	492.5	-232.8	0.04	-0.1356	41	0.292
C_1	65.54	16.043	667.4	-116.9	0.008	-0.1540	77	0.288
C_2	12.97	30.07	708.5	89.7	0.098	-0.1002	108	0.284
C_3	6.17	44.1	615.9	205.6	0.152	-0.08501	150.3	0.280
n-C_4	2.42	58.1	551.3	305.4	0.193	-0.06413	189.9	0.2743
i-C_4	1.5	58.1	529.2	274.6	0.176	-0.07935	181.5	0.282
n-C_5	1.02	72.2	489.5	385.3	0.251	-0.04183	268.01	0.269
i-C_5	1.08	72.2	491	368.7	0.227	-0.0435	225	0.27
C_6	1.38	86	477.2	453.5	0.275	-0.01478	314.21	0.287
C_{7+}	7.04	177.11	274.3	782.9	0.536	0.12873	666.8	0.307